Core Ion Structures in CO$_2$- and N$_2$O-Based Cluster Anions Studied by Infrared Photodissociation Spectroscopy

by

Michael Charles Thompson

B.S., Baylor University, 2013

A thesis submitted to the

Faculty of the Graduate School of the

University of Colorado in partial fulfillment

of the requirement for the degree of

Doctor of Philosophy

Department of Chemistry and Biochemistry

2018

This thesis entitled:

Core Ion Structures in CO_2- and N_2O-Based Cluster Anions Studied by Infrared
Photodissociation Spectroscopy

has been approved for the Department of Chemistry and Biochemistry

_____

Professor J. Mathias Weber

_____

Professor Veronica M. Bierbaum

Date_____

The final copy of this thesis has been examined by the signatories, and we

find that both the content and the form meet acceptable presentation standards

of scholarly work in the above mentioned discipline.

Thompson, Michael Charles (Ph.D., Chemistry)

Core Ion Structures in CO_2 and N_2O based Cluster Anions Studied by Infrared Photodissociation Spectroscopy

Thesis Directed by Prof. J. Mathias Weber

The interactions of anionic species with other molecules opens up new avenues to study the process of bond formation or charge transfer. Gas phase clusters are a useful tool for studying such systems in the absence of competing effects in condensed phase. Cluster ions can be studied as model analogues to more complex condensed phase systems. The majority of this thesis focuses on gas phase cluster ions of the form $[M(CO_2)_n]$ (M=Bi, Sn, Mn, Fe). These clusters consist of a charged molecular anion surrounded by weakly bound "solvent" CO_2 species. IR photodissociation spectroscopy is used to probe the infrared spectra of the molecular core ions.

$[Bi(CO_2)_n]^-$ and $[Sn(CO_2)_n]^-$ clusters are studied as model systems of the reduction of CO_2 at a corner or edge site of a Bi or Sn electrode surface. The structures of the core ions for these clusters give insight into potential docking motifs of the CO_2 species. In both species, the formation of an η^1-C docked CO_2 species results in a metal carboxylate complex. These structures have characteristic CO_2 stretching frequencies that can be used to identify these species in the condensed phase. These species also exhibit oxalate ligand formation, which is interesting since it requires the formation of a C-C bond.

$[Mn(CO_2)_n]^-$ and $[Fe(CO_2)_n]^-$ clusters are studied to understand how a change in the electron configuration of the metal affects the binding motifs of the CO_2. As in other first row transition metals, these species exhibit a rich collection of interaction motifs, among which the η^2

(C,O), where M-C and M-O bonds are formed, is most prevalent. In addition, oxalate ligands also are present.

We also investigated the structure and charge distributions of neat and heterogeneous N_2O clusters $[(N_2O)_n^-$ and $(N_2O)_nO^-]$. In heterogeneous N_2O clusters, we find that initially the core ion is an NNO_2^- molecular anion. We find that this core ion switches to an O^- core ion at larger cluster sizes. We also find an N_2O^- core ion for neat anionic clusters of N_2O and report for the first time frequencies of the N-N and N-O stretches of the N_2O^- anion.

Dedication

To my family and my teachers for always encouraging me to explore my curiosity.

Acknowledgements

As I conclude this chapter of my life and move onto the next, it is appropriate to look back and acknowledge all those who have been instrumental throughout this journey. Any list of people must begin with my advisor Prof. J. Mathias Weber. I will be eternally grateful for his thoughtful counsel and excellent example. His constant jokes and puns always served to lighten the mood on many occasions and made my graduate experience all the more rich and enjoyable. Mathias has not only been a good mentor, but he has been an example of patience and thoughtfulness that I will strive to emulate.

Throughout my time in the Weber group, I have had the opportunity to overlap with a number of very talented group members. Initially, I overlapped with Dr. Benjamin Knurr and Dr. Shuang Xu. Our conversations about science and philosophy helped grow my own critical thinking and laboratory skills. I am immensely grateful especially to Ben, who showed me how to turn the instrument on and how to make ions. His patience and guidance are one of the reasons I have been as productive as I was during my graduate career. I would like to thank Curtis Beimborn for his friendship and willingness to discuss anything. Recently, I have had the privilege of working with Dr. Leah Dodson. Leah's work ethic and curiosity are inspiring. I thank her for challenging me to think beyond what I am doing in the moment, and constantly pushing me to be better. I have had less time to interact with Wyatt Zagorec-Marks but, I have no doubt that he will be extremely successful.

I have been fortunate enough during my time to work at JILA and participate in the Molecular and Ionic Clusters Supergroup consisting of the groups of Profs. Carl Lineberger, Ronnie Bierbaum, and Barney Ellison. The talks and discussions afterwards have been insightful and enlightening. Specifically, I thank Allan Maple and Dan Nelson for being willing to chat about problems from time to time. I would also like to thank the members of the JILA Machine Shop, the Computing Group, and Electronics Shop. Their knowledge and experience has been indispensable, whether showing me how to use a lathe, helping to restart our calculation computers (for the thousandth time), or diagnosing broken power supplies. Their eagerness to teach and discuss problems have helped mold me into a better scientist.

Lastly, I would like to thank my friends and family. Their support has helped make my graduate career much easier than it could have been. Specifically, I would like to thank the members of the Magic Club for helping me escape the lab every weekend. To my family, I thank you for your quiet support and willingness to listen. While it has been hard being so far away, your support has meant the world to me.

Contents

List of Figures

List of Tables

Chapter 1

Introduction and Motivation

The steadily increasing concentration of CO_2 in the atmosphere has been one of the primary drivers of anthropogenic climate change.[1] One promising avenue toward reducing the amount of CO_2 released is to replace combustion of hydrocarbons as the primary source of electricity. However, new technologies involving solar or wind energy will require modernizing current infrastructure and changing many technology approaches we currently rely on. In the interim, the development of a carbon neutral fuel cycle would allow current technology to be maintained, while decreasing the amount of CO_2 released from industrial sources such as power plants.[2,3]

The chemical conversion of CO_2 into a usable feedstock chemical for the generation of hydrocarbon fuels occurs in the simplest variant via a two-electron reduction process to CO:

$$CO_2 + 2H^+ + 2e^- \rightarrow CO + H_2O \text{ (-0.53 V).}[4]$$

The first step in this conversion in the one electron reduction of CO_2 to CO_2^-,[5] although a hydride transfer to CO_2 has also been proposed as the initial step.[6] In order to discuss this process in the context of catalysis, a thorough understanding of how CO_2 interacts with an excess electron is necessary.

In its neutral ground state, CO_2 is a linear molecule with $D_{\infty h}$ symmetry and CO bond lengths of 117 pm.[7] The highest occupied molecular orbital (HOMO) of CO_2 is the $1\pi_g$ orbital. Examination of the Walsh Diagram of CO_2 shows that an excess electron will be accommodated into the $2\pi_u$ orbital. This orbital is stabilized by the deformation of the OCO bond angle away from 180˚. In its ground state, the CO_2^- has a calculated OCO bond angle of 134˚,[8,9] C_{2v} molecular symmetry, and the singly occupied molecular orbital has a_1 symmetry. Occupation of this orbital

also results in an increase of the CO bond distance from 117 pm in the neutral[7] to 124 pm in the anion.[8] This is not surprising since the HOMO of CO_2^- is antibonding.[10]
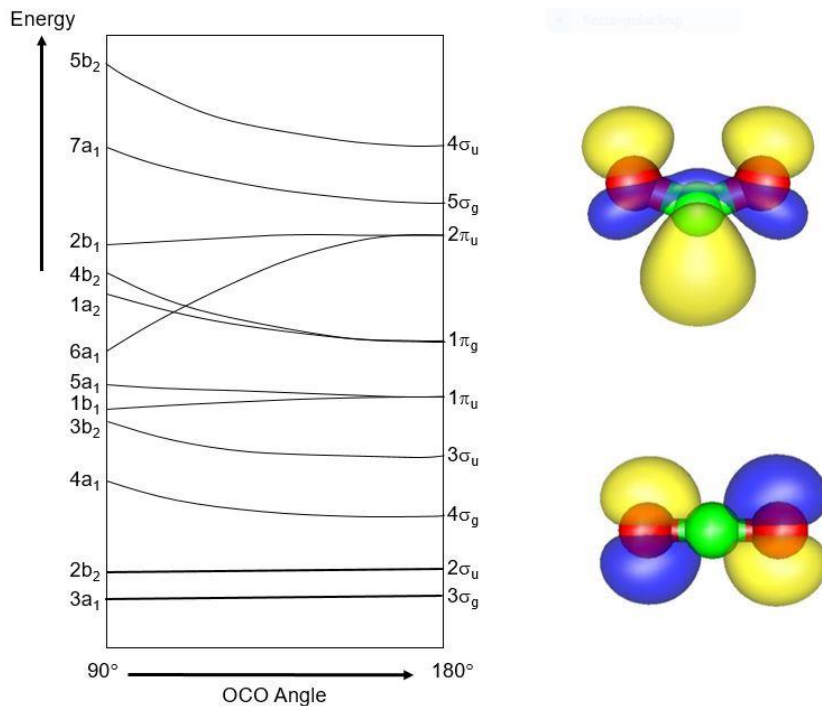
Figure 1.1. Walsh Diagram of CO_2 (Left).[11] Reproduced from Ref. 12 with permission from Taylor and Francis Group. The HOMO of CO_2 (lower) and CO_2^- (upper) based on HF-SCF calculations are shown on the right.

Formation of this radical anion is complicated by the negative adiabatic electron affinity (AEA) of CO_2. Several experimental studies estimate the AEA to be -0.6 eV.[13] Although the CO_2^- anion is unstable against spontaneous electron emission, several observations of CO_2^- have been claimed in mass spectrometry experiments with an estimated lifetime of the ion of up to a millisecond.[14-16] Observations of the anion are possible due to its large vertical detachment energy, 1.4 eV.[17] The CO_2^- anion can be stabilized through interactions with a matrix[18-20] or through solvation of the ion in the condensed phase or in gas phase cluster ions.[21-25] For more details about

how CO_2 interacts with negative charge, the author directs the reader to the following review articles and citations therein.[12,26]

The population of the antibonding HOMO in CO_2^- causes changes in the vibrational frequencies of the anion compared to neutral CO_2. As an example, the antisymmetric CO_2 stretching frequency is red shifted from 2349 cm^{-1} (neutral) to 1665 cm^{-1} (anion).[18,27] Experimental work by Weber and coworkers on $X^- \cdot CO_2$ (X=Cl, Br, I) have shown a correlation between the charge on a CO_2 species and its asymmetric CO_2 stretching frequency.[28] Further work on $[M\text{-}CO_2]^-$ species (M = Au, Ag, and Cu) have corroborated and expanded upon this relationship, establishing that the asymmetric CO_2 stretching frequency can be used to estimate the amount of charge on a CO_2 species.[29-31]

Energetically, it is very costly to add an excess electron to CO_2 (0.6 eV).[14] Industrially the solution to an energetically costly reaction is often to employ a catalyst to both reduce high reaction barriers and as a result increase the reaction rate without the input of large amounts of energy into the reactor. The reductive activation of CO_2 is often employed over atomically rough electrode surfaces in order to increase the accessible surface area. Work by Kanan and coworkers has shown that electrochemically roughened catalyst surfaces are superior to their more atomically flat counterparts.[32,33] This observation has corroborated the hypothesis that the reduction of CO_2 occurs at corner or edge sites of an electrode surface. Ideally, the process of refining a reaction for industrial application uses precise understanding of the fundamental physics and chemistry governing the individual chemical reactions. In the context of CO_2 reduction, one of the first interactions that must be understood is that of CO_2 with these catalytically active corner and edge sites. For more information about catalytic reduction of CO_2 the author recommends the following review articles and references therein.[34-40]

Experimental determination of the binding motifs of CO_2 to corner sites in situ is complicated by speciation, low concentrations, and short lifetimes of reactive intermediates in the condensed phase. In order to limit the number of complicating factors, gas phase cluster ions can be used as a model system to study these interactions in the absence of speciation. Corner sites on a charged electrode surface can be approximated as a single atomic anion, since charge tends to accumulate at these corner sites, and the CO_2 species may interact with a single atom at the site. With this in mind, gas phase cluster ions of a metal atom and CO_2 in the presence of an excess electron can be used to study the binding motifs of CO_2 molecules to strongly charged corner sites. At the very least, these model systems provide insight into the fundamental interactions between CO_2 and undercoordinated metal atoms in the presence of an excess electron.

The structure of the molecular core ions in clusters, and how this structure is perturbed by solvation are the main topics of this thesis. In Chapter 2, the experimental apparatus and experimental and computational methods are discussed. The low concentration of cluster species precludes the use of traditional linear IR absorption spectroscopy. Instead, infrared photodissociation spectroscopy was employed to study the cluster species described in this thesis. Chapters 3 and 4 will compare and contrast the interaction of CO_2 with bismuth and tin anions as a method of understanding the activation of CO_2 at bismuth or tin based electrocatalysts. Chapter 5 examines the interaction of CO_2 with an iron atom and with a manganese atom. While not necessarily applicable to the initial question of CO_2 reduction catalysis, these clusters serve as a way to probe the structure of novel metal-organic compounds containing several carbon dioxide ligands. The final two chapters deviate from the overall theme discussed above. In Chapter 6 the fundamental physics behind the infrared intensity ratios of the asymmetric and symmetric CO_2 stretching modes of $MCOO^-$ (M = H, Ag, Bi) is examined. Chapter 7 focuses on the fundamental

interaction of the solvation environment with the core ions of N_2O cluster anions. N_2O is a fairly interesting analogue to CO_2 because they are isoelectronic. However, electron attachment to N_2O is complicated by a low lying dissociative electron attachment process that results in the formation of $(N_2O)_nO^-$, providing access to fundamentally different types of core ions.

Chapter 2

Experimental and Theoretical Methods

2.1   Overview

Experiments were performed with a custom photodissociation action spectrometer. Ions were generated with one of three methods, entrainment of laser-ablated material into a supersonic expansion[41] (CO_2), entrainment of volatile species into a supersonic expansion (Ar or N_2O) coupled with electron bombardment,[42] or electron bombardment of a neat supersonic expansion (N_2O and CO_2). Each method generates a large number of anionic, cationic and neutral species; the anionic species are injected into a time-of-flight mass spectrometer. Once mass separation is achieved (within the first 10 µs after injection), the ions are mass selected by a pulsed mass gate.[43] The ions are irradiated with tunable light (600 cm^{-1}-4000 cm^{-1}) generated by an infrared optical parametric converter (IR-OPC) system. Absorption of a photon of sufficient energy will result in the loss of a weakly bound component of the cluster. A reflectron is used as a secondary mass analysis step, in order to separate daughter ions from the heavier parents, and the formation of daughter ions is monitored as a function of the laser wavenumber. In the following sections, the experimental apparatus and methods will be discussed in more detail.

2.2   Experimental Methods

2.2.1   Ion Generation

There are several methods for generating gas phase molecular ions, many of which depend on the stability of the ion with respect to the neutral. For fairly large ions, electrospray ionization[44] or matrix assisted laser desorption and ionization (MALDI)[45] are appropriate ionization methods. However, in the case of unstable anionic species (such as CO_2^-), special care must be taken to

stabilize these species against electron auto-detachment.[13] Unstable anions are often formed via electron attachment to neutral cluster species.[14] Lineberger and coworkers developed a supersonic ion source to generate a beam of molecular anions by intersecting a supersonic expansion with the output of an electron gun.[46] Entrainment, described by Campargue in 1970, is a process by which molecules penetrate the first shock boundary of a supersonic expansion and are drawn into the supersonic flow.[47] This phenomenon is useful in preparing reactive gas mixtures without directly seeding the carrier gas prior to expansion. By entraining volatile gases into a supersonic expansion, the exact conditions (i.e. concentrations, backing pressures, etc.) can be easily adjusted to optimize ion production.[42] The supersonic entrainment ion source operates by generating an electron impact plasma in the high-density region of the supersonic expansion. The plasma contains slow secondary electrons that combine with neutral clusters (A•mB) forming "hot" anionic clusters (A•mB^{-*}) (Equation 2.1).

$$A•mB + e^- \text{ (slow)} \rightarrow A•mB^{-*} \tag{2.1}$$

The hot anionic clusters will then evaporate weakly bound constituents in order to dissipate the attachment energy of the electron (Equation 2.2).

$$A•mB^{-*} \rightarrow A•(m\text{-}n)B^- + nB, \tag{2.2}$$
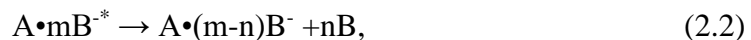
The newly formed clusters exist as a molecular core ion surrounded by one or more weakly bound neutral molecular species that are solvating the ion, and can possess a significant amount of internal energy, in some cases much more than the binding energy of one of the solvating molecules. The process of losing excess energy can be described by an evaporative ensemble,[48] where the cluster species dissipate excess internal energy by evaporating one or more weakly bound molecular species until the ions are stable over the observation time of the experiment. The internal energy

of the clusters can be estimated to be on the order of the binding energy of the last species to be evaporated. The assumption places an upper limit on the internal energy content of a cluster species that possesses at least one weakly bound solvent. The experiments described in this thesis were performed using two ion source configurations, a laser vaporization ion source and an electron impact entrainment source.

2.2.1.1 Laser Vaporization Ion Source

Many of the metal-CO_2 cluster species discussed in the later chapters were generated using a laser vaporization ion source. Initially developed independently by the group of Smalley and by Bondybey and English as a method of generating cold molecular beams of charged metal atoms and clusters,[49,50] laser vaporization ion sources are used to study materials whose low vapor pressure would normally preclude study in a molecular beam experiment. The laser vaporization source used here (Figure 2.1) features a long channel through which a laser is allowed to propagate and impinge on a rotating metal target. The resulting metal vapor is entrained into a pulsed expansion of CO_2 generated from an Even-Lavie valve (stagnation pressure 550 kPa).
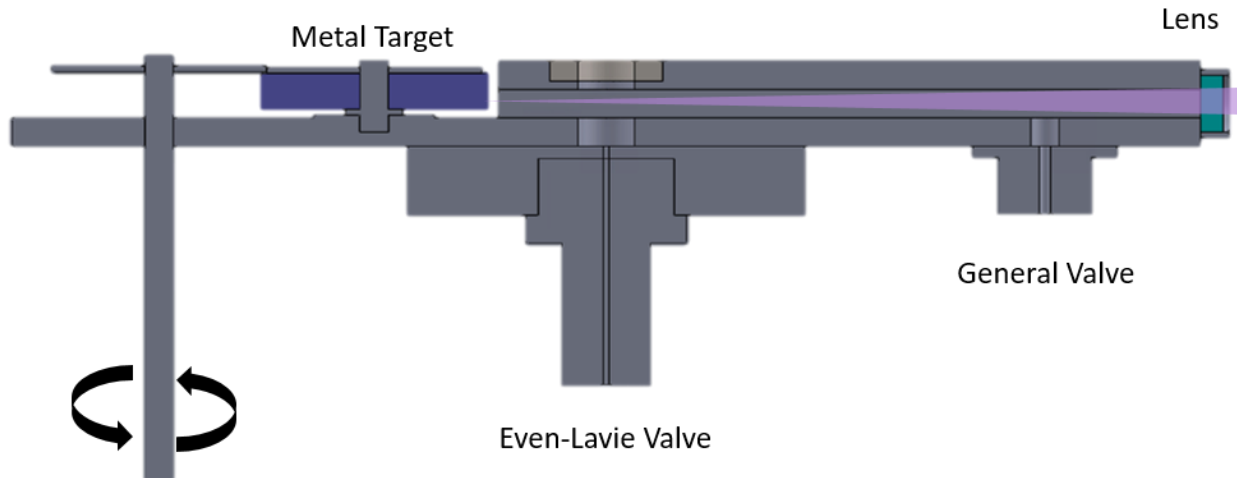
Figure 2.1. Schematic of the ion source. In the laser vaporization method, a laser propagates from right to left and is focused onto the edge of a metal target (see text). In the entrainment of volatile gases experiment, the target gas is introduced with a general valve and entrained into the main expansion (see text), additionally ions can be produced using only the main expansion.

The metal disk targets were 50 mm in diameter with a thickness of 6 mm, and were either purchased (Fe, Mn, Sn) or manufactured in JILA (Bi). Metal from the rim of the target was vaporized with the third harmonic of an Nd:YAG laser (InnoLas Spitlight 300, 355 nm, 7 ns pulse duration, 40 mJ/pulse) approximately 200 µs before the pulsed expansion. A lens, placed at the entrance to the entrainment channel, focuses the laser beam at the target. The disk is rotated to allow the laser to hit a fresh portion of the surface with each experimental cycle. Adiabatic cooling of the entrained metal vapor occurs in the expansion. The laser impact plasma creates a large number of cationic species as well as a sufficient number of slow secondary electrons to allow for the formation of $[M(CO_2)_n]^-$ (n=0-15) in sufficient abundance to perform our experiments. The gas expands into a vacuum chamber typically held at several 10^{-6} mbar, pumped by a 400 Ls^{-1} turbomolecular pump (Leybold Turbovac 361) and a 2000 Ls^{-1} diffusion pump (BOC Edwards Diffstak 250/2000). The current ion source is capable of generating large abundances of clusters

containing a single metal atom and several CO_2 molecules, with small abundances of metal dimer centered structures, depending on the metal in question and source conditions. The experiment is operated at a repetition rate of 20 Hz.

2.2.1.2 Entrainment of Volatile Species

The entrainment of gases into pulsed supersonic expansions was initially developed as an alternative to using seeded buffer gas sources in electron beam ionized supersonic expansion sources.[42] One of the constant struggles with using seeded gas sources in these experiments is the difficulty of changing concentration of the seeded gas in the expansion. Johnson and coworkers describe an ion source for the generation of cold ion-molecule complexes via entrainment of a volatile gas into a supersonic expansion.[42] Entrainment of volatile gases into a supersonic expansion was performed with the same ion source configuration described above using a different ionization technique (see Figure 2.1). For this experiment a Series 9 General Valve (Parker) is used to introduce a secondary gas (B) into the experiment several microseconds before the main expansion. Ions are produced by coupling an electron impact plasma to the supersonic expansion by focusing the output of an electron gun (E_{KE}=800 eV, 10–50 µA) into the high density region of the expansion. The target species is entrained into the main expansion of inert gas (Ar). The resulting electron impact plasma generates slow secondary electrons that then interact with the molecule of interest, forming metastable [B^- • mAr] cluster species. The excess energy of the B anion can be dissipated by evaporating the weakly bound (500 cm^{-1})[51] Ar atoms. A pulse delay generator (Quantum Composers 9614+) controls the gas pulse timing.

2.2.2 Mass Spectrometry and Photodissociation Spectroscopy

Each of the ion sources described above results in the formation of cationic, neutral, and anionic cluster species. In order to separate the anionic species from this mixture, and allow the study of mass selected anions, the ion source is coupled to a Wiley-McLaren time-of-flight mass spectrometer. A schematic of the experimental set up is shown in Figure 2.2. The anionic portion of the molecular beam is accelerated, orthogonal to the expansion axis, into the field-free time-of-flight region by two accelerator plates pulsed from ground to -4000 kV (repeller) and -3000 to -3400 kV (extractor) in a Wiley-McLaren arrangement.[52] Two sets of electrostatic ion deflectors are used to steer the ion beam, and an Einzel lens is employed in order to focus the ion beam. The time-of-flight tube is typically held at a pressure of 10^{-8} mbar and is pumped by a 520 Ls^{-1} turbomolecular pump (Pfeiffer TC600). A delay generator (Quantum Composers 9614+) controls the timing of all triggering pulses.
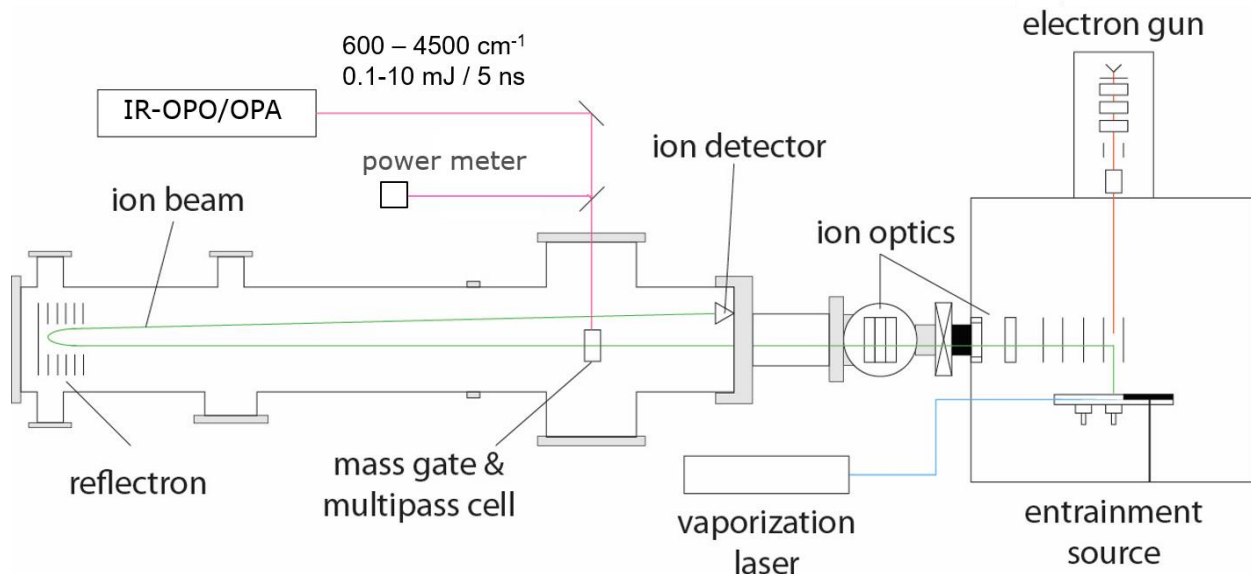
Figure 2.2. Diagram of the experimental apparatus with paths outlined of the vaporization laser (blue), ion path (green), electron beam (red), and laser (purple).

In an idealized mass spectrometer with a point source of ions, each ion receives the same amount of initial kinetic energy in the direction of flight. The relationship between the masses of two ions and their flight times can be written as:

$$\sqrt{\frac{m_1}{m_2}} = \frac{t_1}{t_2} \tag{2.3}$$

The mass spectra can therefore in principle be assigned by knowing the mass of a single peak in the spectrum. The initial assignment of a mass spectrum can be aided by the formation of simple cluster ions (i.e. $(CO_2)_n^-$) which have a known intensity profile as a function of size.[53,54] A typical mass spectrum can be found in Figure 2.3.

In reality, the ions arrive at the acceleration region with a distribution of positions along the time-of-flight coordinate. Ions that are closer to the ion detector will spend less time in the accelerating field and as such will be slower than ions (of the same m/z) that spend more time in the accelerating field. This difference in velocity results in the faster ions eventually overtaking the ions that spent less time in the field. The exact position at which this occurs, as described by Wiley and McLaren,[52] can be adjusted by tuning the biases of the two accelerator electrodes. This position is referred to as the space focus of the mass spectrometer.
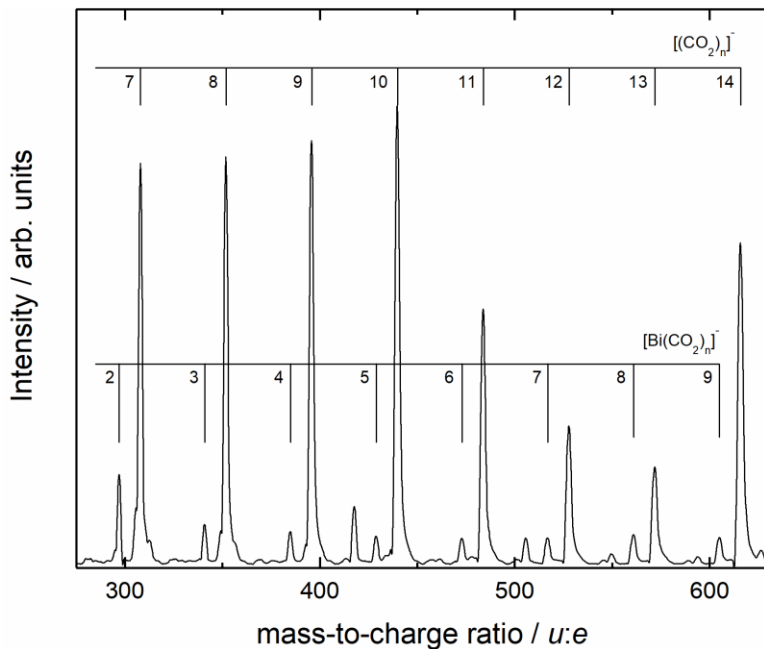
Figure 2.3. Mass spectrum obtained via the laser vaporization ion source with bismuth target and a pulsed CO_2 expansion.

A mass gate, placed at the space focus of the spectrometer, is used to mass select ions.[43] The mass gate consists of a series of parallel shim electrodes that can be biased to ±100 V with neighboring plates alternating in polarity. When the plates are biased, the ions encounter an electric field, which deflects them into the walls of the flight tube. If the plates are grounded, the ions continue on their original path. This device is used to mass select particular mass-to-charge ratios by pulsing the mass gate to ground for a short time (800 ns). Ions that are allowed to pass through the mass gate are irradiated by the output of an IR-OPC system (see section 2.2.3). The ions continue to travel before encountering a two-stage reflectron (Jordon TOF) which reflects the ions. The reflectron serves several purposes in the experiment, primarily the reflectron is used in concert with photodissociation spectroscopy techniques to separate laser generated daughter ions from the parent ions. Secondly, the reflectron is used to account for any differences in velocity of the ions along the time-of-flight axis. Thirdly, the reflectron doubles the flight distance of the ions. This

will result in an increase of the relative flight times of each ion, since there is a larger distance in which to separate the ions. The ions are detected by a microchannel plate detector (MCP) installed at the second space focus of the spectrometer, whose position is defined by the ratio of the electric fields in the two stages of the reflectron.

Photodissociation spectroscopy is a method by which absorption of a photon results in the dissociation of the target molecule. This technique is paired with a tandem mass spectrometer. The first mass spectrometry step serves to mass-select the target ions, which is achieved in the first space focus of the Wiley-McLaren setup in the current experiment. The second mass spectrometry step, occurring after irradiation, is used to monitor dissociation events, since the subsequent loss of mass from the target cluster can be detected as a change of flight time. For the metal-containing cluster systems that will be discussed later in this thesis, the cluster ions in question will typically undergo the following process:

$$[M(CO_2)_n]^- + h\nu \rightarrow [M(CO_2)_{n-1}]^- + CO_2 \tag{2.4}$$
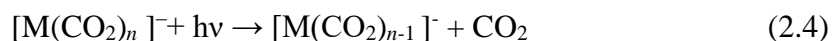
If a cluster absorbs a photon, the absorbed energy is distributed among all energetically accessible modes through intramolecular vibrational redistribution. The now "hot" molecular cluster can dissipate excess energy by evaporating one or more weakly bound solvent species (Equation 2.4). In the case of CO_2 containing cluster anions, an infrared photon, in the wavenumber range 1000-2150 cm^{-1}, typically has enough energy to cause the evaporation of a single CO_2 solvent species. If the photon energy is higher than the binding energy of the most weakly bound solvent species, this process occurs with near unity efficiency during the observation time of the experiment. This is the time between irradiation of the ions and when they reach the reflectron (10-30 µs). When a photon with lower than the binding energy is absorbed, then the cluster must utilize its internal energy prior to photon absorption to evaporate the solvent species. Often this is the case with very

low photon wavenumber (<1300 cm^{-1}), and results in a suppression of the observed intensity of signatures in this energy range.

2.2.3 Light Source

Tunable infrared light in the wavenumber range of 600 cm^{-1} to 4500 cm^{-1} is generated using an IR-OPC system (Laservision, see Figure 2.4).
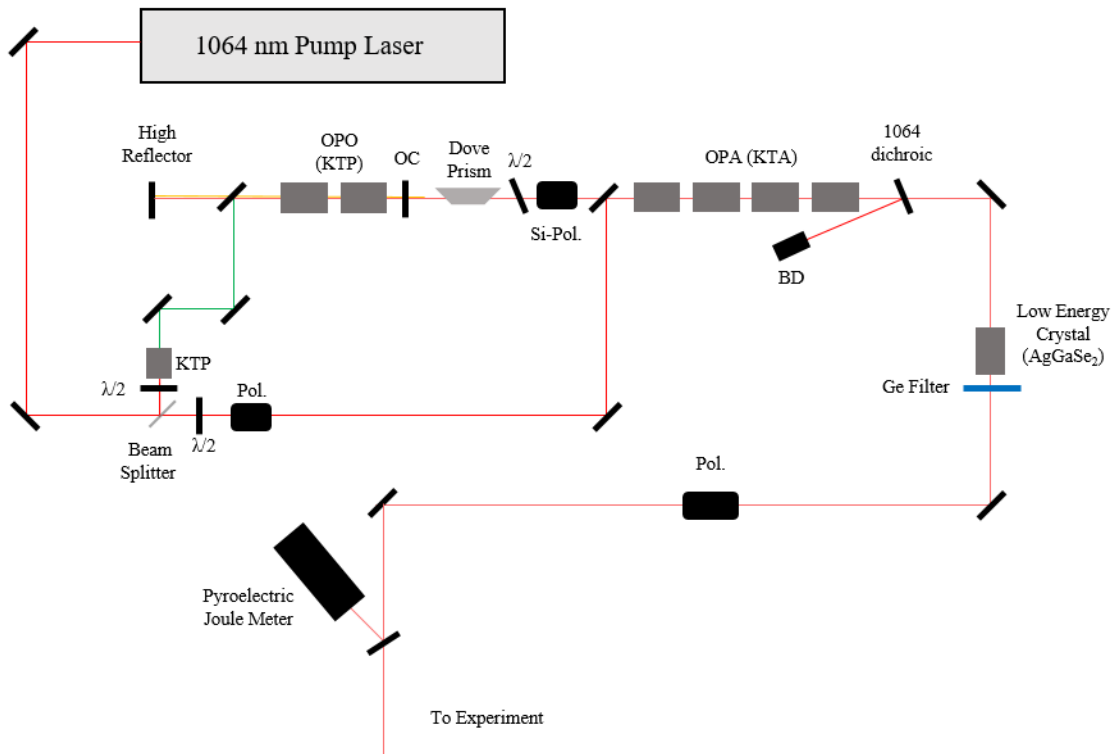
Figure 2.4. Schematic of the Optical Parametric Oscillator/Amplifier system (λ/2, half-wave plate; OC, output coupler; BD, beam dump; Si-Pol., silicon polarizer; Pol., polarizer).

The optical parametric converter system is pumped by a Nd:YAG laser (InnoLas Spitlight 600, 7 ns pulse, 500 mJ/pulse, 1064 nm, ν_{1064}) operating at a 20 Hz repetition rate. The output of the Nd:YAG laser is split into two beams. One of the beams is frequency doubled into 532 nm light and is used to pump an optical parametric oscillator (OPO). The OPO consists of two potassium titanyl phosphate crystals (KTP) inside an optical cavity. The 532 nm pump wave is split into a signal wave (ν_{signal}) and an idler wave (ν_{idler}). The signal and idler wavenumbers are connected by conservation of energy and momentum such that the sum of the energy of these two waves must equal the energy of the 532 nm pump (see equation 2.5). Since the signal and idler waves have perpendicular polarizations, the signal wavelength is separated out of the OPO output by a polarizer. The idler beam profile is rotated 90° by a dove prism to minimize the divergence of the beam in the vertical direction in the next stage. Any residual 532 nm light is removed with a Si-polarizer, which acts as a filter for light below 1127 nm. The second 1064 nm beam is routed into a delay stage and directed into an optical parametric amplifier (OPA), which consists of four potassium titanyl arsenate crystals (KTA). The delayed 1064 nm beam is difference-frequency mixed with the idler output of the OPO (see equation 2.6). This generates mid-infrared light (ν_{midIR}) in the range of 2100 cm^{-1} to 4500 cm^{-1} (pulse energy 5 mJ to 20 mJ). Any residual 1064 nm light is reflected by a 1064 mirror and dumped.

The mid-IR and idler beams co-propagate out of the OPO/OPA and onto a second table. Depending on the frequency of light needed, the idler beam is removed via a polarizer or the mid-IR and idler beams are allowed to undergo difference frequency mixing in a single silver gallium selenide (AgGaSe$_2$) crystal. Mixing in the crystal generates a far-IR ($\nu_{far\ IR}$) beam with an energy range of 600 cm^{-1} to 2150 cm^{-1} (see equation 2.7; pulse energy 10 µJ to 100 µJ). Any remaining mid-IR and idler radiation are removed from the far-IR beam by a germanium filter, which only

allows far-IR light to pass (transmission 5-14 µm). A summary of the various frequency relationships can be found below in equations 2.5 to 2.7.

$$2 \times \nu_{1064} = \nu_{signal} + \nu_{idler} \tag{2.5}$$

$$\nu_{1064} - \nu_{idler} = \nu_{midIR} \tag{2.6}$$

$$\nu_{idler} - \nu_{mid\ IR} = \nu_{far\ IR} \tag{2.7}$$

The OPO is calibrated by measuring the signal wavelength (719 – 820 nm) after the OPO stage. A combination of two spectrometers is used to measure the signal wavelength, an Ocean Optics fiber-optic spectrometer (820 to 750 nm) and an Avantes fiber optic spectrometer (750 to 719 nm). We estimate the bandwidth of the optical parametric converter system to be around 2 cm^{-1}. Given that H_2O and CO_2 exhibit very strong lines in the tuning range of the OPO/OPA, the entire beam line is purged with dry nitrogen, in order to eliminate the loss of power due to absorption by atmospheric trace gases.

2.2.4 Signal Acquisition and Processing

In order to monitor the mass spectrum, the signal from the microchannel plate detector is visualized using two digital oscilloscopes (Tektronix TDS 2022). The IR photodissociation spectra are measured by monitoring the formation of lighter daughter ions as a function of laser wavenumber. One of the oscilloscopes is set to display the entire width of the daughter peak (~100 ns). The intensity of the ion signal is averaged over 64 shots per data point. A second oscilloscope monitors a section of the mass spectrum with no ion signal. This oscilloscope captures any changes in the baseline of the mass spectrum (background) as the fragment intensity is monitored. The IR-OPO/OPA is scanned along the tuning range by a LabVIEW program, which also collects the output data of the oscilloscopes. Laser power is monitored by placing a KBr window into the

beamline and measuring the back reflection with a pyroelectric joule meter. Since the transmission efficiency of KBr is constant over the tuning range of the OPO/OPA the pulse energy of the IR beam can be monitored using this back reflection. This also allows for simultaneous measurement of both laser power and photodissociation signal. The raw fragment formation data are further processed by subtracting the background from the laser induced fragment signal. The resulting infrared spectrum is then corrected for photon fluence by dividing the signal intensity by the photon number as a function of photon wavenumber. Several spectra collected over multiple days are averaged in order to increase the signal-to-noise ratio of the average spectrum. In addition, collecting data over several days allows us to confirm the reproducibility of the infrared spectra.

2.3 Computational Methods

In this section, common computational methods will be briefly discussed. In some cases, different systems required other computational methods. These calculations will be discussed in the appropriate chapter as necessary. Generally, in order to aid in the interpretation of the photodissociation spectra, quantum chemical calculations are employed in order to determine the structure of the clusters in question.

Calculations were performed on the TURBOMOLE suite of programs[55] (ver. 5.9.1 and ver. 6.2) using density functional theory with a dispersion corrected B3LYP functional,[56,57] and def2-TZVPP basis sets for all atoms.[58] Harmonic frequency calculations were performed using the AOFORCE program.[59] For CO_2 based systems, harmonic frequencies were corrected for anharmonicity using a correction factor of 0.975, which was found by comparing the harmonic frequency of free CO_2 with experimental values. Some vibrations were corrected using other values, these motions will be described in the appropriate section. Approximations of the charges on each individual atom were calculated using Natural Population Analysis.[60]

Initially, cluster structures are created based on chemical intuition and then optimized using the above methods. The calculated vibrational spectra are then convoluted with a 12 cm^{-1} full width at half-maximum Gaussian to generate a calculated vibrational spectrum that is then compared to the experimental spectrum of a given cluster. Assignments are made based on the agreement between these calculated spectra and the experimental spectrum.

Chapter 3

Interactions of CO_2 with Bismuth: Formation of Metalloformate and Metallooxalate Complexes

This chapter has been adapted with permission from:

Thompson, M. C., Ramsay, J., and Weber, J. M. "Solvent-Driven Reductive Activation of CO_2 by Bismuth: Switching from Metalloformate Complexes to Oxalate Products." Angewandte Chemie International Edition, 2016. 55: p. 15171-15174. DOI: 10.1002/anie.201607445. Copyright John Wiley and Sons. License Number: 4310361273540

3.1 Introduction

The chemical conversion of CO_2 into hydrocarbon fuels in a carbon neutral fuel cycle is a promising avenue toward reducing worldwide dependence on fossil-based fuels. Many synthetic routes to hydrocarbon fuels from CO_2 begin with the reduction of CO_2 to CO.[39] Researchers such as Hori and coworkers during the late 1980s and 1990s studied the product distributions and energetics of CO_2 electroreduction over many different electrode materials ranging from transition metals to p-block metals.[61-63] These studies showed that the product of electroreduction of CO_2 at p-block metal electrodes was primarily formic acid, while reduction over noble metal electrodes (Au, Ag) produced carbon monoxide as a principal product.[4]

Several years ago, Rosenthal and coworkers were successful in developing a device for the formation of CO from CO_2 by electrodepositing bismuth onto glassy carbon. The resulting surface

was incorporated into an electrochemical device with ionic liquid saturated with CO_2.[64] The result of this experiment was a working device capable of forming CO at Faradaic efficiencies comparable to devices made of electrochemically roughened or sputtered gold surfaces. Further experiments using deposited bismuth nanoparticles as electrode material resulted in Faradaic efficiencies comparable to those of bismuth foil and electrodeposited bismuth surfaces.[65]

An open question regarding these catalytic devices is the exact mechanism of CO formation. While several theories exist for homogeneous CO_2 reduction catalysts,[66,67] the sheer number of morphologies seen on electrode surfaces makes hypothesizing an exact mechanism difficult. A consensus is that the first step in the reduction of CO_2 to CO is the single electron reduction of the CO_2 to $CO_2^{\bullet-}$.[5,39,68] At the same time, this is believed to be the rate-limiting step in the reduction of carbon dioxide. As such, an important first process to examine would be the docking of a CO_2 molecule onto the electrode surface and the transfer of a single electron to the molecule. Gas phase clusters have been used as effective model systems to study the behavior of CO_2 interacting with under-coordinated atoms on a metal surface.[29-31] In this chapter, the interaction of CO_2 with a bismuth atom in the presence of an excess electron is discussed.

3.2 Results and Discussion

In order to understand how a CO_2 molecule interacts with a bismuth atom in the presence of an excess electron, we measured the IR photodissociation spectra of $[Bi(CO)_2)_n]^-$ (Figure 3.1). The experimental spectra are displayed as a series of individual traces, where the numbers indicate the size of the cluster, n. Each individual spectrum is scaled to the highest intensity peak. In anionic metal-CO_2 clusters, the CO_2 molecules can take on one of two roles; the CO_2 molecule is directly bound to the metal atom as a ligand, or the CO_2 molecule solvates the molecular core ion. Signatures that appear in the spectral region shown in Figure 3.1 are CO stretching vibrations of

CO_2 species that are directly bound to the metal as ligands. These ligands exhibit binding energies in excess of 4000 cm^{-1},[69,70] such bonds cannot be broken with a single photon in the energy ranges used in this experiment. The CO_2 species that solvate the core ion are less tightly bound than the ligands (around 1500 cm^{-1}). The presence of one or more solvent CO_2 molecules is necessary for clusters to be observable in this experiment. CO vibrational frequencies of CO_2 ligands are red shifted compared to the analogous motions in free CO_2. This is due to charge sharing that occurs between the metal center and the ligand(s). For an in-depth discussion of how CO_2 interacts with negative charge, see Chapter 1.
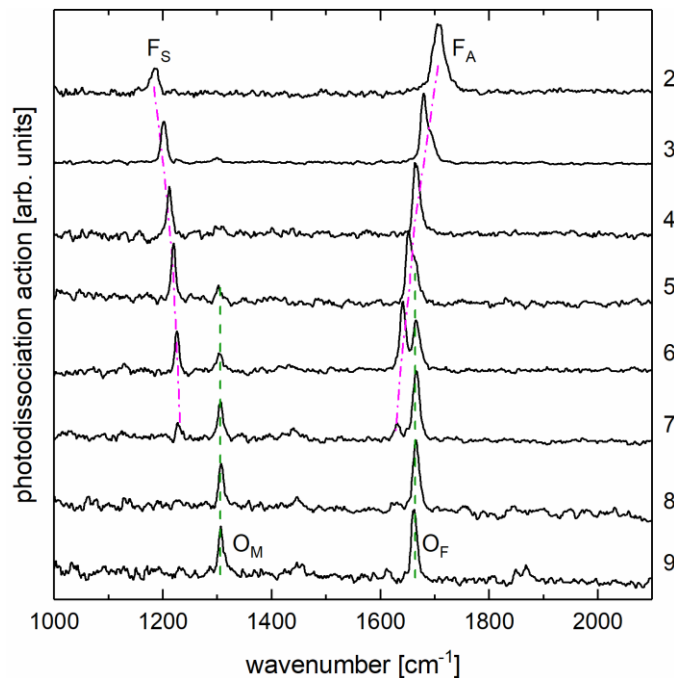
Figure 3.1. IR photodissociation action spectra of $[Bi(CO_2)_n]^-$ ($n=2–9$). Labels denote the core ion geometry (F=metalloformate, O=oxalate) and the subscript letters denote the type of oscillation (S=symmetric, A=asymmetric, M=metal bound, F=free). The dashed lines are meant to draw the eye to experimental signatures of the metalloformate complex (magenta) and metallooxalate complex (green).

The spectra of the smaller cluster ions ($n=2–4$) share a set of spectral features, labeled F in Figure 3.1. These spectral features appear to blue-shift (F_S) and red-shift (F_A) as cluster size

increases. In the intermediate cluster size regime ($n=5$–7) another set of spectral features appear (O_M, O_F) and grow in intensity relative to F_S and F_A. At larger cluster sizes ($n=8$–9), the second set of spectral features become the only observed signatures. Unlike F_S and F_A, the positions of O_F and O_M do not change with increasing cluster size. The appearance of the second set of peaks (O_F and O_M) and the disappearance of the first set (F_A and F_S) suggests a change in core ion geometry as cluster size increases. Such changes have been observed previously, and often can be associated with the formation of a first solvation shell, or the stabilization of a core ion structure due to increased solvation.[23,25,71]

The structure of cluster species was determined by comparing calculated vibrational frequencies of a variety of cluster geometries with the experimental spectra. The harmonic calculated frequencies are corrected by a factor of 0.9398 for the asymmetric CO stretching motion and 0.9655 for the symmetric CO stretching motion of the metalloformate core ion as found by comparing known experimental values[18,29] with calculated values.[72] All other motions were corrected as described in Chapter 2. A summary of the stable core ion geometries is shown in Figure 3.2.

| Metalloformate | (C,O)-Bidentate | Butterfly | Oxalate |
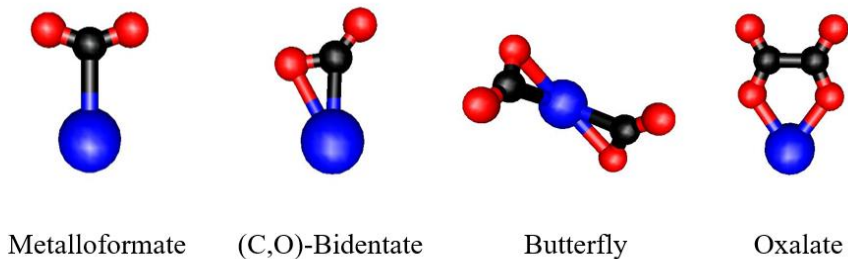
Figure 3.2. Calculated core ion geometries (Bi, blue; C, black; O, red).

The metalloformate ion is a simple species where the CO_2 ligand forms a single bond from its carbon atom to the metal center. The geometry is the result of an attraction of the partially positive carbon atom to the negatively charged metal center, accompanied by a repulsion of the partially negative oxygen atoms. The result is a formate-like complex where the hydrogen atom has been replaced with a bismuth atom. The (C,O)-bidentate ion is a species where the CO_2 molecule forms two bonds to the bismuth center through the carbon atom and one of the oxygen atoms. This geometry is only computed in the singlet spin configuration, while the metalloformate geometry is found only in the triplet spin configuration.

The larger core ions feature two CO_2 species acting as ligands. The butterfly structure consists of two CO_2 ligands each bound in a (C,O)-bidentate motif. In the oxalato ligand, two CO_2 molecules are connected to one another through the formation of a C-C bond, and the ligand binds to the metal atom through two oxygen atoms belonging to different CO_2 subunits. This geometry is stable in both singlet and triplet configurations, while the butterfly structure is stable only in the singlet spin state. A summary of which calculated core ions are observed in either triplet or singlet spin states is shown in Table 3.1.

Table 3.1. Spin states of calculated core ion geometries

Core Ion Geometry	Stable in singlet spin state?	Stable in triplet spin state?
Metalloformate	No	Yes
(C,O)-Bidentate	Yes	No
Butterfly	Yes	No
Oxalate	Yes	Yes

Each set of spectral features (F and O) can be assigned by comparing calculated vibrational spectra to the experimental spectra (Figure 3.3). Beginning with $[Bi(CO_2)_2]^-$, two spectral features are present at 1707 cm^{-1} (F_A) and 1186 cm^{-1} (F_S). These experimental signatures are compatible with either (C,O) bidentate or metalloformate based clusters. We note that clusters with (C,O) bidentate core ions lie approximately 400 meV higher in energy than the metalloformate based clusters. This suggests that the spectral series F_A and F_S are due to clusters with metalloformate core ions, and that clusters with a (C,O) bidentate core ion geometry are not present in our experiment. Therefore, we assign F_S and F_A to the symmetric and asymmetric CO stretching motions of the carboxylate ligand. It is interesting to observe the contrast in relative intensities in the calculated vibrational spectrum for metalloformate versus the experimental spectrum.
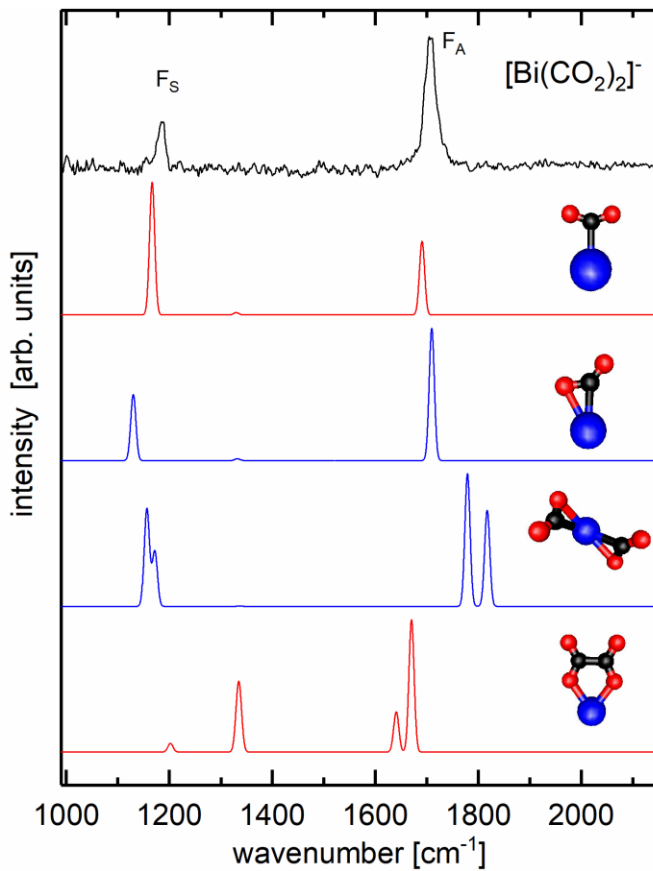
Figure 3.3. $[Bi(CO_2)_2]^-$ experimental spectrum and calculated spectra. The colors of the traces indicate the spin of the structure (red, triplet; blue, singlet), and the core ion whose vibrational signatures are shown are pictured above each trace. The top two structures have solvent species behind the ligand.

The formation of a metalloformate complex in this study compares well with previous work on anionic clusters of CO_2 with Ag and Au atoms.[29,30,72] In those cases, the metal and carbon atoms form a σ bond between the s-orbital on the metal atom and the $π^*$ orbital of the CO_2 ligand. Similarly, the Bi-C bond is also a σ bond. However, the bond is formed between the p-orbital of the Bi atom and the $π^*$-orbital of the CO_2 ligand (Figure 3.4). This suggests that the charge donation from the metal atom to the CO_2 ligand occurs from the orbital on the metal that

the excess electron occupies (the 5s- or 6s-orbital in the case of Ag or Au, and the $6p_z$-orbital of Bi).
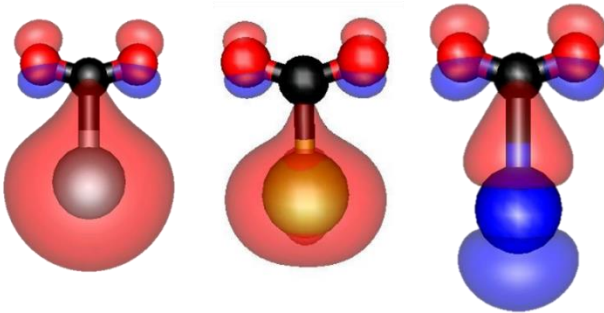
Figure 3.4. Calculated HOMOs (70% contour) of several $MCOO^-$ species [M=Ag (silver), Au (yellow), and Bi (blue)].

The spectral shifts of the F series contain important information regarding the overall structure of the solvation shell around the metalloformate core ion. As has been seen previously, the red shift of the F_A signature is due to increased solvation around the ligand side of the core ion.[29-31] Solvation around the carboxylate ligand polarizes excess electron density onto the ligand. As discussed in Chapter 1, excess electron density is accommodated in an antibonding orbital of CO_2. This weakens the CO bonds and should result in a red shift of the CO oscillators. This expectation is consistent with the behavior of the F_A signature, which strongly red shifts as cluster size increases. The blue shift of the F_S signature is directly contrary to this expectation, as F_S should also red shift, in the absence of other effects. There is, however, an additional structural change in CO_2 upon accommodation of an excess electron, as the OCO bond angle decreases from 180° to 134°.[73] The same occurs in the bismuthoformate core ion, as the OCO bond angle decreases as a function of cluster size from a calculated 140° in the bare complex to 133° in the $[Bi(CO_2)_6]^-$. The

decrease of the OCO bond angle results in a decrease of the kinetic coupling of the CO oscillators. As the coupling decreases, the energy difference between the symmetric and asymmetric CO stretching modes decrease. Experimentally, this would present itself as a red shift of the asymmetric stretching frequency and a blue shift of the symmetric stretching frequency. This effect should result in a shift of the same magnitude and opposite sign for the symmetric and asymmetric CO_2 stretching frequencies, in the absence of the red shift associated with a weakening of the CO bonds. This means that the average position of these two frequencies and its shift should show the weakening of the CO bonds, while the decrease of the kinetic coupling between the two CO oscillators is encoded in the diminishing splitting between the two modes. Figure 3.5 shows that the average position of the two signatures redshifts as cluster size increases. This demonstrates that the weakening of the CO bonds is contributing to the observed spectral shifts. Also shown is the splitting between F_S and F_A as a function of cluster size; the decrease of this splitting indicates that the OCO bond angle is decreasing with increasing cluster size.
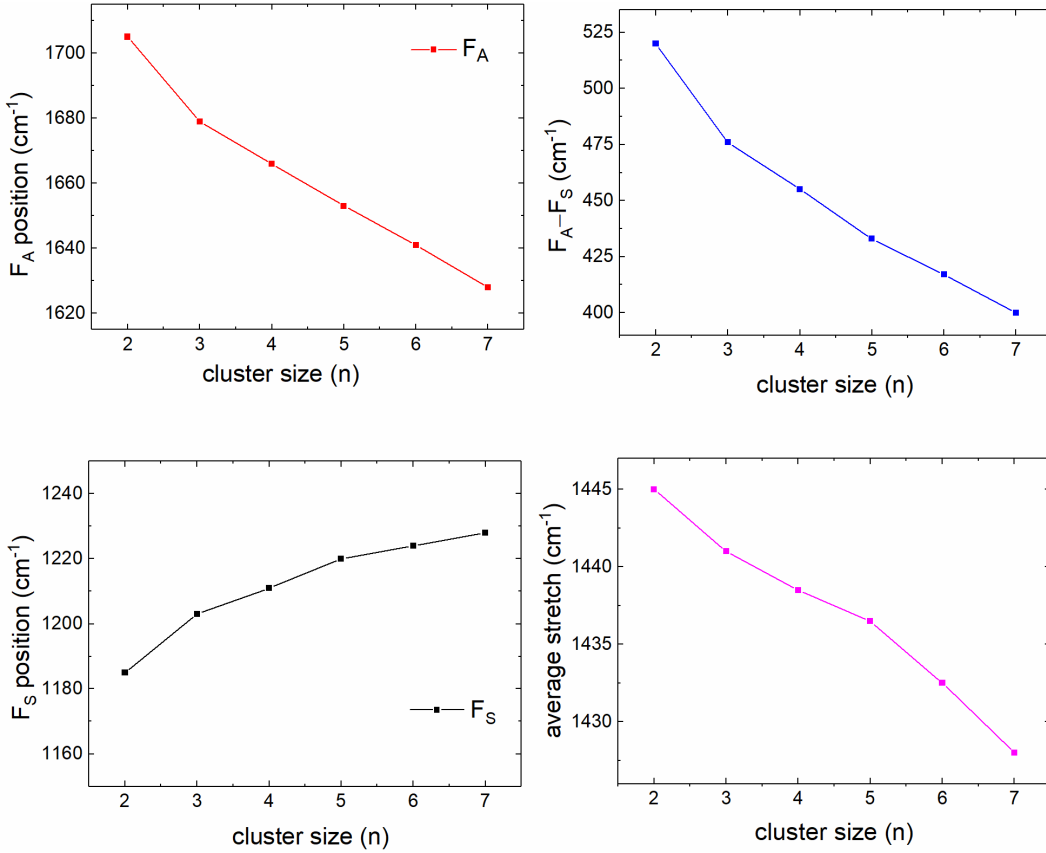
Figure 3.5. Positions of the signatures in the F series as a function of cluster size for the asymmetric (red, top left) and symmetric (black, bottom left) as well as the difference (blue, top right) and the average between F_S and F_A (magenta, bottom right).

A second set of spectral features appears beginning with $[Bi(CO_2)_6]^-$, and becomes the dominant set of signatures seen in the spectra of the larger clusters. The two signatures appear at 1665 (O_F) and 1304 cm^{-1} (O_M). A comparison of calculated vibrational spectra and the experimental spectrum (Figure 3.6) shows that the new spectral features are clearly due to the formation of a bismuth oxalate complex.
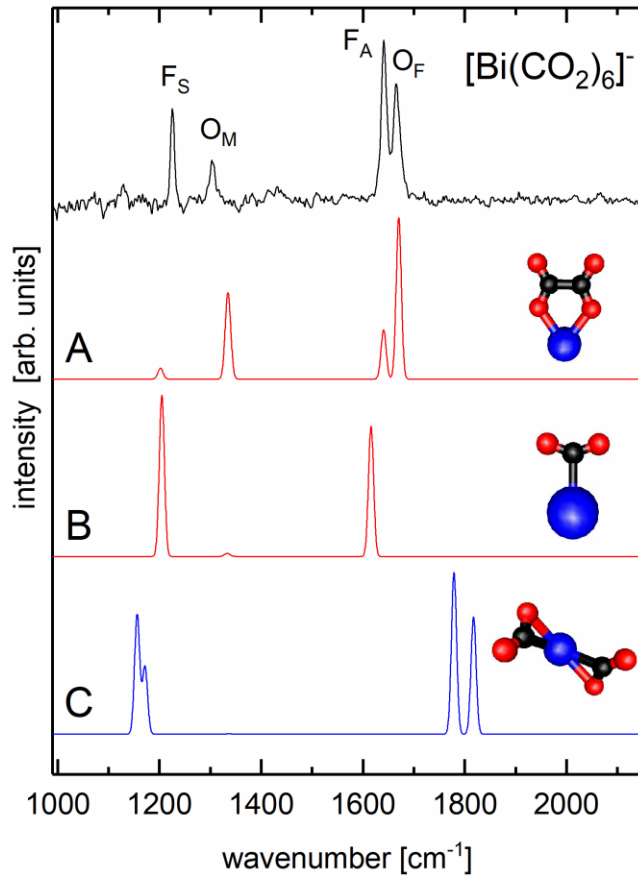
Figure 3.6. $[Bi(CO_2)_6]^-$ experimental spectrum and calculated spectra (black, top). The colors of the lower traces indicate the spin of the structure (red, triplet; blue, singlet). Calculated vibrational frequencies of a metallooxalate based $[Bi(CO_2)_6]^-$ cluster (A) , a metalloformate based $[Bi(CO_2)_6]^-$ cluster (B), and a butterfly based $[Bi(CO_2)_2]^-$ cluster (C).

Based on these calculations the new spectral feature at 1665 cm^{-1} is assigned to the symmetric combination of free CO stretches in the oxalate ligand. We note that the asymmetric combination of free CO stretches is predicted to have infrared intensity, but its intensity is calculated to be 30% of that of the more intense symmetric free CO stretch. At cluster size $n = 6$, this feature is buried underneath F_A. The spectral signature at 1304 cm^{-1} is assigned to the symmetric combination of metal bound CO stretches in the oxalate ligand. Similar to the free CO stretches, the asymmetric

combination of metal bound CO stretches is also predicted to be much lower in intensity compared to the symmetric combination.

The absence of any clear oxalate based vibrational signatures in the photodissociation spectra of smaller clusters is something that warrants further discussion. Although clusters with singlet oxalate core ions are calculated to be the lowest energy isomer for all cluster sizes, oxalate features are only observed for intermediate and larger cluster sizes (n=6–9). The presence of triplet based metalloformate containing cluster species in small cluster sizes suggests that a comparison between the relative energies of triplet oxalate and metalloformate based clusters is appropriate. A comparison of the relative energies of clusters containing these two core ion geometries as a function of cluster size (Figure 3.7) shows that the triplet oxalate based clusters are stabilized as cluster size increases. This trend continues until the two types of clusters are isoenergetic at $n = 5$ and then the oxalate based cluster is lower in energy at $n = 6$.
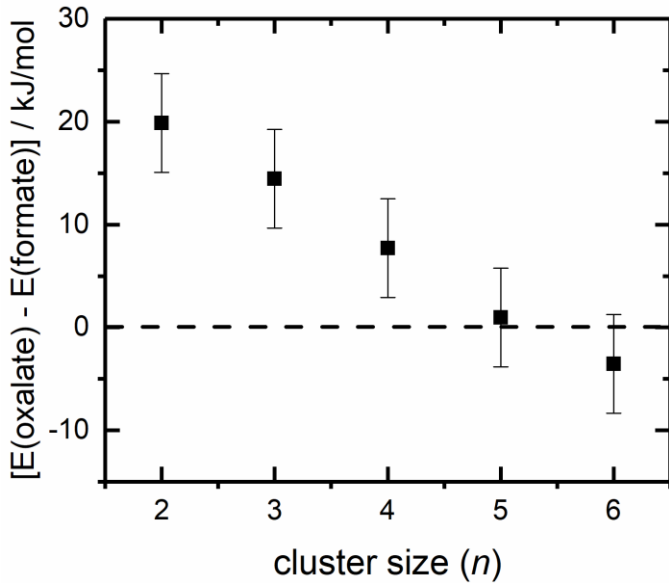
Figure 3.7. Comparison of the relative energies of the triplet formate and triplet oxalate core ion clusters as a function of cluster size.

The calculated cluster size where the two types of clusters are isoenergetic is identical to the experimental observation of oxalate based signatures at cluster size $n=5$. Since the appearance of oxalate based signatures seems to be tied to the relative stability of the triplet core ion geometry, clusters are most likely formed in the triplet electronic configuration. This suggests that the ions are formed via association reactions of CO_2 with Bi^- in its $^3P_2$ ground state during supersonic expansion. We note that there are of course many different solvation positons around a given core ion. We have calculated several different solvation positions and have generally found that the difference in energy between different solvation positions is small (± 50 meV) for these cluster species, and this value is used as the error bars in Figure 3.7.

The increasing stability of triplet oxalate based clusters can be explained through an analysis of the amount of charge on this ligand compared to metalloformate-based clusters. Natural population analysis assigns a maximum charge of -0.9 e on the carboxylate ligand of large

metalloformate based clusters (n=6). The oxalate ligand contains a calculated charge of approximately -1.5 e. The differential solvation energy gain demonstrated in Figure 3.7 is due to solvating a larger amount of charge, which is more favorable than solvating a smaller amount of charge. This proposed mechanism is slightly different from other observed core ion changes in cluster ions. In the case of $(N_2O)_nO^-$, changes in the core ion structure are driven by core ion size rather than purely by charge as it is in the case of $[Bi(CO_2)_n]^-$.[23,25]

3.3 Conclusions

The interaction of CO_2 with bismuth in the presence of an excess electron was studied using photodissociation spectroscopy of mass selected $[Bi(CO_2)_n]^-$ (n=2–9). Small anionic clusters (n=2–4) have a metalloformate core ion structure. Intermediate clusters (n=5–6) have both metalloformate and metallooxalate core ion structures. Larger cluster sizes only exhibit a metallooxalate core ion structure. Solvation around the ligand of a metalloformate core ion polarizes charge onto the ligand. The increased charge can be detected as a red shift of the asymmetric CO stretching frequency. Increased charge also results in a decrease of the OCO bond angle. The decrease of this angle decreases the kinetic coupling of the individual CO oscillators. This is observed as a blue shift of the symmetric CO stretching frequency. The change from metalloformate to metallooxalate core ion geometries is due to the larger amount of charge on the oxalate ligand, which has a larger solvation energy compared to the metalloformate core ion.

Chapter 4

Interaction of CO_2 with a Sn Atom in the Presence of an Excess Electron: Formation of a

Weak Sn–C bond.

This chapter has been adapted with permission from:

Thompson, M. C., Ramsay, J., Weber, J. M., "Infrared Photodissociation Spectra of $[Sn(CO_2)_n]^-$ Cluster Ions." Journal of Physical Chemistry A, 2018. ASAP DOI: 10.1021/acs.jpca.8b00362. Copyright 2018 American Chemical Society.

4.1 Introduction

As stated previously, one of the limitations in developing economically viable catalysts for CO_2 electroreduction to liquid fuels is the development of cheaper catalytic materials. Some of the more promising materials explored in recent years have been inexpensive post transition metals, such as Sn and Bi.[65,74] Hori and coworkers have studied the catalytic activity of Sn toward CO_2 previously.[4,61] Additional work has shown that electroreduction of CO_2 at Sn electrode surfaces resulted in formic acid formation.[61,63,75] Sn nanoparticle based electrodes have shown formate formation to be the dominant reaction pathway under turnover conditions.[76]

An electrochemically roughened Sn based electrode surface has shown very high Faradaic efficiencies for carbon monoxide formation.[77] The efficiency of this device rivals that of traditional catalytic materials for CO_2 reduction (Ag and Au). Kanan and coworkers first reported that electrochemically roughened surfaces exhibited increased catalytic activity, compared to more atomically flat surfaces.[32,33,78] In principle, such roughened surfaces should have a larger concentration of corner and edge sites, which are thought to be the catalytically active sites on the surface. Experimental measurements of the binding motifs of CO_2 at catalytically active sites on an electrode surface in situ is often hindered by the chemical environment in the condensed phase.

This problem is further enhanced under turnover conditions where reaction intermediates may not survive long enough to be investigated. In this chapter, the IR photodissociation action spectra of $[Sn(CO_2)_n]^-$ are reported. The structure of the core ions will be discussed along with the effects the solvent molecules have on the core ion's structure and charge distribution.

4.2 Results and Discussion

The experimental spectra of $[Sn(CO_2)_n]^-$ ($n = 2–6$) are shown in Figure 4.1. As mentioned previously, vibrational signatures in the region from 1000 cm^{-1} to 2150 cm^{-1} are due to reduced CO_2 stretching motions of the molecular core ions. Signatures in the region from 2175 cm^{-1} to 2450 cm^{-1} can be assigned to asymmetric CO_2 stretching modes of solvent CO_2 species. Vibrational bands in this region blue shift by approximately 3 cm^{-1} as cluster size increases, similar to the behavior observed in other M-CO_2^- cluster species (M = Au, Ag, Cu, Co, Ni, Bi, Mn, Fe, Ti).[29-31,69,70,79-82] The nature of the blue shift is due to a decreasing influence of the negative core ion on the solvent species as cluster size increases.
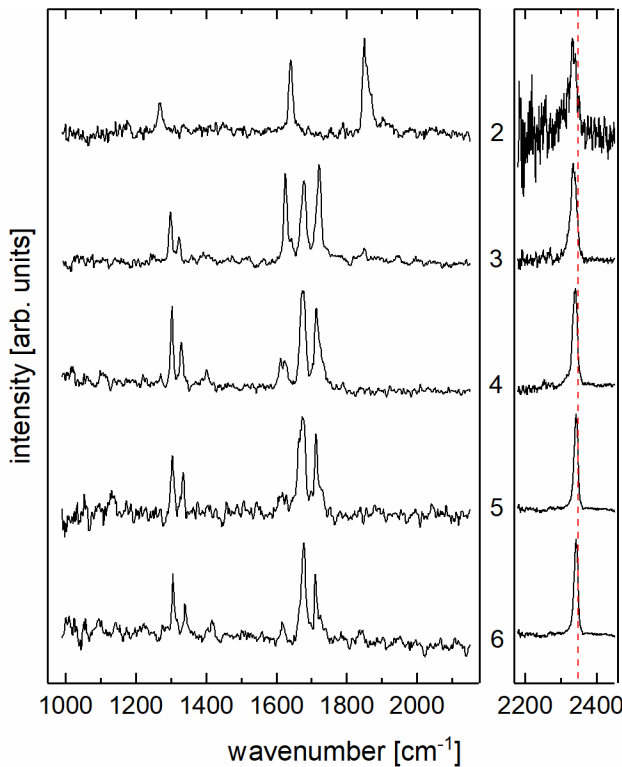
Figure 4.1. Infrared photodissociation spectra of $[Sn(CO_2)_n]^-$ ($n = 2–6$). Cluster size is denoted by the numbers between the two panels. The red dashed line gives the position of the asymmetric stretching mode of free CO_2. Each trace is individually normalized to the highest intensity feature.

The vibrational modes of the core ion cluster can be described as asymmetric and symmetric stretching motions of negatively charged CO_2 ligands bound to the metal atom. The magnitude of the red shift of the asymmetric CO_2 stretching frequency of metal bound CO_2 species compared to neutral CO_2 species can be related to the amount of charge shared from the metal ion to the CO_2.[29-31] As described in Chapter 3, the presence of excess charge on the CO_2 species results in a decrease in the OCO bond angle away from 180°.[11,12,26]

An initial inspection of the experimental spectra will immediately reveal the large change in spectroscopic signatures that occurs between cluster size $n = 2$ and $n = 3$. The appearance of many new experimental signatures in the region from $1650 – 1750$ cm^{-1} with increasing cluster

size is often due to the experiment becoming sensitive to larger core ion geometries. As described in Chapter 2, IR photodissociation spectroscopy requires the presence of a weakly bound solvent species in these metal-CO_2 cluster ions in order for an absorption event to be detected on the time scale of the experiment. There is not a large difference between the experimental spectrum of cluster size $n = 3$ and the spectra for larger cluster sizes besides some changes in the relative intensities of the signatures. This suggests that the largest core ion geometry present in the molecular beam has a chemical formula of $[Sn(CO_2)_3]^-$.

As described in Chapter 3, the intensity of infrared signatures below 1500 cm^{-1} are artificially suppressed due to the energy of the photon being lower than the binding energy of a weakly bound CO_2 species. When the energy of an absorbed photon is lower than the binding energy of a solvent species, only the cluster ions with internal energy above a critical level will evaporate a solvent species on the timescale of the experiment. The internal energy of a cluster can be estimated using an evaporative ensemble (see Chapter 2). Briefly, the internal energy content of the cluster is estimated to be on the order of the binding energy of the last solvent species to evaporate from it during cluster formation.[48] Calculations indicate that the binding energy of a solvent molecule to the molecular core ion is dependent on solvation position, particularly for small clusters. On average, the binding energy of a CO_2 solvent species is around 1500 cm^{-1}. For small cluster sizes, the intensity of features below 1500 cm^{-1} will therefore be suppressed in the experimental spectrum.

Just as in the case of Bi-CO_2 cluster anions, Sn-CO_2 clusters can exist in two different spin states. The $5s^2 4d^{10} 5p^3$ valence electron configuration of a Sn anion implies that Sn-CO_2 complexes can exist in either a doublet or quartet spin state. Photoelectron spectroscopy studies of the Sn$^-$ anion confirm the expected ground electronic state of the anion as a ^4S state.[83] Quantum chemical

calculations for $[Sn(CO_2)_n]^-$ consistently show that doublet spin structures are 400 meV lower in energy than similar clusters with quartet spin. In addition, several stable cluster geometries with doublet spin dissociate into a Sn^- solvated by multiple neutral CO_2 species when calculated with quartet spin. It is likely that the discrepancy between the ground state spin of the Sn anion and the spin state predicted by our calculations for $[Sn(CO_2)_n]^-$ clusters is due to the interaction between the Sn atom and the CO_2 ligands breaking the symmetry of the 5p orbitals on the metal. This would allow the doublet state to be stabilized in the complex. This behavior is analogous to Sn_n^- clusters, where already the dimer, Sn_2^-, has a doublet ground state.[84,85]

A summary of the calculated structures with chemical formula $[Sn(CO_2)_2]^-$ along with relative energies is shown in Figure 4.2. Inspection of the experimental spectrum for $[Sn(CO_2)_2]^-$ reveals two high intensity features at 1640 cm^{-1} and 1840 cm^{-1} with lower intensity features at 1269 cm^{-1} and 1178 cm^{-1}. The asymmetric stretching region of neutral CO_2 also features a very low intensity signature at 2333 cm^{-1} which signals that some of the clusters at this size must be composed of a $[SnCO_2]^-$ core ion and a solvent CO_2 species.
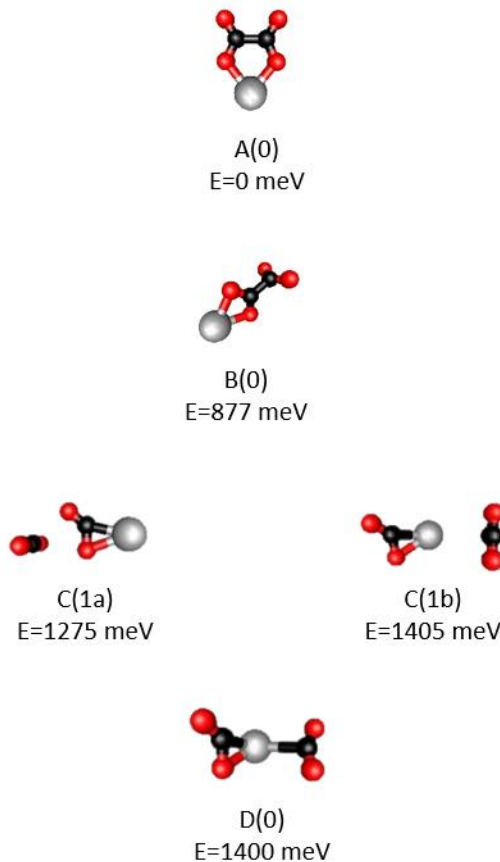
Figure 4.2. Calculated cluster geometries of $[Sn(CO_2)_2]^-$. Calculations were performed based on the methods described in Chapter 2. Clusters are labeled based on core ion geometry (capital letter), number of solvent CO_2 species (number) and solvent configuration (lower case letter) according to increasing relative energy.

The lowest energy structures at this cluster size feature a Sn metal center bound to a planar oxalate ion [A(0)] similar to the structures observed in $[Bi(CO_2)_n]^-$ cluster anions (Chapter 3).[81] The next highest energy cluster configuration also features a C_2O_4 ligand [B(0)], except that it is bound to the metal in a nonplanar configuration. Since we require the presence of at least one weakly bound CO_2 molecule in order to detect absorption events, structures A(0) and B(0) can be safely excluded from contributing to the experimental spectrum of $[Sn(CO_2)_2]^-$. We can do this because the binding energy of CO_2 ligands to the metal center are much higher (of the order of

10^4 cm^{-1}) than the photon energies used in the experiment. It is highly likely that these two isomers are present in the molecular beam at this cluster size. The calculated vibrational spectra of the remaining structures are compared to the experimental spectrum in Figure 4.3.
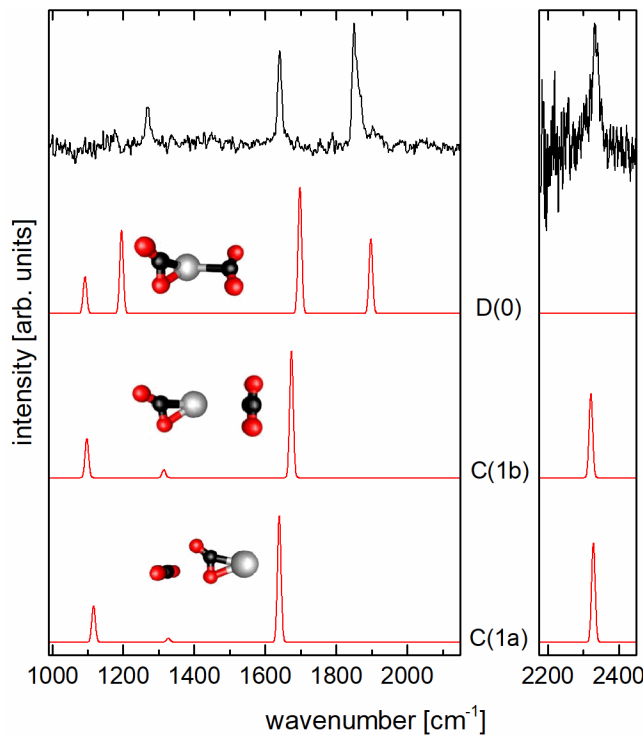
Figure 4.3. A comparison of calculated vibrational spectra (red) with the experimental spectrum of $[Sn(CO_2)_2]^-$. The intensity of the solvent signatures is approximately 6–10 times weaker than the feature at 1850 cm^{-1}.

The remaining two cluster structures feature bidentate η^2-(C,O) CO_2 ligands with either a solvent CO_2 species at the metal or behind the ligand [C(1a) or C(1b)] or accompanied by a monodentate η^1-C bound CO_2 ligand similar to that discussed in Chapter 3 [D(0)]. The presence of these high energy isomers at this cluster size suggests that they are kinetically trapped species, indicating that since the collisional cooling rate of the ions is faster than the isomerization rate. Based on the calculated vibrational frequencies, the experimental signatures are assigned as follows (see Table 4.1 for a summary).

Table 4.1. Spectral assignments of the experimental bands at $n = 2$ compared to predicted vibrational frequencies.

observed [cm^{-1}]	mainly contributing core ion and vibrational mode	predicted [cm^{-1}]
1178	D, symmetric CO stretch of η^2-(C,O) ligand	1092
1269	D, symmetric carboxylate CO stretch	1196
1640	D, asymmetric CO stretch of η^2-(C,O) ligand	1698
1850	D, antisymmetric carboxylate CO stretch	1898
2333	C, antisymmetric CO stretch of solvent	2326[a]

[a] Average value of isomers C(1a) and C(1b).

The η^2-(C,O) binding motif is common to core ion structures C and D. The asymmetric CO_2 stretching motion of this ligand is predicted to be close in frequency to the experimental signature at 1640 cm^{-1}. We assign this band to the asymmetric CO_2 stretching mode of a η^2-(C,O) CO_2 ligand. The symmetric CO_2 stretching mode of this ligand is predicted to appear around 1100 cm^{-1} and is likely responsible for the weak spectral signature at 1178 cm^{-1}. It is evident that vibrational motions of the η^2-(C,O) ligand do not account for the experimental signatures at 1850 cm^{-1} and 1269 cm^{-1}.

Comparison of the calculated vibrational frequencies of structure D(0) with the experimental spectrum shows that one of the vibrations of this structure recovers the experimental signature at 1850 cm^{-1}. We assign this experimental feature to the asymmetric CO_2 stretching motion of the carboxylate ligand. The symmetric CO_2 stretching mode is assigned to the experimental band at 1269 cm^{-1}. Based on the assignments discussed, it is clear that structure D(0)

is the main contributor to the experimental signatures at this cluster size. This is contrary to the presence of the vibrational signature at 2333 cm^{-1}, which indicates the presence of a weakly bound CO_2 solvent species. Since structure D is not compatible with this signature, there must be some amount of structures C(1a) or C(1b) also present in the molecular beam. The low signal-to-noise ratio of the peak at 2333 cm^{-1}, especially compared to analogous transitions at the same cluster size in Chapters 3 and 5, suggests that a very small fraction of the experimentally observable ion population have a solvent CO_2 molecule. The determination of a ratio between clusters with core ion C or D present in the molecular beam is not straightforward since there is no spectral overlap between the two spectral regions examined. Based on the raw ion intensities and typical laser pulse energies, we estimate that the band at 2333 cm^{-1} is roughly a factor of 6-10 times weaker than the band at 1850 cm^{-1}. This makes it very unlikely that we would be able to observe vibrational signatures of the corresponding core ions in the experimental spectrum.

The ability to observe photodissociation of cluster structure D(0) is a testament to how weakly bound the carboxylate ligand is to the metal center. The calculated bond dissociation energy of the Sn-C bond of the carboxylate ligand is around 1500 cm^{-1}. This suggests that a single infrared photon in the wavenumber range of this experiment should be able to dissociate that bond. The intensities of vibrational signatures with lower wavenumber will be suppressed as discussed above.

Similar to the case of Bi-CO_2, the interaction of the η^1-C bound CO_2 ligand with the metal results in charge donation from the metal center to the ligand. The presence of excess electronic charge lengthens the C–O bonds and results in a red shift of the asymmetric CO_2 stretching mode compared to the same mode in neutral CO_2. Compared to other η^1-C bound CO_2 ligands, the Sn-C bond is about a factor of two weaker than the bonds observed in Au-CO_2 cluster anions.[72,86] This

is likely due to the presence of the η^2-(C,O) ligand. Natural population analysis shows that a majority of the excess charge (around -1.0 e) is localized onto the η^2-(C,O) ligand in structure D(0). The carboxylate ligand has -0.41 e of charge localized onto it. This leaves an overall cationic Sn atom. In structure C(1a) the Sn atom is effectively neutral with nearly all of the electron density residing on the η^2-(C,O) ligand.

There is a remarkable similarity between structures C(1b) and D(0), where the only difference is the distance between the Sn and the carbon atom of the weakly bound CO_2 species. In order to understand the barrier toward interconversion between these two structures, we calculated a potential energy curve along the Sn-C bond distance (Figure 4.4).
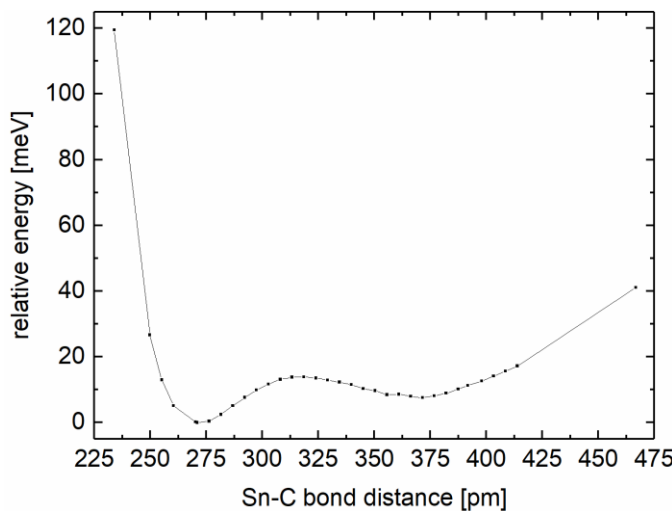
Figure 4.4. Calculated potential energy curve connecting structures D(0) and C(1b) along the Sn–C bond distance. All energies are relative to the lowest energy calculated data point and are corrected for zero point motion except for the Sn–C stretching mode.

It is clear that structures C(1b) and D(0) represent two minima along this potential energy surface. Structures C(1b) and D(0) represent CO_2 that is physisorbed and chemisorbed onto the $SnCO_2$ complex anion, respectively. The existence of physisorbed and chemisorbed CO_2 onto a Au anion has been observed by Bowen and coworkers using photoelectron spectroscopy.[87] The calculated

barrier to interconversion from D(0) to C(1b) is approximately 6 meV. This value is very low and would most likely correspond to rapid interconversion between structure D(0) and structure C(1b). One would therefore expect for the experimental spectrum to exhibit a broad spectral feature corresponding to species in the process of converting from structures D(0) and C(1b). However, the experimental spectrum has fairly narrow vibrational signatures corresponding only to structure D(0). A plausible explanation is that the barrier height for the interconversion of these two isomers is drastically underestimated by the calculation. Another explanation is that structure C(1b) simply does not exist, and the spectral feature at 2333 cm^{-1} is due solely to structure C(1a).

We note that the calculated values of the C–O bond lengths and the OCO bond angle vary smoothly along the Sn–C bond length, suggesting a gradual conversion of structure D(0) to structure C(1b). Examination of the highest occupied molecular orbitals (HOMOs) of structures D(0), C(1b) and the transition state show a gradual elongation of one of the Sn 5p orbitals as the CO_2 species moves closer to the metal center. Upon bond formation, there is strong mixing between the 5p orbital of the Sn with one of the π orbitals of the ligand CO_2. (See Figure 4.5).

Structure   Transition   Structure
C(1b)   State   D(0)
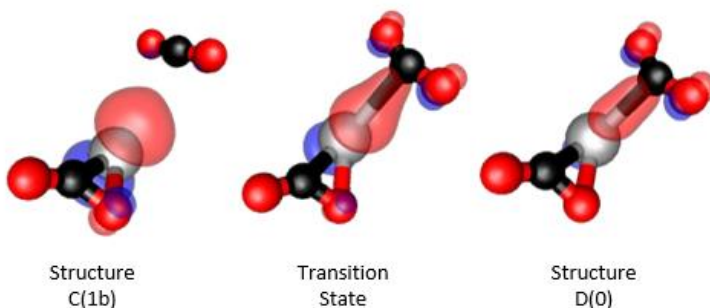
Figure 4.5. Calculated HOMO contours for different positions along the potential energy curve described in Figure 4.4. Contours are 70% of maximum orbital amplitude.

It is likely that the experimental spectrum of $[Sn(CO_2)_2]^-$ does not represent the overall distribution of different cluster structures, since the lowest energy isomers will not dissociate after absorbing a single infrared photon. The clusters that do dissociate at this cluster size provide insight into how CO_2 molecules interact with an undercoordinated Sn atom in the presence of an excess electron, i.e., under reducing conditions. As stated previously, gas phase cluster ions are interesting model systems for the interaction of CO_2 with strongly charged corner sites. The presence of isomer D(0) in the molecular beam demonstrates binding behavior that is unique to the Sn-CO_2 system and may be related to the efficiency of CO_2 reduction at Sn based electrodes.

Adding another CO_2 molecule to the clusters results in a large change in the experimentally observed infrared spectrum. The experimental spectrum contains three high intensity bands at 1625, 1678, and 1721 cm^{-1} with lower intensity bands at 1299 and 1323 cm^{-1}. The loss of the experimental signature at 1850 cm^{-1} suggests that clusters with core ion structure D are no longer major contributors to the experimentally observed signatures. The overall increase in the signal-to-noise ratio of the CO_2 solvent signature compared to cluster size $n = 2$, implies that most if not all of the structures contributing to the experimental spectrum contain at least one weakly bound CO_2 species. A summary of the calculated structures and relative energies at this cluster size is shown in Figure 4.6. A comparison of the calculated vibrational spectra to the experimental spectrum is provided in Figure 4.7, and a summary of the spectral assignments can be found in Table 4.2.
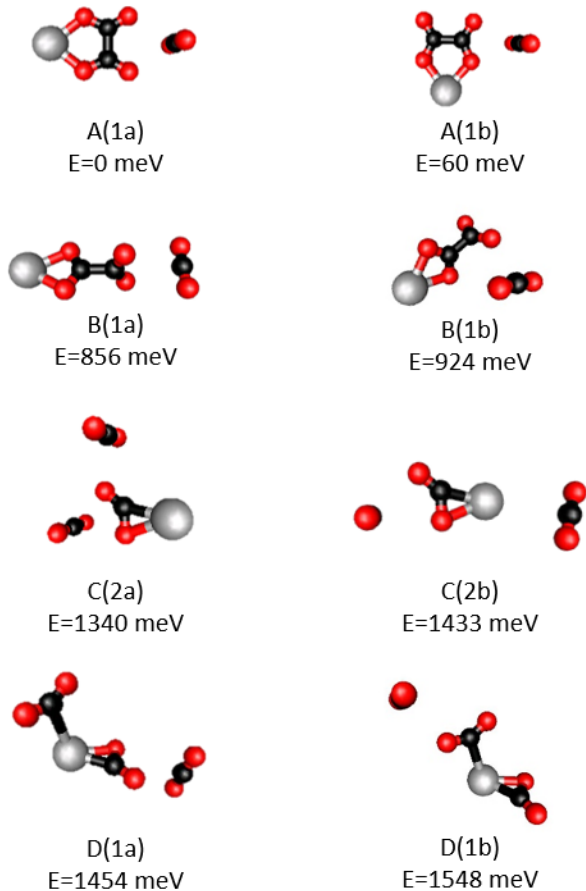
Figure 4.6. Calculated cluster structures for $[Sn(CO_2)_3]^-$. The cluster labeling procedure is described in Figure 4.2, and calculations were performed as described in Chapter 2.
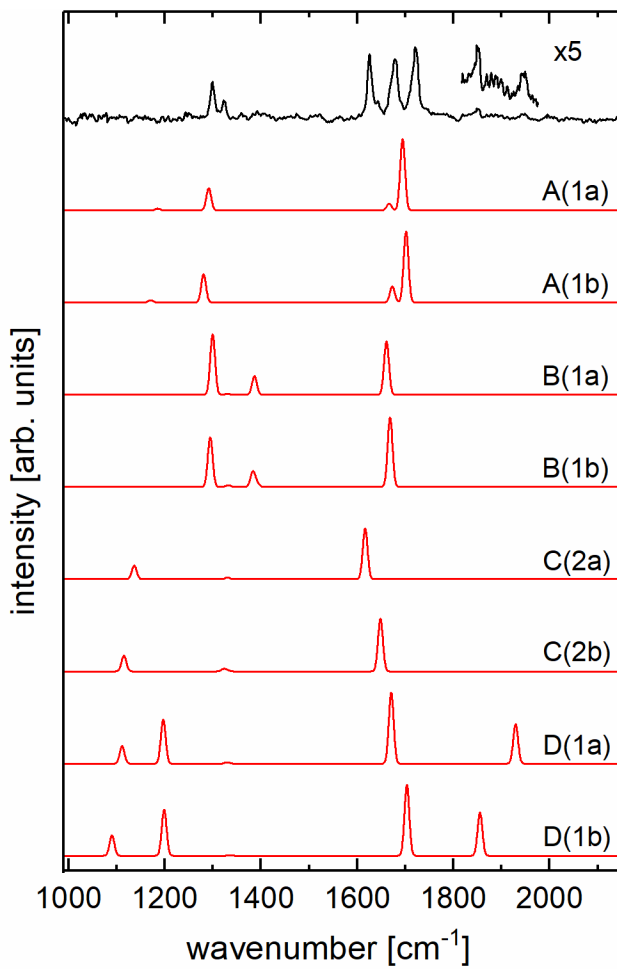
Figure 4.7. Comparison between the experimental spectrum of $[Sn(CO_2)_3]^-$ (black) and calculated vibrational spectra (red). Calculated traces are labeled by cluster structure. The region from 1816–1975 cm^{-1} is enhanced by a factor of 5 to highlight two low intensity bands in that region.

Table 4.2. Spectral assignments for $n = 3$ compared to predicted frequencies.

observed [cm^{-1}]	mainly contributing core ion and vibrational mode	predicted[a] [cm^{-1}]
1299	A, in-phase combination of metal-bound CO stretches	1286
1323	B, out-of-phase combination of symmetric CO_2 stretches	1297
1625	C, asymmetric CO_2 stretch, structure C(2a)	1616
1678	B, antisymmetric stretch of free CO_2 subunit	1664
1721	A, in-phase combination of free CO stretches	1698
1850	D, antisymmetric carboxylate CO_2 stretch, structure D(1b)	1855
1945	D, antisymmetric carboxylate CO_2 stretch, structure D(1a)	1929

[a] Unless assigned to specific solvent isomers, average values of different solvent isomers are reported

As stated above, the loss of the spectral feature at 1850 cm^{-1} in the spectrum of $[Sn(CO_2)_3]^-$ would seem to suggest that structures D(1a) and D(1b) are not present at this cluster size. However, a close examination of the experimental spectrum of $[Sn(CO_2)_3]^-$ reveals two very weak features at 1850 and 1945 cm^{-1} that correspond to the asymmetric CO_2 stretching mode of the carboxylate ligand of core ion D. The position of this band is directly related to the position of the solvent species relative to the carboxylate ligand, and results in shifts similar to other metalloformate complexes.[29-31,81] The loss of intensity of these modes informs on the stability of structures D(1a) and D(1b) compared to structure C(1b). Solvation of structure D(0) at the η^2-(C,O) ligand results in charge polarization out of the carboxylate ligand. This further weakens the already very weak Sn–C σ bond of the carboxylate ligand, making it more likely that isomerization to structure C(1b) occurs.

The experimental signature at 1625 cm^{-1} can in principle be due to clusters with core ion C or core ion D. Given the discussion above and the intensity of the signatures at 1850 and 1945 cm^{-1}, it is unlikely that structures D(1a) or D(1b) contribute significantly to the intensity of the feature at 1625 cm^{-1}. Structures C(2a) and C(2b) each represent different solvation positions around core ion C, where both solvents are behind the metal bound CO_2 ligand, or there is one solvent each at the ligand position and beside the metal atom. Based on the calculated vibrational spectra we assign the feature at 1625 cm^{-1} to the asymmetric stretching motion of the η^2-(C,O) ligand of core ion C. Specifically, cluster structure C(2a) matches the position of this band best. The same vibration in structure C(2b) most likely contributes to the experimental signature at 1678 cm^{-1}.

The addition of a third CO_2 molecule to the cluster allows for larger core ion structures to be solvated. This means that core ion structures A and B are observable. The individual CO_2 subunits of the C_2O_4 ligand in core ion structure A are equivalent. This equivalence results in coupling of free and metal bound C–O stretching motions into in-phase and out-of-phase combinations. We assign the vibrational signature at 1721 cm^{-1} to the in-phase combination of free C–O stretching motions of structures A(1a) and A(1b). Similar to the case of Bi-oxalate complexes, the out-of-phase combination of free C–O stretching motions is not predicted to have significant infrared intensity. We assign the in-phase combination of metal-bound C–O stretching motions to the experimental signature at 1299 cm^{-1}.

In core ion structure B, rotation about the C–C bond is not hindered by the presence of the metal atom. This results in a twisted configuration where the partially negative oxygen atoms repel each other, resulting in a rotation of the free CO_2 moiety of 90˚. This core ion geometry is similar to the observed structure of $MgCO_2Cl^-$ examined by Asmis and coworkers.[88] In that structure, the

CO_2 ligand binds to the Mg atom through both of its oxygen atoms; this results in a carbene type structure featuring a highly nucleophilic carbon atom. Structure B likely comes about as a result of a nucleophilic attack by this carbon atom onto the carbon atom of a second CO_2 molecule (the carbon atom in neutral CO_2 is slightly positively charged). Unlike in core ion structure A, the two CO_2 subunits that make up the C_2O_4 ligand are not equivalent. In fact, there is a significant difference in the OCO bond angle of the free CO_2 subunit (132°) and the metal bound CO_2 subunit (116°). This difference in OCO bond angle results in a predicted splitting of the asymmetric CO_2 stretching modes of 279 cm^{-1}. This is remarkable, considering that each CO_2 subunit has approximately the same amount of charge associated with it. We assign the experimental signature at 1678 cm^{-1} to the asymmetric CO_2 stretching motion of the free CO_2 subunit. The signature of the asymmetric CO_2 stretching motion of the metal bound CO_2 subunit is predicted to occur around 1385 cm^{-1}. The experimental signature corresponding to this band is likely suppressed due to the binding energy of a CO_2 solvent species to this core ion. However, a compatible experimental feature does appear for larger cluster sizes. Surprisingly, unlike the asymmetric stretching motions, the symmetric CO_2 stretching motions are strongly coupled between the two CO_2 subunits. We assign the experimental signature at 1323 cm^{-1} to the out-of-phase combination of symmetric CO_2 stretching motions. The in-phase combination of these motions is predicted to have no infrared intensity and is not observed in the experimental spectrum.

Unlike the behavior observed for $[Bi(CO_2)_n]^-$ cluster ions, there does not appear to be any change in position of any of the signatures as cluster size increases.[81] There is a reduction of the intensity of the band at 1625 cm^{-1} that could correspond to isomerization of core ion structure C into either core ion A or B.

The observation of high-energy isomers is an indication that these isomers are kinetically trapped due to significant barriers toward isomerization. This behavior has been seen previously in other metal-CO_2 cluster ions.[31,69,70,82] In order to estimate the barrier toward isomerization for structure B to structure A, exploratory calculations were performed along the Sn–C–O bond angle. Based on these calculations, the barrier toward isomerization of core ion structure B to structure A is predicted to be approximately 725 meV.

4.3 Conclusions

The structures of core ions found in $[Sn(CO_2)_n]^-$ cluster ions were determined using photodissociation spectroscopy in concert with quantum chemical calculations. For $[Sn(CO_2)_2]^-$ clusters, the dominant core ion geometry that contributes to the experimental spectrum is a unique structure featuring two CO_2 units bound to the metal center with η^2-(C,O) and an η^1-C binding motifs. The η^1-C CO_2 ligand is very weakly bound to the metal atom (bond dissociation energy predicted to be approximately 1500 cm^{-1}). For clusters with $n \geq 3$, a plurality of clusters are comprised of planar and nonplanar Sn-oxalate core ions and a η^2-(C,O) Sn-CO_2 core ion. For large cluster sizes, it is likely that the η^2-(C,O) Sn-CO_2 core ion isomerizes into either of the Sn-oxalate structures. Unlike Bi-CO_2 cluster ions, Sn-CO_2 core ions do not readily form metalloformate structures, despite both Bi and Sn being p-block metals.[81]

Chapter 5

Interactions of CO_2 with Fe and Mn: Formation of Complex and Diverse Core Ions

This chapter has been adapted with permission from the following previously published articles:

Thompson, M. C., Dodson, L. G., Weber, J. M., "Structural Motifs of $[Fe(CO_2)_n]^-$ Clusters (n = 3–7)." Journal of Physical Chemistry A, 2017. 121: p.4132–4138. DOI: 10.1021/acs.jpca.7b02742. Copyright 2017 American Chemical Society.

Thompson, M. C., Ramsay, J., Weber, J. M., "Interaction of CO_2 with Atomic Manganese in the Presence of an Excess Negative Charge Probed by Infrared Spectroscopy of $[Mn(CO_2)_n]^-$ Clusters." Journal of Physical Chemistry A, 2017. 121: p.7534–7542. DOI: 10.1021/acs.jpca.7b06870. Copyright 2017 American Chemical Society.

5.1 Introduction

The interaction of CO_2 with transition metals is important both in the context of CO_2 reduction catalysis as well as from a fundamental perspective.[4,89,90] The electrochemical reduction of CO_2 has many applications towards the sequestration or recycling of CO_2 in a carbon neutral fuel cycle.[5,91,92] While the coinage metals have shown promise as materials for heterogeneous catalytic conversion of CO_2 to CO, transition metals outside of group 9 have not displayed the selectivity of these materials for CO formation. In many cases, homogeneous catalysts containing first row transition metals have higher selectivities for CO formation compared to heterogeneous analogues.[4]

The continued interest in first row transition metal based catalytic materials is due to their relatively large abundances compared to traditional electrode materials. Infrared studies of cationic metal–CO_2 systems have shown primarily metal oxygen interactions between the metal cation and CO_2 neutral species.[93-100] These interactions are largely electrostatic in nature and often result in negligible charge transfer to the CO_2 species. Anionic clusters of a metal atom and CO_2 exhibit a

much richer collection of interactions. In many cases, strong M–C and M–O bonds are formed resulting in a wide variety of structural motifs.[31,79,80] In contrast to earlier work by Knurr et al.,[79,80] the systems discussed in the following sections exhibit many different ligand binding motifs between metal and CO_2 ligands.

5.2 $[Fe(CO_2)_n]^-$ Results and Discussion

In an effort to characterize the interactions of CO_2 with an Fe atom in the presence of an excess electron, photodissociation spectroscopy was performed on $[Fe(CO_2)_n]^-$ cluster ions . The experimental spectra are presented in two spectral regions (990–2150 and 2175–2450 cm^{-1}, see Figure 5.1); signatures in the higher wavenumber region are due to CO_2 species that are solvating the core ion, while signatures in the lower wavenumber region are primarily due to reduced CO stretching motions of CO_2 ligands in the core ion. As discussed previously, the presence of a weakly bound solvent species is necessary for our technique to detect laser-induced photodissociation on the timescale of the experiment. As observed in $[M(CO_2)_n]^-$ (M=Au, Ag, Cu, Co, Ni, Sn, and Bi), CO_2 ligands are bound from anywhere between 4000 cm^{-1} to as high as 10^4 cm^{-1}.[29-31,79-81] This precludes observation of laser-induced dissociation of CO_2 ligand species at the photon energies used in this experiment. There was no observed photodissociation action from cluster sizes smaller than $n = 3$. This suggests that the smallest stable core ion present in the molecular beam has stoichiometry $[Fe(CO_2)_2]^-$.
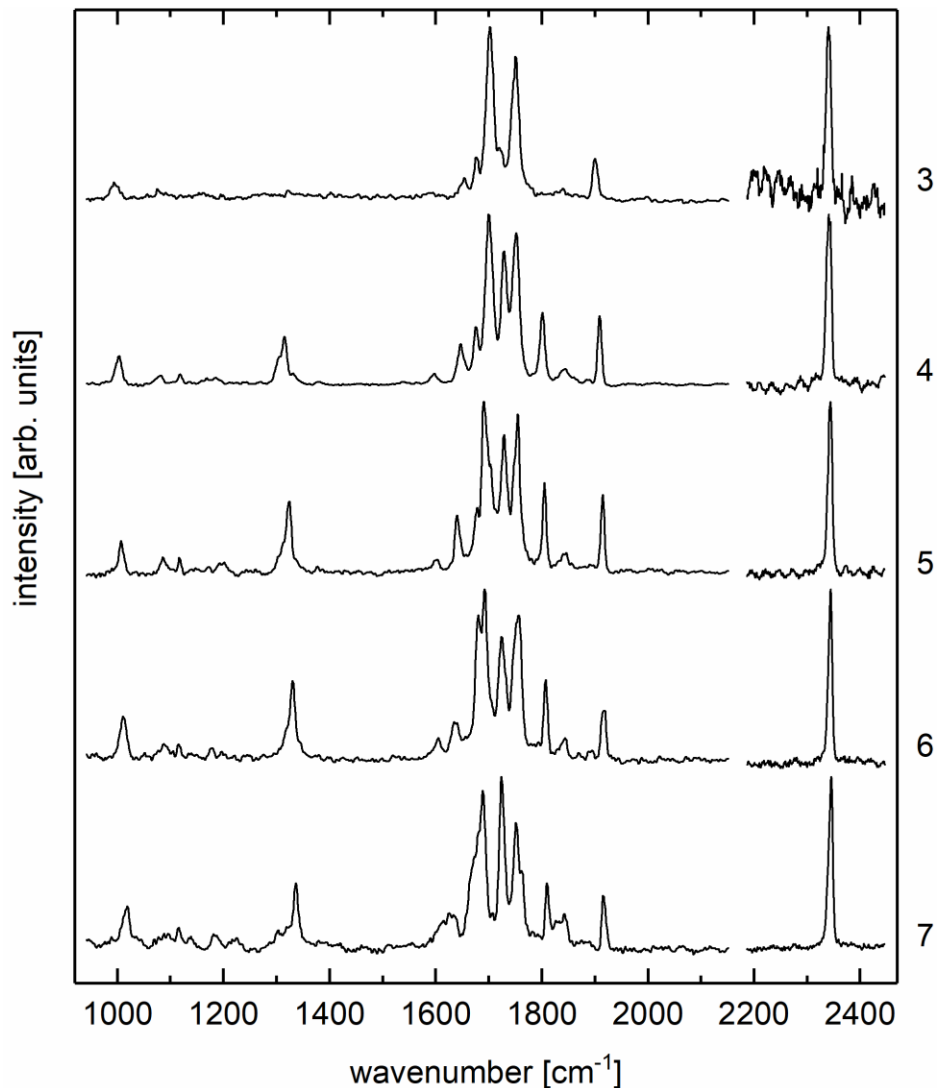
Figure 5.1. Experimental spectra of $[Fe(CO_2)_n]^-$ cluster ions. The numbers along the right hand side indicate the number of CO_2 species in the cluster (n). Spectra in the asymmetric stretching region of neutral CO_2 were taken over a single day and are shown to demonstrate the presence of at least one solvent CO_2 species.

As before, the interpretation of the experimental spectra is aided by quantum chemical calculations. A series of cluster geometries were generated based on chemical intuition and then relaxed. Assignments were made by comparison of calculated vibrational frequencies to the experimental spectrum. A set of viable calculated cluster structures is shown in Figure 5.2.

A(1): 0 meV

D(1): 0 meV

B(1a): 892 meV

B(2b): 1155 meV

B(1b): 876 meV

B(2a): 1143 meV

C(1a): 915 meV

A(2): 147 meV

C(1b): 968 meV

C(2): 1151 meV

E(1): 1226 meV
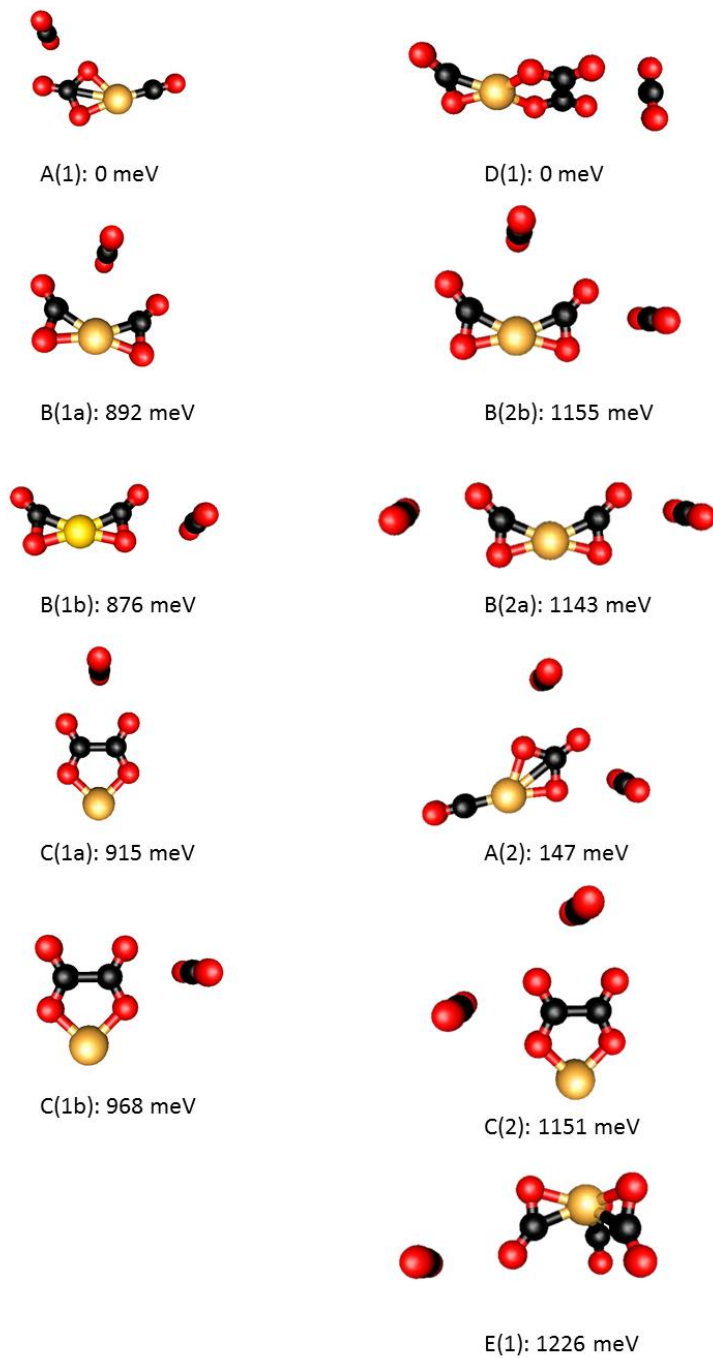
Figure 5.2. Calculated structures of $[Fe(CO_2)_3]^-$ (left) and $[Fe(CO_2)_4]^-$ (right). Calculations were performed as described in Chapter 2. Clusters are labeled based on core ion structure (capital letter), number of solvent species (number in parentheses) and solvent position (lower case letter in parentheses). All calculated structures are in the quartet spin state.

Based on the electron configuration of the Fe^- ($4s^2 3d^7$), $Fe–CO_2$ complex ions can have two possible spin states, doublet or quartet. Calculations show that doublet spin complexes lie approximately 1 eV higher in energy than quartet spin structures with the same geometry. This suggests that doublet spin complexes can relax through a spin-flip to a quartet state without large geometry changes. Similar transitions occur in other metal-organic complexes with lifetimes up to a microsecond.[101] An alternative is that the ions are formed via an Fe^- anion in its ^4F ground state.[102] The relatively short spin flip transition lifetime suggests that doublet $Fe–CO_2$ complexes formed in the ion source will not survive between formation and irradiation (milliseconds).

The smallest cluster that displays photodissociation action is $[Fe(CO_2)_3]^-$. The experimental spectrum (Figure 5.3) for this cluster features a group of peaks in the region from 1600–1750 cm^{-1}, a signature around 1900 cm^{-1}, and several features below 1300 cm^{-1}. The two large features at 1699 and 1749 cm^{-1} are assigned to the in-phase and out-of-phase combination of asymmetric CO stretching vibrations in structures B(1a) and B(1b). Core ion geometry B features two CO_2 ligands each bound to the metal atom through the carbon atom and one of the oxygen atoms [η^2-(C,O)]. This core ion has C_{2v} symmetry, and its "butterfly" geometry has been seen previously in studies of CO_2 interactions with Co, Cu, and Ni.[31,79,80] As discussed in Chapter 1, when CO_2 accommodates excess charge, there is a large red shift in the asymmetric stretching frequency. Since the assigned CO stretches are red shifted by about 700 cm^{-1} compared to the neutral asymmetric CO stretching motion, the CO_2 ligands must be partially reduced. Natural population analysis confirms this assumption, finding that each CO_2 ligand contains about -0.89 e of charge (in the unsolvated complex). Kinetic coupling between individual CO_2 oscillations results in in-phase and out-of-phase combinations of CO_2 stretching motions in the complex. The higher energy feature (1749 cm^{-1}) is assigned to the in-phase combination of asymmetric CO_2

stretches, and the lower energy feature (1699 cm^{-1}) is due to the out-of-phase combination of asymmetric CO_2 stretches. Calculations show a third high intensity feature should be present around 1042 cm^{-1}, corresponding to the in-phase combination of symmetric CO_2 stretching motions. We assign this motion to the experimental signature at 993 cm^{-1}. As discussed in Chapter 3, features with energy far below the binding energy of a solvent CO_2 species (1400 cm^{-1}) do not readily dissociate a solvent species after absorption of a single photon in the time scale of the experiment. Only a small portion of the ion population will contain enough internal energy (after photon absorption) to dissociate on the timescale of the experiment. The suppression of the intensities of these features should diminish with increasing cluster size.
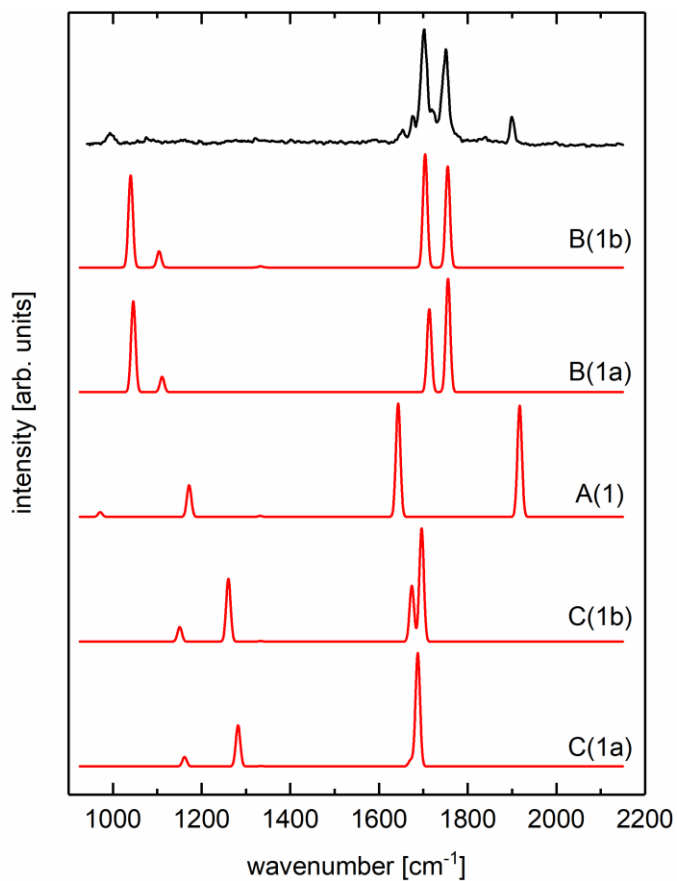
Figure 5.3. Comparison of the experimental spectrum of [Fe(CO$_2$)$_3$]$^{-}$ (black, top) to calculated IR spectra (red). Each trace is labeled according to the corresponding calculated structure (see Figure 5.2).

The feature at 1900 cm^{-1} is assigned to the CO stretching motion of structure A(1). The core ion consists of a carbonate ligand bound to the metal along with a carbonyl ligand on the opposite side. This geometry is only possible via insertion of the metal atom into a CO bond of CO_2. The CO_2 molecule has a CO bond energy of 525.9 kJ/mol,[103] so one would expect any insertion of a metal atom into one of the CO bonds would feature a fairly high energetic barrier. However, work by Dodson et al. has demonstrated that insertions of a Ti atom into a C–O bond of CO_2 occurs with a negligible barrier.[82] Unlike other transition metal-CO_2 systems studied, this insertion signature has significant intensity, indicating that structure A(1) is not a minor contributor to the experimental spectrum. There is an experimental signature at 1646 cm^{-1}, which is consistent with the calculated frequency of the asymmetric CO_2 stretching motion of the carbonate ligand of structure A(1).

A third possible core ion goemetry is an oxalate complex similar to others described previously in this thesis. Structures C(1a) and C(1b) represent two different clusters with the solvent species being to the side of the core ion or above the core ion, respectively. Calculated vibrational frequencies suggest that one of the two weak shoulders at 1653 and 1676 cm^{-1} could account for the symmetric combination of free CO stretches in the oxalate complex. Just as before, the asymmetric combination of free CO stretches is predicted to have negligible infrared intensity. The absence of a signature around 1350 cm^{-1} (corresponding to the symmetric combination of metal bound CO stretches) could be due to a suppression of this feature due to the binding energy of a solvent CO_2 species to this core ion. The author cannot rule out the presence of structures C(1a) or C(1b) in the molecular beam at this cluster size.

The coexistence of structural families A and B merits further discussion. In the absence of high barriers to isomerization, one would expect, on the timescale of the experiment, for all of the

clusters to relax to the global minimum geometry configuration, followed by CO_2 solvent evaporation as necessary to accommodate the resulting heat of reorganization. An examination of the relative binding energies of the bare complexes reveals that structure A(0) is roughly 1 eV lower in energy than structures B(0) and C(0). An evaluation of the bond insertion process with a smaller test system reveals a barrier to metal insertion of around 1.4 eV.[82] It is not surprising to find higher energy isomers populated for this system due to kinetic trapping. If the collisional cooling rates in the cluster source are faster than the isomerization rate, higher energy isomers can become kinetically trapped in higher lying potential wells.

Due to our detection scheme, the clusters need to have at least one weakly bound solvent species in order for absorption events to be detectable. For $[Fe(CO_2)_3]^-$ clusters, our experiment is not sensitive to core ions that have molecular formula $[Fe(CO_2)_3]^-$. This means that if these core ions are present in the molecular beam, they would only be detectable in the experimental spectra of larger cluster ions ($n \geq 4$). Examination of the experimental spectrum of $[Fe(CO_2)_4]^-$ reveals the appearance of several new features that could be due to larger core ion structures becoming detectable at this cluster size (Figure 5.4). Starting with signatures already identified as being vibrational modes of smaller core ion geometries, butterfly based clusters (B) and insertion based structures (A) are clearly still present. In these cases the positions of these signatures are slightly shifted due to solvent position affecting the charge distributions of the core ions.
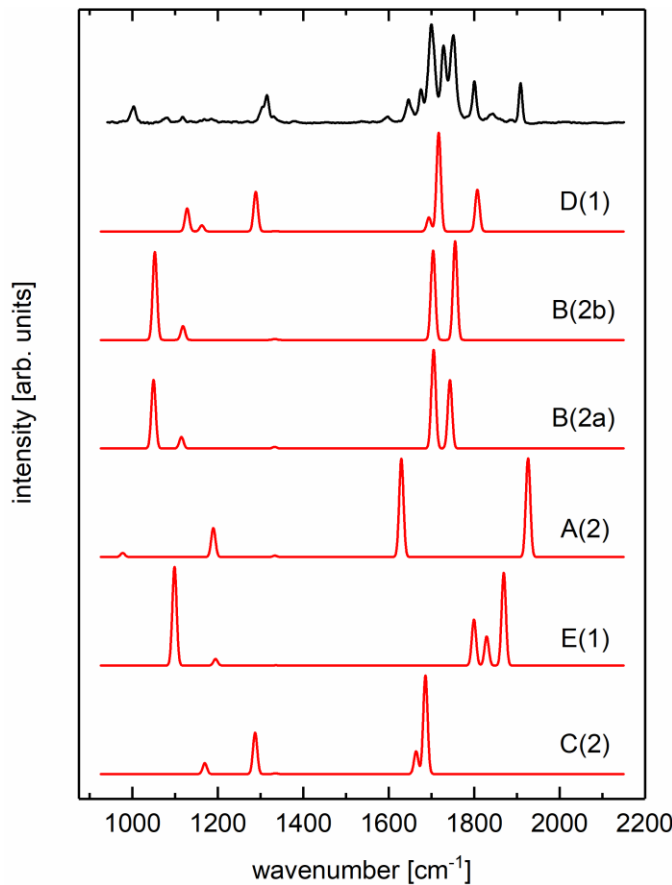
Figure 5.4. Comparison of the experimental spectrum of $[Fe(CO_2)_4]^-$ (black, top) to calculated IR spectra (red). Each trace is labeled according to the corresponding calculated structure (see Figure 5.2).

The viable calculated cluster geometries for this cluster size are shown in Figure 5.2. The lowest energy isomer is structure D(1). This geometry is very similar to structural family C, except for a third CO_2 species interacting with the metal atom. This CO_2 forms two bonds to the metal center, through the C atom and one of the O atoms. The η^2 (C,O) ligand ends up with a smaller proportion of charge on it compared to the same binding motif seen in the butterfly complexes. This results in structural family D being identifiable from family C by the presence of an asymmetric CO stretching signature around 1800 cm^{-1}. This is compatible with the experimental signature found at 1799 cm^{-1}. The other prominent new experimental signature at 1313 cm^{-1} can be assigned to the

symmetric combination of metal bound CO stretches in the oxalate ring, and is compatible with structure D(1) or possibly structures C(2a) and C(2b). The presence of the bidentate CO_2 ligand in structure D(1) results in a calculated blue shift of the oxalate signatures (as shown in the calculated spectra). This shift is due to charge migration out of the oxalate ring and into the bidentate CO_2 ligand. The bidentate ligand contains a smaller amount of charge (-0.68 e) compared to similar ligands in other complexes (-0.89 e). The relative position of the bidentate CO_2 asymmetric stretching signature of structure D(1) compared to comparable signatures in structural family B reflect this.

Several smaller features in the region from 1800–1900 cm^{-1} are seen in the experimental spectrum for $[Fe(CO_2)_4]^-$. These features can be attributed to combinations of asymmetric CO stretching motions of structure E(1). This core ion geometry is a trisbidentate species with C_{3v} symmetry where three CO_2 species are bound directly to the metal atom in an η^2 (C,O) motif. In the bare complex, each CO_2 ligand on average contains -0.64 e of charge. Upon solvation, the entire molecule skews toward the solvated side of the complex, breaking the C_{3v} symmetry and resulting in the solvated CO_2 ligand containing -0.68 e of charge. As was the case with the smaller cluster size, the sheer number of populated isomers suggests that many of them are kinetically trapped species.

Given the large number of spectral features and the variety of calculated core ion structures, it was useful to combine our calculated spectra to evaluate the overall fit of our calculations to the experimental spectrum. The combined calculated curve was generated by scaling the individual calculated traces using the experimental intensities of positively identified unique experimental signatures assigned to each core ion. As an example, the calculated spectrum of structure D(1) was

scaled to the intensity of the experimental signature at 1799 cm^{-1}. The calculated spectrum for this cluster size is compared to the experimental spectrum in Figure 5.5.
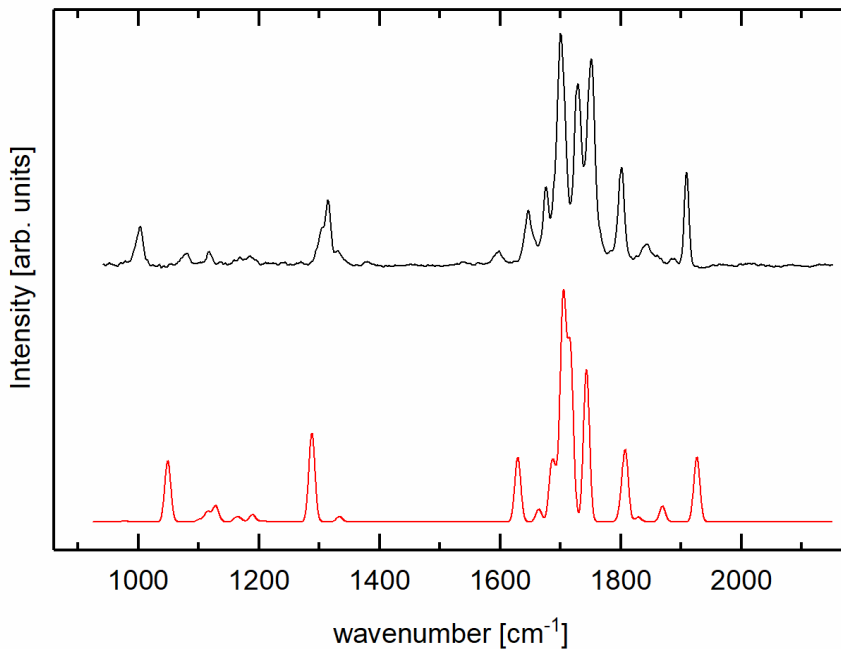
Figure 5.5. A composite of all calculated infrared spectra for $[Fe(CO_2)_4]^-$ clusters (red) compared to the experimental spectrum (black).

Surprisingly, this method reproduces the experimental signatures and intensities very well. This suggests that it is unlikely that any other core ion geometry is significantly populated at this cluster size. This also holds for larger cluster sizes, since no new signatures appear as cluster size increases.

Unlike other metal-CO_2 clusters discussed thus far, Fe-CO_2 clusters exhibit a large variety of core ion geometries. This is similar to previous studies of $[Cu(CO_2)_n]^-$, where the clusters exhibited many diverse core ion geometries.[31] An interesting note is that similar to other transition metal-CO_2 systems there were no observed core ions smaller than $[M(CO_2)_2]^-$.[69,79]

5.3 [Mn(CO₂)ₙ]⁻ Results and Discussion

Laser vaporization of a manganese target entrained into a supersonic expansion of CO_2 generated a series of $[Mn(CO_2)_n]^-$ (n=2–10) cluster ions. Unlike other metals discussed in this thesis, manganese does not exist as a stable anion (its electron affinity has never been measured but is predicted to be strongly negative).[104] If Mn^- were to be stable, it would have a valence electron configuration of $4s^2 3d^6$, isoelectronic with neutral atomic iron. This electron configuration is compatible with three spin configurations: quintet, triplet and singlet. Calculated cluster geometries consistently demonstrate that complexes with quintet spin configuration are the lowest energy isomers, in agreement with Hund's rules that would suggest $^5D_4$ as the ground state of the atomic anion.

Infrared photodissociation action spectra of $[Mn(CO_2)_n]^-$ (n = 2–10) are presented in Figure 5.6. For the smallest cluster size, the region from 1600–1700 cm^{-1} is relatively bare compared to the spectra for larger cluster sizes. As cluster size increases, the number of features in this region also dramatically increases for clusters larger than $[Mn(CO_2)_3]^-$. Complexity of the spectra of $[M(CO_2)_n]^-$ in this spectral range is not unusual, especially for clusters with first row transition metals, and can be indicative of either highly polarizable core ions, many different core ion geometries populated, or both.
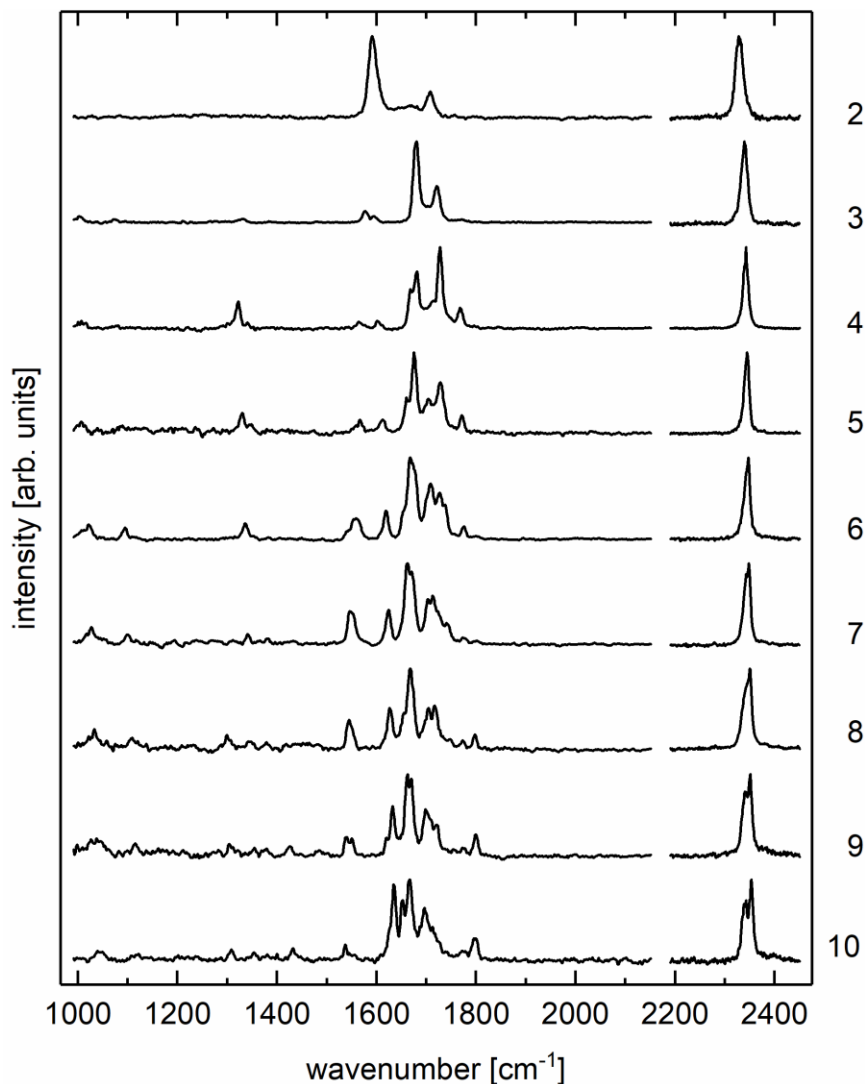
Figure 5.6. Experimental spectra of $[Mn(CO_2)_n]^-$ cluster ions. The numbers along the right hand side indicate the number of CO_2 species in the cluster (n).

Spectra are assigned based on comparison of calculated vibrational frequencies of proposed structures as described in Chapter 2. Starting with the smallest cluster size there are two features, one at 1592 cm^{-1} and another at 1710 cm^{-1}, with a broad feature between them. A summary of three stable cluster geometries, along with calculated vibrational spectra are shown in Figure 5.7.
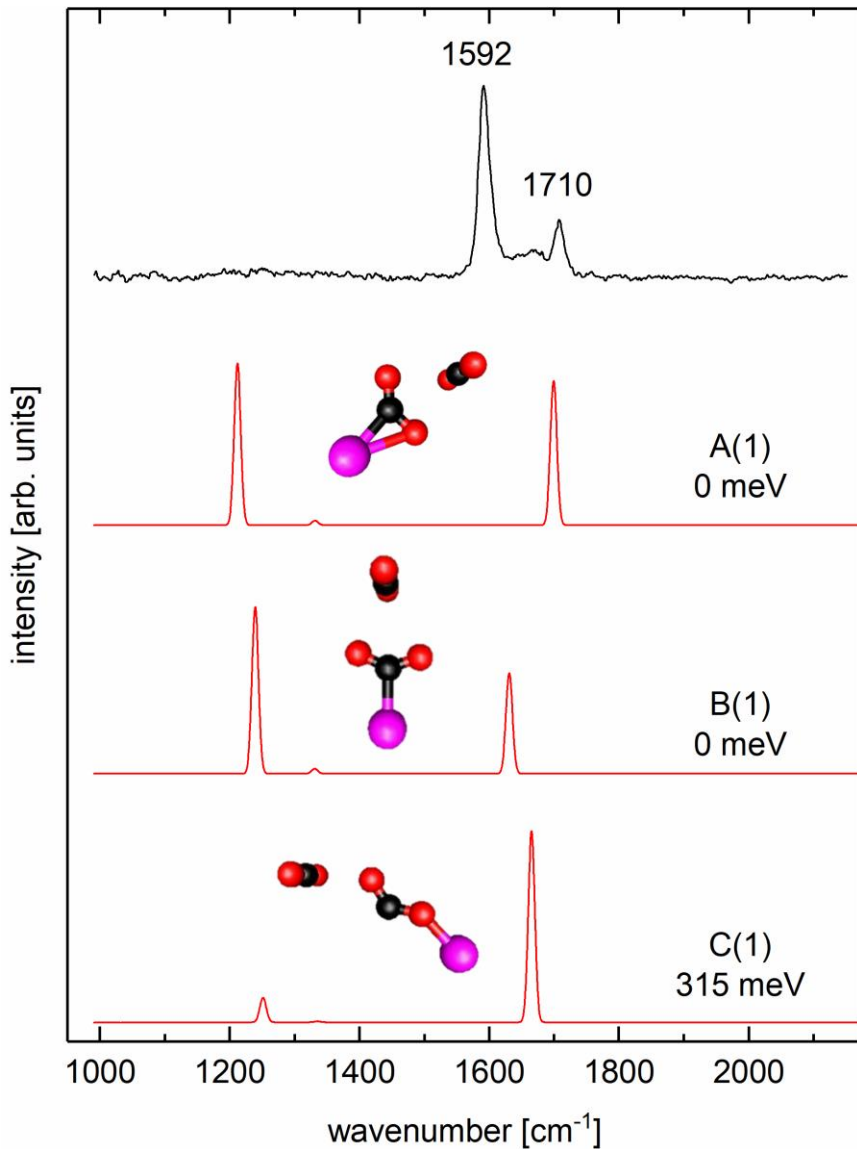
Figure 5.7. Comparison of the experimental spectrum of $[Mn(CO_2)_2]^-$ (top, black) to the calculated IR spectra of several isomers (red). Isomers are labeled based on the same method described in Figure 5.2. Energies are relative to the lowest energy calculated isomer.

Structure A(1) consists of a single CO_2 ligand bound in the η^2 (C,O) motif. In this particular cluster geometry, the CO_2 solvent species is directly behind the ligand. Structure B(1) consists of a carboxylate CO_2 ligand similar to what has been discussed previously. As in the case of structure A(1), the solvent species is located behind the CO_2 ligand. There is no spectroscopic evidence for either core ion species in any particular spin state. On energetic grounds, the quintet spin states are

roughly 1 eV lower in energy than the corresponding triplet spin analogue and around 2 eV lower in energy than the corresponding singlet spin analogue.

Based on vibrational frequency calculations of structures A(1) and B(1), the feature at 1710 cm^{-1} was assigned to the asymmetric CO stretching motion of structure A(1) and we assigned the feature at 1590 cm^{-1} to the asymmetric CO stretching motion of structure B(1). Structure C(1) could in principle also contribute to the peak at 1590 cm^{-1}. Structure C(1) features a CO_2 ligand bound to the Mn atom through one of its O atoms. The ligand is effectively a CO_2 anion, with a majority of the excess charge residing on the ligand. This structure is in contrast to the similar binding method of CO_2 in cationic clusters with metal atoms.[93-100,105] While in theory this species could contribute to the feature at 1590 cm^{-1}, further discussion will show that this species does not contribute to the experimental spectrum.

The nature of the broad signature between 1600 and 1700 cm^{-1} merits further discussion. Since no individual structure seems to recover this broad feature, a potential energy scan was performed along the C-Mn-O bond angle, calculating a potential energy curve along this coordinate (Figure 5.8).
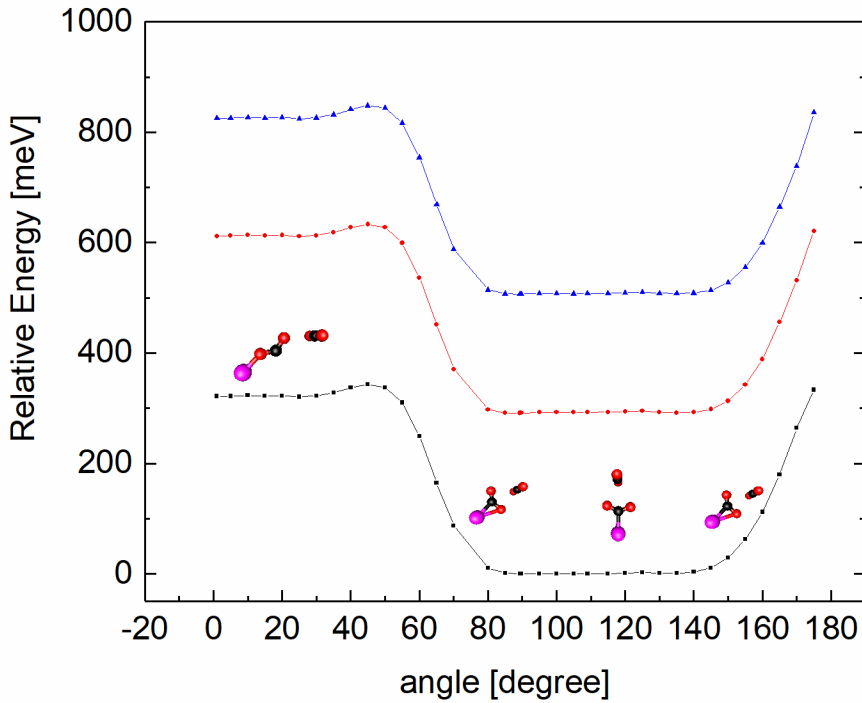
Figure 5.8. Potential energy curve along the C-Mn-O bond angle. The Born-Oppenheimer (black), vibrationally adiabatic ground state (red), and the vibrationally adiabatic excited state (blue) surfaces are shown, along with relevant structural figures.

By freezing the C-Mn-O bond angle and allowing all other degrees of freedom to relax, we can generate a Born-Oppenheimer potential energy surface in order to examine possible barriers to interconversion between the different quintet structures at this cluster size. Immediately apparent is the flat nature of the potential between 80 and 140 degrees. This suggests that interconversion between structures A(1) and B(1) will occur readily with no barrier. Structure C(1) has small barrier (25 meV) toward isomerization, suggesting that it will readily isomerize into either A(1) or B(1). This eliminates structure C(1) as a contributor to the experimentally observed signatures. Vibrationally adiabatic surfaces were calculated according to Equation 5.1:[86,106]

$$U_{ad,0}(\theta) = U_{BO}(\theta) + \frac{1}{2}\sum_J \hbar\omega_J. \tag{5.1}$$

The vibrationally adiabatic ground and excited surfaces are very similar to the Born-Oppenheimer surface. Both adiabatic surfaces were generated by summing over the two asymmetric CO stretching modes, since they are faster than the other vibrational modes of these species. The similarity between the three curves suggests that unresolved sequence bands could be responsible for the broad transition seen in the experimental spectrum.

It is interesting to note that in the absence of the solvent species, structure B(0) lies at the top of a 196 meV barrier along the C-Mn-O bond angle. Structure A(0) also lies 68 meV higher in energy than isomer C(0). This rearrangement of the relative energy of these three core ion isomers highlights the role of solvation in determining which core ions are observed in the experimental spectrum.

There are several differences between the experimental spectra for $[Mn(CO_2)_2]^-$ and $[Mn(CO_2)_3]^-$. Most notably is the relative absence of the high intensity feature at 1590 cm^{-1} in the smaller cluster size. Instead the spectrum of $[Mn(CO_2)_3]^-$ has two high intensity features at 1680 and 1724 cm^{-1}, and two weaker features around 1575 and 1594 cm^{-1}. There are also low intensity features at 1003 cm^{-1}, 1076 cm^{-1} and 1330 cm^{-1}. At this cluster size, vibrational signatures of molecular core ions that consist of two CO_2 ligands can now be detected. This drastically increases the number of possible geometries that need to be examined. A selection of these geometries as well as a comparison between calculated vibrational spectra and the experimental spectrum are shown in Figure 5.9 and Figure 5.10.
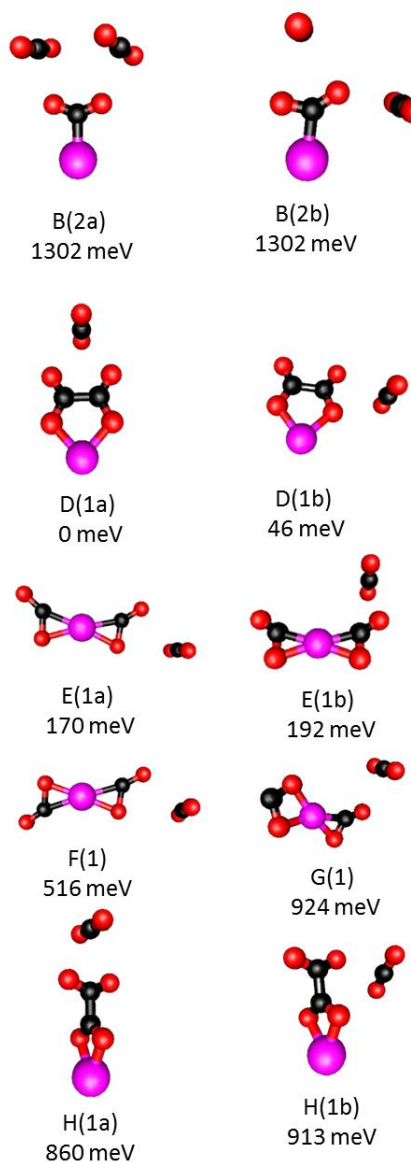
Figure 5.9. Calculated structures of $[Mn(CO_2)_3]^-$. Calculations were performed as described in Chapter 2. All calculated structures are in the quintet spin state.
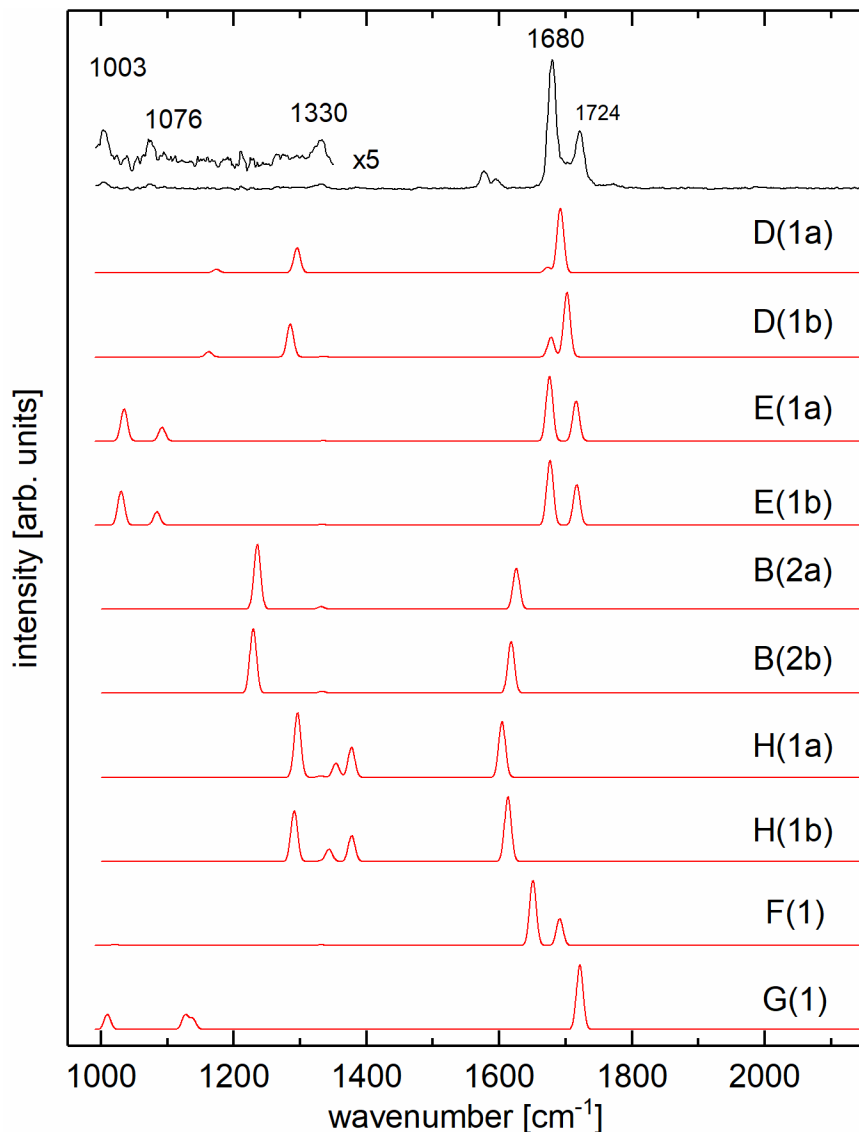
Figure 5.10. Comparison of the experimental spectrum of $[Mn(CO_2)_3]^-$ (top, black) to the calculated IR spectra of several isomers (red). Isomers are labeled based on the same method described in Figure 5.2. Energies are relative to the lowest energy calculated isomer.

The lowest energy calculated isomer at this cluster size is structural family D. This core ion has two CO_2 units forming a C-C bond and bonding to the metal atom through two oxygen atoms. This planar core ion geometry is a commonality in metal CO_2 chemistry, having been observed in several metal-CO_2 cluster systems (Fe, Ni, Cu, Bi, Sn).[31,70,80,81] Natural population analysis reveals that this core ion features a cationic Mn center (+0.5 e) with an almost dianionic

oxalate ligand (-1.5 e). The next higher energy structure is family E. The core ion in this case is a butterfly structure similar to what has been described in the previous section on $[Fe(CO_2)_n]^-$ clusters. Structural family E appears to recover the two main experimental features at 1680 and 1724 cm^{-1}. Also of note is that these structures also recover the two lowest energy features at 1003 and 1076 cm^{-1}. As a reminder, due to the binding energy of solvent CO_2 species to the core ions being higher than the energy of these transitions, absorption of a single photon may not result in evaporation on the timescale of the experiment for each ion. We can only detect the population of ions that have enough internal energy (combined with the absorbed photon energy) to evaporate a CO_2 species fast enough to be detected in our experiment. The low intensity feature observed at 1330 cm^{-1} can be assigned to the symmetric combination of metal bound CO stretches in the oxalate ligand of structural family D. This signature is also suppressed due to the binding energy of the solvent CO_2 species. Structures D(1a and b) also contribute to the intensity of the feature at 1680 cm^{-1}. Structure F(1) is an inverted butterfly structure with the same connectivity as core ion E. Given the potential energy surface calculated in Figure 5.8, it is likely that this high-energy isomer would readily isomerize to core ion structure E. Similarly, core ion structure G is also likely too high in energy to be populated. Given the narrow breadth of the spectral features it is unlikely that isomers E and F are coexisting in the beam. Similar to other first row transition metals, it does not appear that different solvation positions around the core ion geometries significantly affect the calculated vibrational frequencies. The exception is structural family D, whose asymmetric combination of free CO stretches gain infrared intensity upon solvation of the core ion from the side [D(1b)] compared to the top of the complex [D(1a)].

The nature of the peaks at 1575 and 1594 cm^{-1} is ambiguous. One could assume that these signatures could be due to structural families B or H, however; unlike in other cluster systems

where these structures have been seen (Bi and Sn), there is no trace of other vibrational signatures characteristic of these species. While such peaks would almost certainly be suppressed by the same effect that suppresses the other spectral features discussed above, the signatures should be apparent given the high signal-to-noise ratio of the experimental spectrum at this cluster size. As such, the origin of these two signatures remains ambiguous.

As mentioned earlier, $Mn-CO_2$ anionic complexes have three compatible spin configurations: singlet, triplet, and quintet, and unlike in the case of Fe and Bi, bare atomic manganese does not support an excess electron. This means that beyond relative energies, there is no intuitive way to determine which spin states are likely to be populated in our molecular beam. In the cases of structural families A, B, C, and D, there is no significant difference in the calculated vibrational frequencies of a cluster geometry as a function of spin state. Structural family E presents different calculated spectra as the spin state is changed. This is due to changes in the structure of the butterfly anion, primarily in the C-Mn-C bond angle, as a function of spin. As a result, the spin state of clusters with butterfly core ions can be determined by comparing the calculated vibrational frequencies of complexes in different spin states with the experimental spectrum (Figure 5.11). Direct comparison of the calculated spectra with the experimental spectrum shows that the quintet spin structure of the butterfly complex best matches the experimental spectrum, in both position and relative intensities. It is unlikely that other core ion geometries will exist with different spin states since each core ion geometry has approximately the same relative energy differences for each spin state.
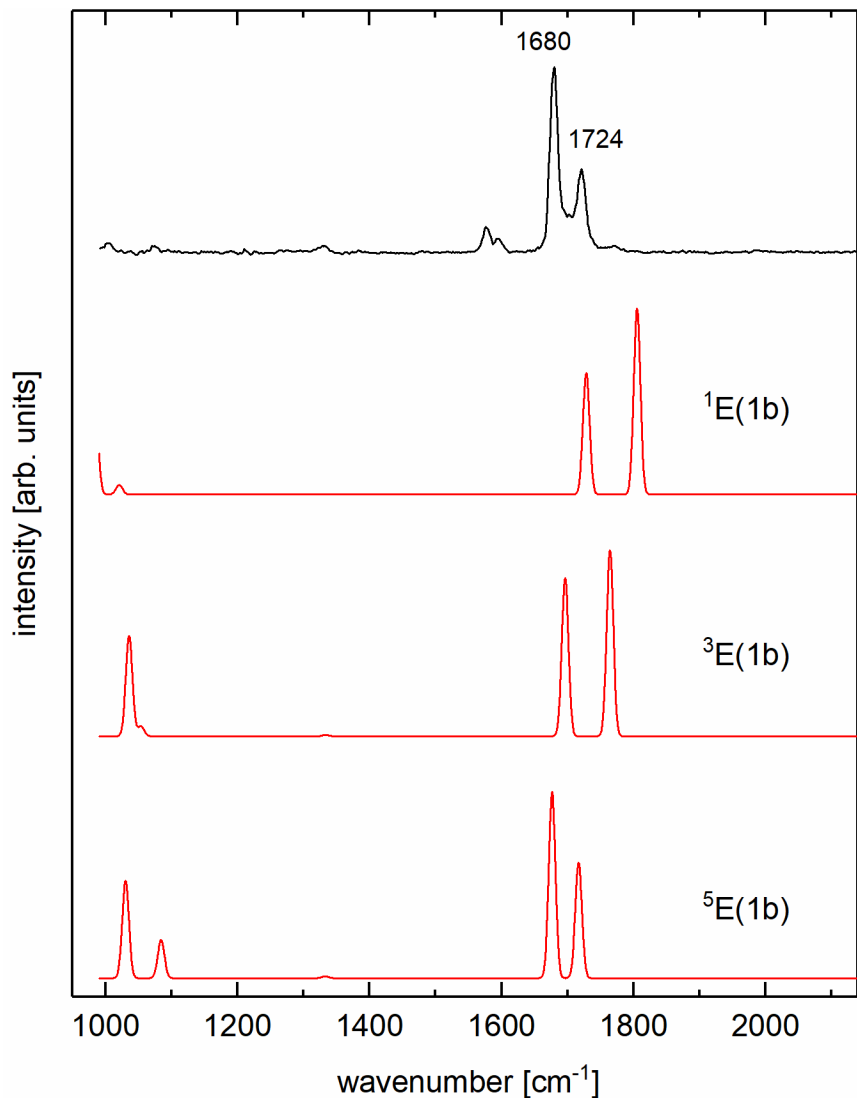
Figure 5.11. A comparison of the calculated IR spectra of different spin states (superscript number) of cluster geometry E(1b) [See Figure 5.7] with the experimental spectrum of $[Mn(CO_2)_3]^-$.

The addition of a fourth CO_2 molecule in the cluster results in an increase of the complexity seen in the experimental spectrum. New spectral features appear at 1321 cm^{-1} and 1777 cm^{-1}. The fourth CO_2 species allows for core ion structures of molecular formula $[Mn(CO_2)_3]^-$ to be detectable. Calculated cluster geometries, along with relative energies are shown in Figure 5.12.
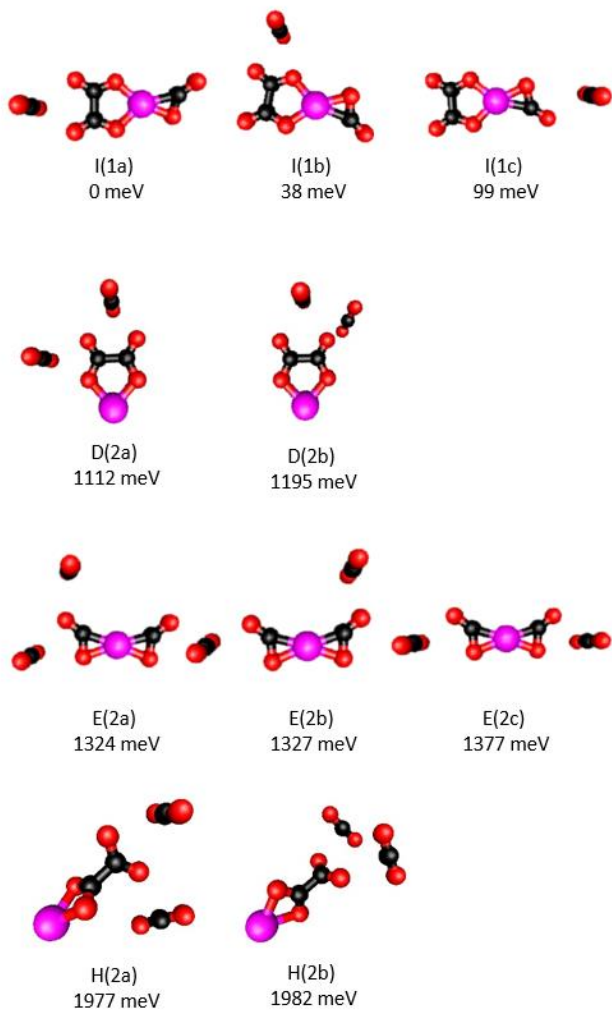
Figure 5.12. Calculated structures of $[Mn(CO_2)_4]^-$. Calculations were performed as described in Chapter 2. All calculated structures are in the quintet spin state.

The lowest energy cluster geometry at this cluster size features an oxalate bidentate core ion (structural family I). This core ion structure is very similar to structural family D except that a third CO_2 species has bonded to the metal atom through a carbon and one of its oxygen atoms. Comparison of calculated vibrational frequencies of clusters with this core ion, along with other calculated structures (see Figure 5.13), reveal that the new spectral feature at 1777 cm^{-1} could be due to the asymmetric stretching motion of the bidentate CO_2 ligand of core ion family I. There is

also excellent agreement with other experimental signatures from 1600–1750, due to in-phase and out-of-phase combinations of free CO stretching motions of the oxalate ligand. The signature at 1321 cm^{-1} is due to the in-phase combination of metal bound CO oscillations of the oxalate ligand. In principle, this transition could also be due to structural family D, since there is only a slight red shift of this signature in structures D(2a) and D(2b). The author notes that solvation of core ion family D at the metal position results in the formation of core ion family I. This suggests that core ion family D will not be present in larger cluster sizes, since the probability of solvation at the metal center increases with cluster size, as solvation positions around the oxalate ligand are filled.
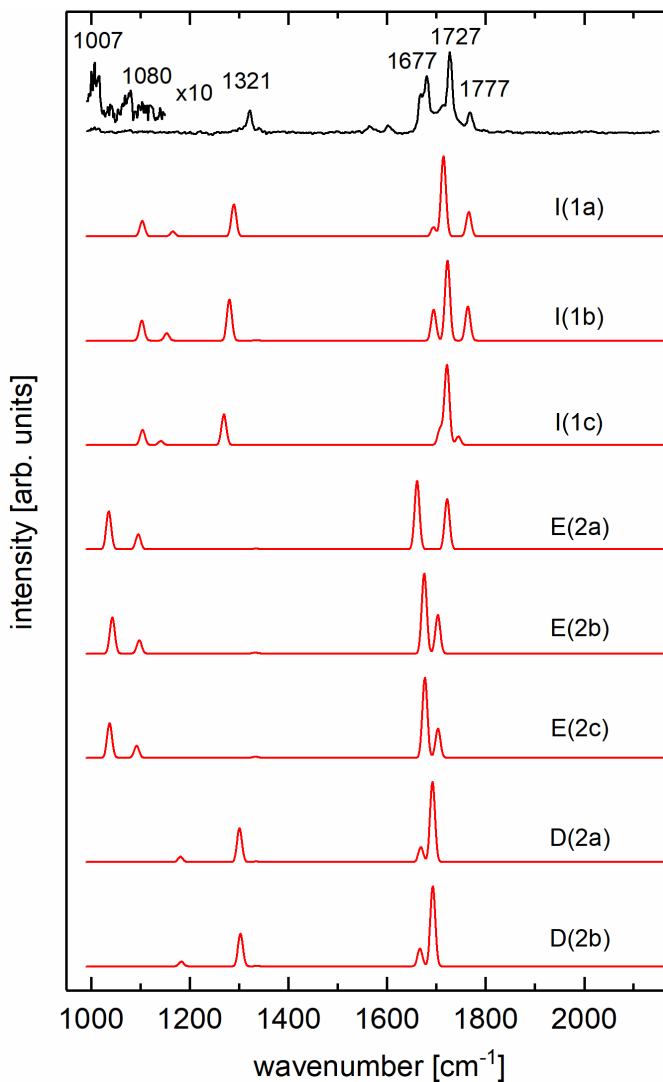
Figure 5.13 Comparison of the experimental spectrum of $[Mn(CO_2)_4]^-$ (black, top) to calculated IR spectra (red).

Clusters with the butterfly (structural family E) core ion geometry are responsible for much of the intensity in the region from 1600–1700 cm^{-1}. The low intensity features at 1007 and 1080 cm^{-1} are assigned to in-phase and out-of-phase combinations of symmetric CO stretching motions. Interestingly, the solvation environment around this core ion results in large change in the position of the two modes from 1600-1700. Asymmetric solvation around a single CO_2 ligand localizes a larger portion of the excess charge onto this ligand. This breaks the symmetry of the charge

distribution and changes the coupling of the oscillators. This results in the localization of oscillatory motion onto single CO_2 units, and is accompanied by an increase of the splitting between the two modes. Despite the fact that clusters with a butterfly core ion geometry are higher in energy than structural families I and D, clusters with butterfly core ion geometries contribute significantly to the experimental spectrum at this cluster size and are likely kinetically trapped. The assumption that structural family E is kinetically trapped is based on the fact that isomerization out of this core ion would require the Mn-C bond to break. Based on the calculated potential energy curve described above (Figure 5.8), this process is estimated to have a barrier of at least 352 meV. The low intensity signatures at 1562 and 1604 cm^{-1} could in principle be due to clusters with core ion geometry B (metalloformate) or could be due to structure H. However, since the symmetric CO_2 modes of these species are absent from the experimental spectrum it is unlikely that clusters with these two core ion geometries are present in the experiment.

Differences in the experimental spectra of larger Mn-CO_2 clusters are more subtle compared to the changes described for smaller clusters. In addition to small changes in peak position is the increase of the intensity of the features below 1400 cm^{-1}. This is due to decreasing solvent binding energies as cluster size increases. This will affect the spectra of smaller core ions more readily than for larger core ions due to the smaller ions having more solvent molecules at a given cluster size compared to the larger core ions. Calculations of clusters with five CO_2 species present show the formation of a new core ion structure with chemical formula [Mn(CO_2)$_4$]$^-$ (see Figure 5.14). Core ion J has four strongly bound CO_2 ligands, two pairs of which each form a C-C bond and bind into the metal center as planar C_2O_4 ligands. The symmetry of the core ion results in a simple calculated vibrational spectrum, with only two signatures which are compatible with the experimental signatures at 1330 and any of the number of peaks in the region from 1650-1750

cm^{-1} (See Figure 5.15). Two other isomers with similar structure have been calculated, with one or both of the oxalate ligands adopting a twisted configuration (Structures K(1) and L(1)). These structures lie at a minimum over 1 eV higher in energy than structure J and do not appear to match any unique experimental signature. The individual oxalate ligands of core ion J each have a calculated charge of -1.29 e with the Mn having a charge of +1.60 e. While the individual oxalate ligands are weakly charged compared to the oxalate ligand in core ion D (around -1.5 e), the combined presence of two of them results in significant oxidation of the Mn atom. In this structure, the charge of the Mn atom is considerably larger than the largest charge calculated for an Fe atom coordinated to multiple CO_2 species (+1.2 e). The author notes that other experimental signatures at this cluster size are due to different solvation positions around smaller core ions previously discussed.
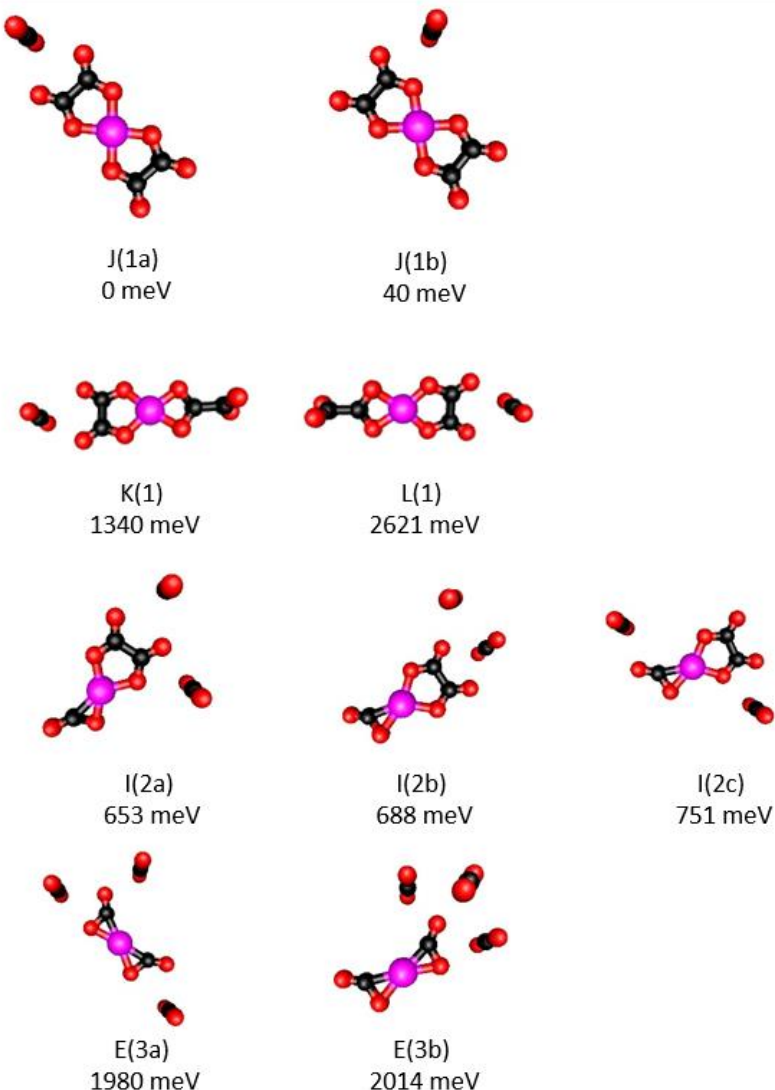
Figure 5.14. Calculated structures of $[Mn(CO_2)_5]^-$. Calculations were performed as described in Chapter 2. All calculated structures are in the quintet spin state.
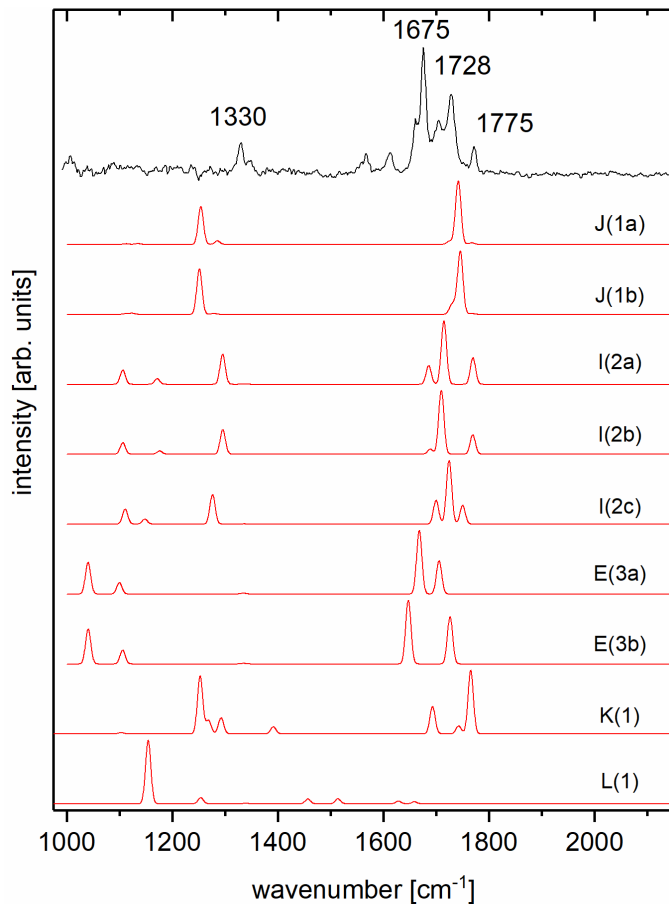
Figure 5.15. Comparison of the experimental spectrum of $[Mn(CO_2)_5]^-$ (black, top) to calculated IR spectra (red).

While the asymmetric CO_2 stretching region of neutral CO_2 is a vitally important metric to confirm the presence of weakly bound CO_2 species in the clusters, normally this region is uninteresting for the purpose of structural identification. Occasionally, this region can exhibit interesting signatures that can report on the nature of the core ion's interaction with solvent species.[29,30] Clusters smaller than $[Mn(CO_2)_6]^-$ have signatures in this region that show the presence of at least one neutral CO_2 molecule in the cluster. This signature blue shifts as cluster size increases, and is consistent with the behavior of all other metal-CO_2 anionic cluster species studied thus far. For clusters larger than this, there is a splitting that results in two different signatures, a signature that is red shifted from the asymmetric CO stretching frequency of 2349

cm^{-1} and a signature that is blue shifted from this value. A blue shift of the asymmetric CO stretching frequency is commonly seen in cationic metal CO_2 complexes due to complexation of the carbon dioxide molecule and the metal cation.[93-100,105] The overall shift is much weaker than that observed for metal bound CO_2 species in anionic metal-CO_2 systems because the binding is primarily a charge quadrupole interaction between the metal cation and the CO_2 with little to no charge sharing between the two.[93,107] It is theorized that the CO_2 species encounters a large repulsive potential barrier on the metal side of the complex, resulting in a blue shift of the asymmetric stretching frequency.[96] With these observations in mind, it is not unlikely that a CO_2 solvent species could weakly interact with a positive metal center of one of the core ions (the probability of this increases as solvation positions around the negatively charged ligands are occupied at larger cluster sizes). To test this theory, exploratory calculations of a $[Mn(CO_2)_9]^-$ cluster anion with a double oxalate core ion were performed. The converged configuration has a single solvent CO_2 species out of the plane of the ligands interacting with the metal cation center through one of the oxygen atoms (see Figure 5.16).
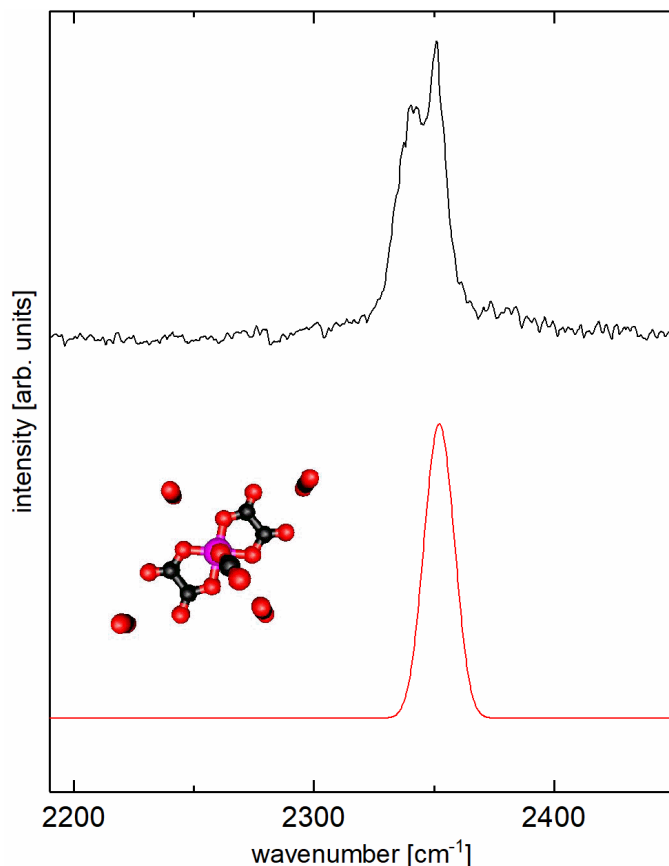
Figure 5.16. Exploratory structure and calculated spectrum for $[Mn(CO_2)_9]^-$.

5.4 Conclusions

The interactions of CO_2 with first row transition metals in the presence of an excess electron have proven to yield much richer chemistry than similar interactions with heavier group 11 or post transition metal atoms[29,30,81] While the sheer number of structures can be intimidating, the key interactions can be broken down into combinations of either η^2 (C,O) or oxalate binding motifs. As was the case for clusters with heavier first row transition metals,[31,79,80] the predominant core ion structure is the butterfly motif, featuring two η^2 (C,O) bound CO_2 ligands especially at cluster sizes less that $n = 4$. For $[Fe(CO_2)_n]^-$ clusters the butterfly structure is expanded to accept a third η^2 (C,O) bound CO_2 ligand; this results in a complex with C_{3v} symmetry that is unique to

the Fe-CO_2 cluster anion. The second most common ligand seen in first row transition metal clusters with CO_2 (and more generally in other metal-CO_2 anionic systems) is the C_2O_4 motif especially at larger cluster sizes. In many cases, the C_2O_4 ligand is paired with an η^2 (C,O) bound CO_2 ligand generating a characteristic vibrational signature seen in the spectra of $[M(CO_2)_n]^-$ (where $n \geq 4$) clusters. For $[Mn(CO_2)_n]^-$ clusters the C_2O_4 ligand is observed to be paired with a second oxalate ligand.

Chapter 6

Enhancement of the Intensity of the Symmetric CO_2 Stretching Transition in MCO_2^- Complexes (M = H, Ag, and Bi) Compared to CO_2^-

This chapter has been adapted with permission from the following previously published article:

Thompson, M. C. and Weber, J. M., "Enhancement of Infrared Activity by Moving Electrons through Bonds – The Case of CO_2 anion and Carboxylate." Chemical Physics Letters. 2017 683: p. 586-590. DOI: 10.1016/j.cplett.2017.01.060. Copyright Elsevier.

6.1 Introduction

One of the most basic measurements in spectroscopy is the intensity of a vibrational transition. Within this value are encoded many molecular properties, the most important of which is how the charge distribution of the species varies with structural changes during vibration. This principle is enshrined in the selection rule for infrared activity, $\left(\frac{\partial \vec{\mu}(Q)}{\partial Q}\right)_0 \neq 0.$

The driver of infrared intensity is the vibrational transition dipole moment $\langle v'|\vec{\mu}(Q)|v''\rangle$ coupling vibrational levels $|v'\rangle$ and $|v''\rangle$ of a normal mode Q. This is often understood with a fixed charge approximation, which assumes that the atomic charges are constant over motion along the normal mode coordinate. This approximation, however, does not hold true in all situations; in some cases, the intensity of a particular infrared transition defies what can be reasonably expected based on the fixed charge approximation. One prominent example is seen in the intensity ratio of the symmetric and asymmetric CH_2 stretching motion in CH_2X radicals (X = F, Cl) as measured by

Nesbitt and coworkers.[108,109] They found that the CH stretching motion was strongly coupled to the charge distribution of the radical species. The flow of charge along the normal mode coordinates runs counter to the direction of the transition dipole moment approximated with the fixed charge model. This reduces the magnitude and even reverses the direction of the overall transition dipole moment. Nesbitt and coworkers found that the intensity of the symmetric CH_2 stretching motion was enhanced by "charge sloshing" along the mode, while the asymmetric CH_2 stretching motion is suppressed by the same effect.[108,109] This results in a reversal of the expected ratio of the intensities of these two modes compared to what is expected based on a fixed charge model.

While the term charge sloshing certainly evokes the correct picture of the physical process occurring, for the remainder of this chapter this process of vibrationally mediated electron density modulation will be referred to as charge oscillation. Charge oscillation has been observed in several ionic systems.[110-112] In this chapter, charge oscillation in several $MCOO^-$ species (M = H, Ag, and Bi) with be contrasted with the photodissociation spectrum of solvated CO_2^-.

6.2 Theoretical Methods

Many of the calculations were performed with the same procedure as described in Chapter 2. Briefly, calculations were performed using density function theory as implemented in the TURBOMOLE suite.[55] Calculations were done with a dispersion corrected B3LYP functional[56] with def2-TZVPP basis set[58] with effective core potentials for the Bi atom.[113] In order to characterize how the charge distribution of a species changes along the symmetric CO_2 stretching coordinate, geometries along the symmetric and asymmetric CO_2 stretching coordinates were generated by distorting the molecular geometries along each coordinate using the VIBRATION program. A single point calculation was performed for each geometry, and the charge of each atom

was assigned using several methods. Charge analysis using Mulliken, Loewdin, Natural Population Analysis, and population analysis based on orbital occupation numbers with multicenter correction (PABOON[114]) were compared, and the PABOON method was found to yield the best agreement with the overall dipole moment calculated obtained by density functional theory. The charges on the COO^- moieties were calculated by adding the charges on the carbon and both oxygen atoms.

6.3 Results and Discussion

We set out to compare and contrast the infrared intensity of symmetric and asymmetric CO_2 stretching modes in CO_2^- and several $MCOO^-$ species (M = H, Ag, Bi). In each of the $MCOO^-$ species, a single σ bond forms between the M atom and the carbon atom of the COO^- group. In the case of both CO_2^- and $MCOO^-$, the excess electron density is accommodated in what would be an antibonding orbital of neutral CO_2 (See Chapter 1). Structures and highest occupied molecular orbitals of CO_2^- and $MCOO^-$ are shown in Figure 6.1.
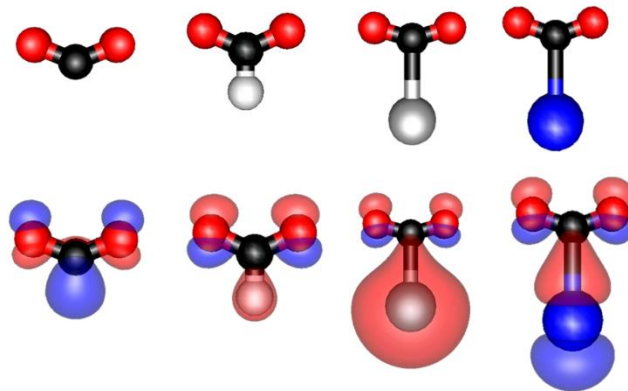
Figure 6.1. Structures and HOMOs for CO_2^-, $HCOO^-$, $AgCOO^-$, and $BiCOO^-$ (presented left to right in the order listed). Carbon atoms are shown in black, oxygen atoms are shown in red, hydrogen in white, silver in grey, and bismuth in blue.

Unlike the other species discussed here, CO_2^- is unstable with respect to electron autodetachment. The species can be stabilized in a matrix[18] or a $(CO_2)_n^-$ cluster.[21,23,24] We performed photodissociation spectroscopy on $(CO_2)_8^-$, which has been confirmed to have CO_2^- as the core ion by Johnson and coworkers, and can therefore be characterized as having the composition $CO_2^- \cdot (CO_2)_7$.[23] The MCOO$^-$ species studied (M = Ag, Bi) each form metalloformate type complexes (see Chapter 3 for an in depth discussion of the BiCOO$^-$ core ion). We report the photodissociation action spectra of HCOO$^-\cdot$Ar, $CO_2^- \cdot (CO_2)_7$, BiCOO$^- \cdot (CO_2)_3$, and AgCOO$^- \cdot (CO_2)_4$ in Figure 6.2.
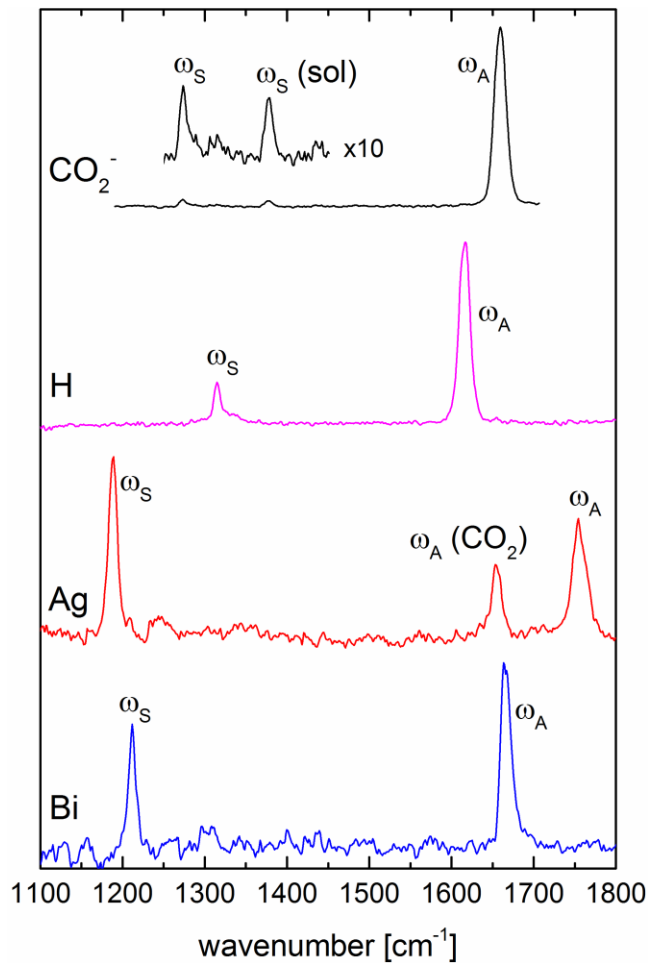
Figure 6.2. Photodissociation spectra of $CO_2^-\cdot(CO_2)_7$ (top, black), $HCOO^-\cdot Ar$ (second trace, magenta), $AgCOO^-\cdot(CO_2)_4$ (third trace, red), and $BiCOO^-\cdot(CO_2)_3$ (bottom trace, blue). Transitions are identified as symmetric (ω_S) or asymmetric C–O stretching motions (ω_A). Assignments of the spectra are discussed below.

The spectrum of $CO_2^-\cdot(CO_2)_7$ was collected by monitoring the formation of $CO_2^-\cdot(CO_2)_6$ resulting from the loss of a single CO_2 molecule. The spectrum is dominated by the high intensity feature at 1661 cm^{-1}, which is assigned to the asymmetric C–O stretching mode of CO_2^- (ω_A). This value is in good agreement with matrix isolation measurements perfomed by Jacox and coworkers.[18] The two lower intensity features are each due to symmetric C–O stretching motions of the core ion (1274 cm^{-1}, ω_S) and of the solvent molecules (1379 cm^{-1}). The interaction of solvent

CO_2 molecules with the core ion slightly breaks their symmetry, which allows for this weak transition to be observable.

The photodissociation spectrum of $HCOO^-\cdot Ar$ is collected by monitoring the formation of $HCOO^-$ as a result of the loss of the Ar atom. This spectrum does not feature the same suppression of low energy transitions described in previous chapters of this thesis. The binding energy of an Ar atom to a negatively charged molecule is approximately 500 cm^{-1}, which means that a single infrared photon in the energy range of the experiment will readily cause the evaporation of the Ar atom on the timescale of the experiment. The spectrum has two spectral signatures at 1617 and 1314 cm^{-1}. These transitions are assigned to ω_A and ω_S, respectively. These values are consistent with photodissociation work performed by Johnson and coworkers.[115] The presence of the hydrogen atom results in a significant red shift of ω_A compared to the value for CO_2^- accompanied by a blue shift of ω_S. There is also a decrease in the calculated OCO bond angle from 135° (CO_2^-) to 131° ($HCOO^-$). As described in Chapter 3, the spectral shifts of ω_A and ω_S can be traced to a weakening of the kinetic coupling of the individual CO oscillators as the OCO bond angle decreases. Unlike in the behavior described in $[Bi(CO_2)_n]^-$, this effect is combined with an decreasing amount of charge on the COO^- group compared to CO_2^-. A decreasing amount of charge would result in a strengthening of the C-O bonds and a blue shift of both CO_2 stretching frequencies. This highlights the strong effect that the more acute bond angle has on the stretching frequencies of $HCOO^-$.

The spectrum of $AgCOO^-\cdot(CO_2)_4$ was collected by monitoring the formation of $AgCOO^-\cdot(CO_2)_3$ as a result of the loss of a single CO_2 molecule. We assign the experimental features at 1756 and 1187 cm^{-1} to ω_A and ω_S of the $AgCOO^-$ core ion, respectively. The feature at 1667 cm^{-1} is assigned to ω_A of a CO_2^- core ion. These values are consistent with observations by Weber and

coworkers.[30] The Ag atom is solvating the CO_2^- core ion and the loss of Ag as a result of vibrational excitation can be monitored. The presence of the Ag atom shifts the position of ω_A to slightly higher wavenumber compared to the value for $CO_2^- \cdot (CO_2)_7$. For more information about this system the author directs the reader to the following article.[30] The spectrum of $BiCOO^- \cdot (CO_2)_3$ has two spectral features that can be assigned to ω_A (1663 cm^{-1}) and ω_S (1211 cm^{-1}). For more information about this system, please see Chapter 3.

Of interest is the change in the intensity ration of ω_S and ω_A (I_S/I_A) for the systems under study. Consistently for all $MCOO^-$ species discussed, the intensity ratio I_S/I_A is enhanced compared to the intensity ratio of the same transitions in CO_2^-. In the case of $BiCOO^-$, this ratio is enhanced by a factor of 40. An even greater enhancement of a factor of 50 is observed experimentally `for $AgCOO^-$. The suppression of low-energy transitions described in previous chapters will result in a slight reduction of the intensity of ω_S, meaning that the experimentally observed enhancement may prove to be smaller than the actual change of this ratio for infrared absorption.

In the typical description of electric dipole allowed vibrational transitions, the transition dipole moment of a transition between two vibrational states $\left| v' \right\rangle$ and $\left| v'' \right\rangle$ can be written as $\left. \frac{\partial \vec{\mu}(Q)}{\partial Q} \right|_0 \langle v' | Q | v'' \rangle$. Taking the derivative of the dipole moment operator, $\vec{\mu}(Q) = \sum_j (q_j \cdot \vec{r}_j)$, we arrive at the equation,

$$\left. \frac{\partial \vec{\mu}(Q)}{\partial Q} \right|_0 = \sum_j \left(q_j \left. \frac{\partial \vec{r}_j}{\partial Q} \right|_0 + \vec{r}_j \left. \frac{\partial q_j}{\partial Q} \right|_0 \right). \tag{6.1}$$

The first term in equation 6.1 describes the derivative of the dipole moment under the fixed charge approximation. In this approximation, the atomic charges, q_j, are held constant while the nuclear coordinates change along the normal mode. The second term quantifies the derivative of the dipole

moment due to only the changes in the charge distribution along the normal mode coordinate, while the nuclear coordinates themselves remain fixed. The sum of both of these components will enter into the expression for the overall transition dipole moment.

The large differences in the intensity ratio I_S/I_A for the different ions cannot be explained with the fixed charge approximation (Table 6.1). Using equation 6.1, we can separate the contributions of the fixed charge approximation and charge oscillation. The charge oscillation term can be calculated by varying the atomic charges of each atom, while maintaining the equilibrium geometry, in center of mass coordinates, of the complex as a whole. Since all of the molecules in question have C_{2v} symmetry, only the component of the transition dipole moment along the σ bond in $MCOO^-$ species will contribute to the overall transition dipole for the symmetric stretch. For the asymmetric stretch, the overall transition dipole lies perpendicular to the axis, in the plane of the molecule.

Table 6.1. A summary of the calculated M–C bond distances, charge on the COO groups, the intensities of ω_S and ω_A (I_S and I_A) and the calculated and experimental ratio (I_S/I_A). The ratio labeled DFT refers to the calculated infrared intensities from the calculated vibrational spectrum of each complex.

Species	M-C distance [116]	Charge on COO [e]	I_S [km·mol^{-1}] (DFT)	I_A [km·mol^{-1}] (DFT)	I_S/I_A (DFT)	I_S/I_A (fixed-charge)	I_S/I_A (charge oscillation)	I_S/I_A (experimental)
CO_2^-	N/A	-1.00	21	642	0.033	0.45	0.004	0.021
$HCOO^-$	1.14	-0.90	146	671	0.22	0.57	0.11	0.22
$AgCOO^-$	1.51	-0.37	592	342	1.7	0.12	0.42	1.4
$BiCOO^-$	2.46	-0.53	851	569	1.5	0.30	0.71	0.65

The ratio I_S/I_A was calculated for both the fixed charge approximation and the charge oscillation approximation, and compared to the calculated ratios based on the predicted vibrational spectra from DFT calculations and the experimentally observed ratios. In general, the fixed charge approximation overestimates the experimentally observed intensity ratio for CO_2^- and $HCOO^-$ while underestimating the experimentally observed ratio for $BiCOO^-$ and $AgCOO^-$. In contrast, the ratio calculated only considering charge oscillation underestimates the experimentally observed ratio for CO_2^- and $HCOO^-$, but overestimates the ratio for $BiCOO^-$ and $AgCOO^-$ (Table 6.1). This can be understood by considering just how much charge does oscillate along the symmetric stretching coordinate in these systems. Figure 6.3 shows the portion of charge assigned to the COO group as a function of the position along the normal mode coordinate Q. This description is of course only meaningful for $MCOO^-$, since CO_2^- does not exhibit any charge movement along this coordinate, because there is no bonding partner in which to move the charge.
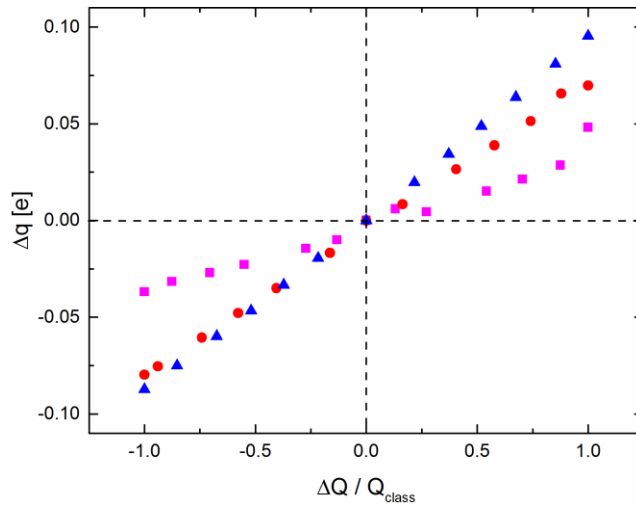
Figure 6.3. Combined plot of the change in charge of the COO group, Δq, plotted along the symmetric C–O stretching coordinate. The change in charge of $HCOO^-$ is shown in magenta squares, $AgCOO^-$ shown in red circles, and $BiCOO^-$ shown in blue triangles. The classical turning points along the normal mode coordinate are at ± 1, and the equilibrium geometry is shown at 0.

The metalloformate complexes exhibit a much higher proportion of the excess charge moving through the complex compared to the formate anion ($HCOO^-$). We can understand this by considering that the COO group in formate anion has about -0.9 e of charge assigned to it in the equilibrium geometry. This results in an upper limit of the amount of charge flow into the COO moiety since most of the charge already resides on the COO group. Charge flow from the H atom to the COO group accounts for approximately 0.1 e of charge. Conversely, the metalloformate species have between -0.5 e and -0.7 e on the COO group in their equilibrium geometry, which naturally allows for the binding partner to be able to push more charge into the COO groups. Charge flow for these species amounts to approximately 0.2 e of charge moving between the M atom and the COO group.

It is clear that the binding partner M acts as a charge reservoir, allowing for excess charge to be moved into and out of the bonding partner along the symmetric stretching coordinate. During CO elongation charge moves out of the binding partner M and into the COO group, while during CO contraction charge migrates out of the COO group and into the binding partner M. The identity of the binding partner is a key role in the amount of charge that is moved during this process.

We note that the intensity of the asymmetric stretching infrared signature is also enhanced by charge oscillation. In this case, charge oscillation occurs from one C−O bond into the other as each bond is contracted and extended, respectively. The magnitude of this enhancement is not connected to the identity of the binding partner M, since the charge oscillation is limited only to the COO^- group.

6.4 Conclusions

The intensity ratios I_S/I_A for $MCOO^-$ complexes (M = H, Ag, Bi) are not recovered using the fixed charge model, which can often be used successfully for calculating the transition dipole moment. The reason for the failure of this model is that a significant amount of charge moves between the M atom and the COO group along the symmetric CO_2 stretching coordinate. Comparison of the intensity ratio I_S/I_A in $MCOO^-$ to the same ratio in CO_2^- shows enhancement of over 50 times the value for CO_2^-. We find that the intensities of both the symmetric and the asymmetric C–O stretching mode are enhanced by charge oscillation along the normal mode coordinate, although the enhancement of the intensity of the symmetric stretching mode shows a greater dependence on the binding partner, M, compared to the asymmetric stretching mode.

Chapter 7

Core Ion Geometries in $(N_2O)_nO^-$ and $(N_2O)_n^-$

This work has been adapted with permission from the following previously published article:

7.1 Introduction

Since its detection by mass spectroscopy in the 1960's, the molecular properties of the N_2O^- anion have largely remained elusive.[14,117-121] The lack of experimental values of many of the properties of this molecular anion lie in the fact that it is very difficult to produce. Early collision experiments to determine the adiabatic electron affinity (AEA) of this species yielded wildly different results (not even agreeing on the sign of the AEA).[122,123]

Nitrous oxide is isoelectronic with CO_2. Like CO_2, N_2O adopts a bent geometry upon accepting an electron. The Walsh diagram of N_2O (Figure 7.1), calculated based on a method discussed in section 7.2, shows that an excess electron will occupy one of the empty 3π orbitals of N_2O. This orbital is stabilized by bending the NNO bond angle away from the linear neutral geometry to approximately 135˚. High-level *ab initio* calculations[124,125] predict a negative AEA for N_2O, which would mean that the anion is unstable against electron autodetachment. This would explain the difficulties in the generation of the N_2O^- anion. This change in geometry results in very

small Frank-Condon overlap between anionic and neutral states, rendering the ground state of the

neutral inaccessible from the ground state of the anion.
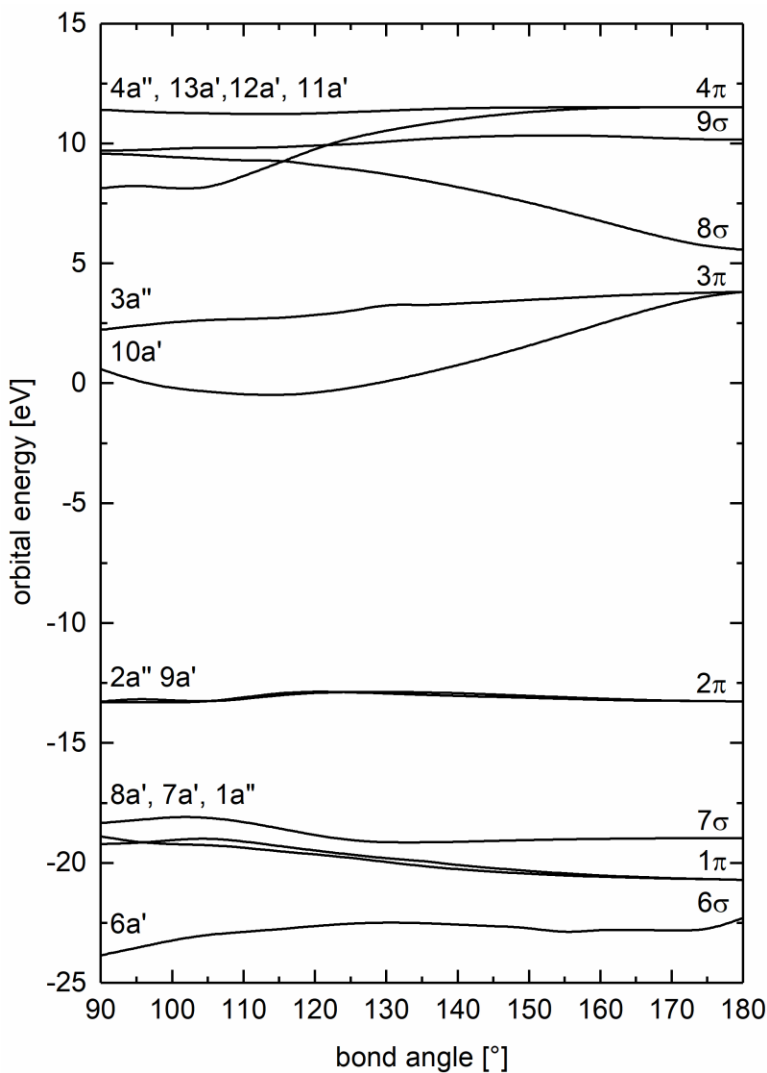
Figure 7.1. Walsh diagram of N_2O, showing molecular orbital (MO) energies as a function of NNO angle. The Walsh diagram for N_2O was calculated using the RI-MP2 method (second-order Møller-Plesset perturbation theory applying the resolution-of-identity for evaluation of two electron integrals)[126,127] with def2-TZVPP basis sets for all atoms.[58] Labels for MO curves in linear and bent geometries are shown above the respective curve. In cases where more than one curve is shown, the labels are listed with decreasing energy. The LUMO of neutral N_2O is the 3π orbital.

Another difficulty in generating N_2O^- comes from the fact that direct electron attachment to N_2O results only in dissociation, with products primarily being O^- and N_2.[14,120,128-130] The ground state geometry of N_2O^- is predicted to lie very close in energy to a dissociative curve.[121,124,125,131] It is theorized that the formation of bare N_2O^- is likely the result of low energy charge transfer processes occurring with other anionic species (NO^- or O^-).[117] Unlike CO_2^-, the anion of N_2O has not been isolated in a matrix, and consequently the vibrational frequencies of this species have not been experimentally measured.

Previous work looking at electron attachment to neutral $(N_2O)_n$ clusters has found that the main product channel is a dissociative attachment to N_2O resulting in the formation of $(N_2O)_{n-1}O^-$ clusters. Additionally it was reported that smaller abundances of $(N_2O)_n^-$ and $(N_2O)_nNO^-$ clusters can be produced at low electron kinetic energies.[14,130,132-138] These anionic clusters have primarily been studied using photoelectron spectroscopy. Johnson and coworkers were able to characterize different isomers of $N_2O_2^-$ using photoelectron spectroscopy by introducing different precursor species into their experiment.[139] Sanov and coworkers collected photoelectron spectra of $(N_2O)_nO^-$ cluster ions.[71,140,141] They report that for small clusters the core ion is a molecular anion with formula $N_2O_2^-$, and between cluster size $n = 3$ and 4 there is a change in the photoelectron signature from a molecular anion to an atomic anion. This most likely is due to a core ion change from an $N_2O_2^-$ to an O^- anion. As discussed earlier in Chapter 3, such core ion switching events can be due to a balance between electronic stability and solvation energy.

Despite the wealth of experimental work on $(N_2O)_nO^-$ clusters, there has been no infrared work to determine the exact nature of the charge carrier. In the case of $(N_2O)_n^-$ there has been no work characterizing the nature of the core ion. In this chapter, the infrared photodissociation

spectra of $(N_2O)_nO^-$ and $(N_2O)_n^-$ are reported and the nature of the core ion in both cluster systems is discussed.

7.2 Results and Discussion of $(N_2O)_nO^-$ Clusters

Electron bombardment of a supersonic expansion of N_2O (See Chapter 2) resulted in the formation of $(N_2O)_nO^-$, $(N_2O)_n^-$, and $(N_2O)_nNO^-$ clusters (Figure 7.2). The most abundant species were $(N_2O)_nO^-$ clusters, which is consistent with previous work studying the electron attachment to neutral N_2O clusters.[14,130,132-138]
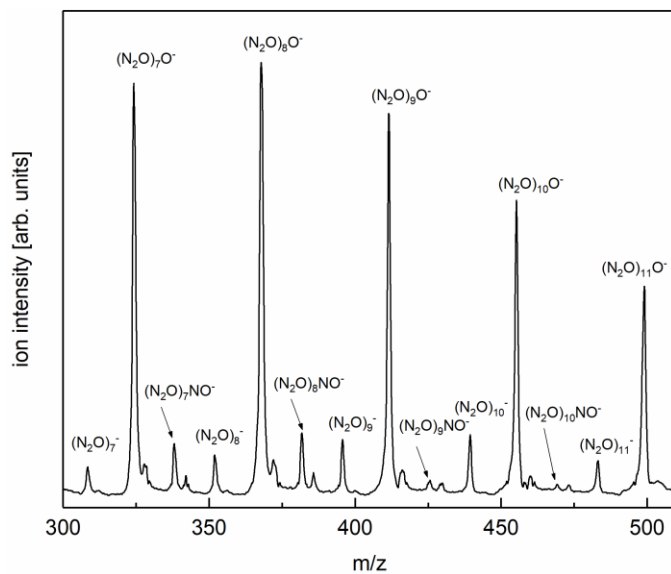
Figure 7.2. Mass spectrum of ions generated by electron injection into a supersonic expansion of neat N_2O.

The infrared photodissociation spectra of $(N_2O)_nO^-$ are shown in Figure 7.3. For smaller ions (n $\leq$ 5) the spectra were obtained by monitoring the loss of both Ar tags from $(N_2O)_nO^- \cdot 2Ar$. All other spectra were obtained by monitoring the loss of N_2O from $(N_2O)_nO^-$. We note the spectrum for n = 5 was obtained with and without the presence of Ar tags and there was no significant difference in either peak position or relative intensities (Figure 7.4).
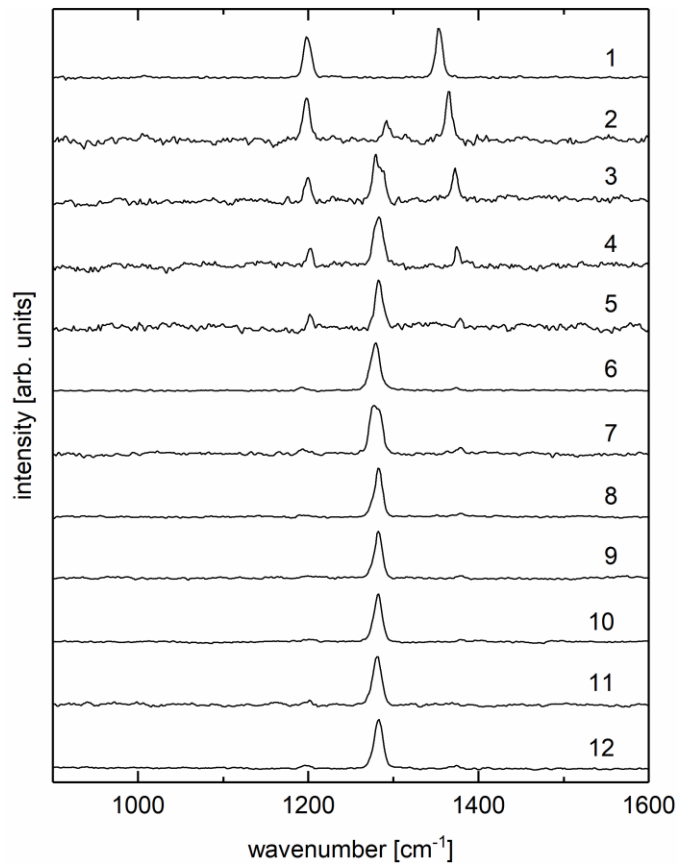
Figure 7.3. Infrared photodissociation spectra of $(N_2O)_nO^-$ ($n = 1–12$). The numbers on the side indicate the number of N_2O in the cluster.
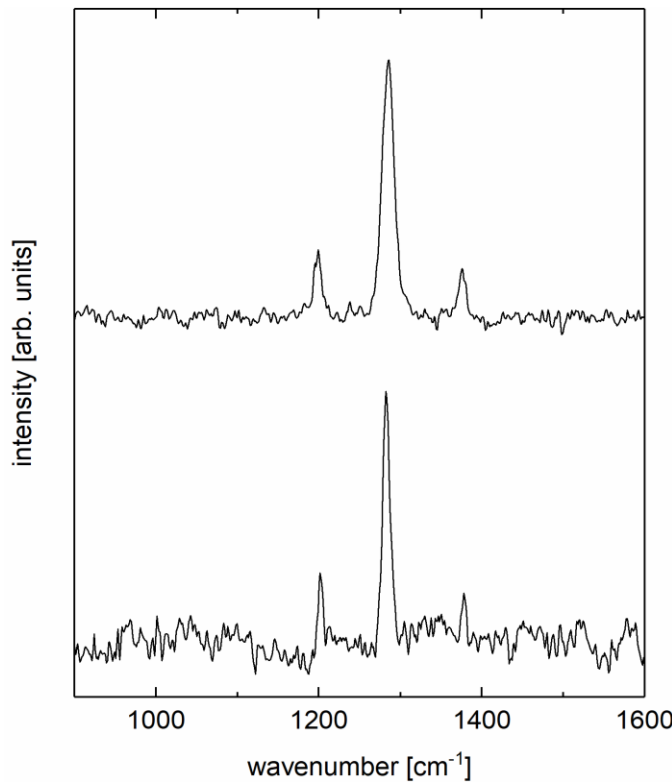
Figure 7.4. Comparison of the experimental spectra of $(N_2O)_5O^-$ (top) and $(N_2O)_5O^- \cdot Ar_2$ (bottom).

The experimental spectrum of $(N_2O)O^- \cdot Ar_2$ contains two features at 1197 and 1352 cm^{-1}. This indicates the presence of a molecular core ion, since O^- does not have any vibrational frequencies. Also, if O^- were to be the core ion, we would expect to see the N-O stretching motion of a solvent N_2O species around 1285 cm^{-1}. With the signature not being present, we conclude the core ion must be a molecular ion with formula $N_2O_2^-$. This observation is consistent with previous work by Sanov and coworkers who observed molecular photoelectron signatures from $N_2O_2^-$.[71] Quantum chemical calculations reveal three different isomers of the $N_2O_2^-$ (Figure 7.5). Two of the isomers are cis and trans configurations of $ONNO^-$ with the cis isomer lying 116 meV higher in energy than the global minimum trans configuration. A third isomer, which lies 291 meV above

the global minimum trans configuration, is an NNO_2^- configuration where the central nitrogen bonds to a second oxygen atom. This structure was found to be the predominant core ion structure in $(N_2O)_nO^-$ generated by electron injection into a supersonic expansion of N_2O studied by Johnson and coworkers using photoelectron spectroscopy.[139]

trans-ONNO⁻   cis-ONNO⁻ NNO_2^-
E=0 meV   E=116 meV   E=291 meV
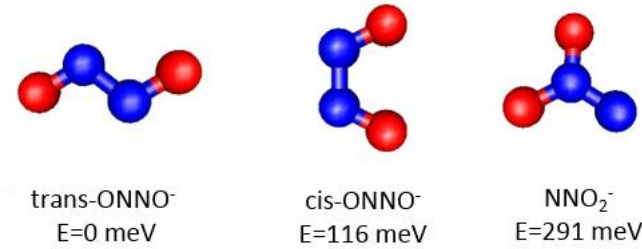
Figure 7.5. Calculated isomers of $N_2O_2^-$. Calculations were performed as described in Chapter 2.

Comparison of the calculated vibrational frequencies of these three isomers with the experimental spectrum reveal that the core ion is the NNO_2^- isomer (Figure 7.6). We assign the experimental signature at 1352 cm⁻¹ to the N–N stretching motion and the lower energy signature to the asymmetric NO_2 stretching mode. The narrow spectral width of the two signatures and the absence of any lower intensity features preclude the presence of any other isomer. It is interesting to note that the highest energy isomer is the only one that is populated. We believe that this geometry can be explained by understanding the charge distribution of neutral N_2O. Charge analysis assigns a charge of +0.51 e on the central N atom, while the terminal N atom has a small negative charge (–0.07 e) and the O atom has a charge of –0.44 e. We concur with the argument made by Johnson and coworkers, that an O^- ion, most likely generated as a result of dissociative electron attachment to neutral N_2O, performs a nucleophilic attack at the central nitrogen of a neutral N_2O species to form NNO_2^-.[139]
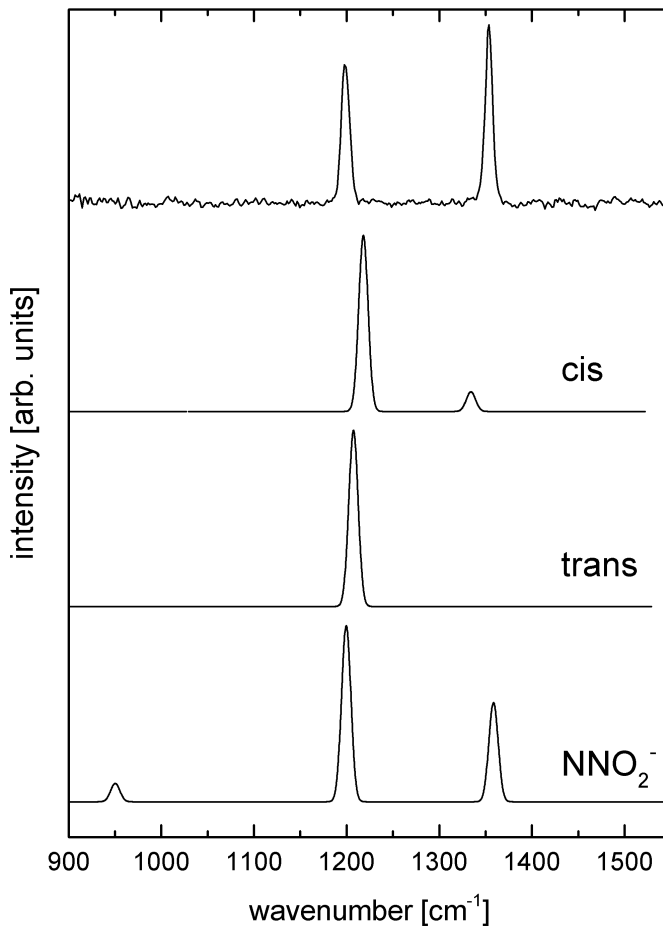
Figure 7.6. Comparison of the experimental spectrum of $N_2O_2^- \cdot 2Ar$ (top trace) with simulated spectra of different isomers of $N_2O_2^-$ (bottom three traces).

Larger cluster sizes show the presence of a new feature at 1292 cm^{-1} that red shifts with increasing cluster size and reaches a stable position at 1282 cm^{-1} in the limit of the largest cluster sizes under study. We assign this band to the N–O stretching motion of neutral N_2O molecules solvating the core ion. For smaller cluster sizes, this feature has some substructure that is likely due to small differences in the solvation position of the solvent around the core ion. The intensity of the solvent signature increases compared to the signatures of the NNO_2^- ion with increasing cluster size. This is to be expected since the number of solvent species increases with cluster size.

Sanov and coworkers observed a core ion switch from NNO_2^- to O^- at cluster size n=4. Inspection of the spectra for larger cluster sizes shows that no new spectral features appear with increasing cluster size. This suggests that if a core ion switch were to occur it would be to a core ion geometry without observable vibrational signatures. The most likely scenario would be a core ion change from NNO_2^- to O^-. In the present experiment, signatures of the NNO_2^- persist for all cluster sizes studied, suggesting that the core ion change remains incomplete with our source conditions. We note, however, that if a core ion change were to occur, there would be a disproportional change in the ratios of the peak areas of NNO_2^- vibrational signatures to the peak areas of the solvent signature. We analyzed the integrated peak areas of signatures up to $(N_2O)_7O^-$. If there is no core ion change, then the ratio of NNO_2^- vibrational signatures to the solvent signatures would change according to

$$\frac{I_{NNO_2}}{I_{solv}} \propto \frac{1}{n-1} \qquad (n \geq 2), \qquad\qquad (7.1)$$

with the onset of solvent signatures beginning at n = 2. Since our infrared spectra do not support the presence of either cis or trans $ONNO^-$, we assume that the only molecular core ion species present is NNO_2^-. This is in line with work by Sanov and coworkers who only observed a single molecular signature in their photoelectron images.[71] The assumption that we only have an NNO_2^- or an O^- molecular core ion allows us to directly compare our experimental results to the model discussed above (see Figure 7.7).
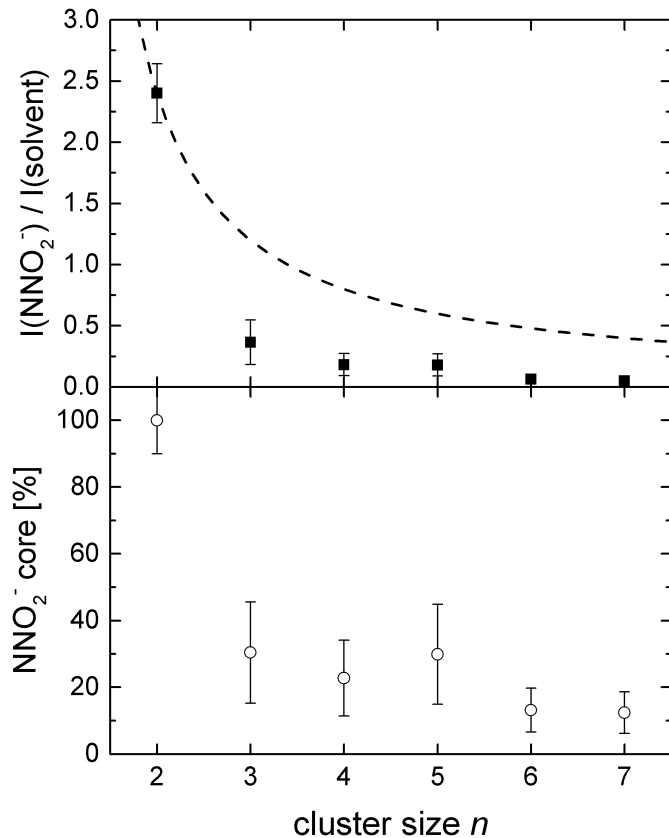
Figure 7.7. Top panel: ratio of integrated peak areas (square points) compared with the predicted values from the model explained in the text (dashed line). Error bars are 10% of the first data point and 50% for all subsequent data points. Bottom panel: percentage of clusters with a NNO_2^- core ion according to the model. The model assumes 100% NNO_2^- core ion population for $n = 1$.

Clusters with NNO_2^- core ion geometries drop to around 30% of the overall population by n = 3 and then drop to around 15% around n = 6. This is in conflict with behavior observed by Sanov and coworkers where the core ion change occurred abruptly at n = 4. We believe that different source conditions between the two experiments are responsible for this discrepancy.

In conclusion, the core ion geometry for small $(N_2O)_nO^-$ clusters is the NNO_2^- molecular anion. For larger cluster ions there is a core ion change to a species that does not have any detectable vibrational signatures (presumably O^-). These clusters were generated by electron

injection into a supersonic expansion of neat N_2O. Previous work by Johnson and coworkers has shown that the geometry of the core ion is somewhat dependent on the method used to create the ions.[139] As such, the currently reported results may only be applicable to clusters generated in a similar manner with the same precursor gases.[71,139-141]

7.3 Core ion structure determination of $(N_2O)_n^-$

The photodissociation action spectra of $(N_2O)_n^-$ ($n = 7–11$, 14,15) are shown in Figure 7.8. The spectra were generated by monitoring the loss of a single N_2O species. No other loss channels were observed resulting from the infrared absorption. The main spectral feature is a high intensity band at 1282 cm^{-1}, which corresponds to the N–O stretching mode of neutral N_2O species in the cluster. These N_2O species are acting as solvent species, solvating the core ion in the cluster. The other signatures in the experimental spectra lie in regions where neutral N_2O does not have a vibrational feature. We conclude that these signatures must be due to vibrations of a molecular core ion. At the smallest cluster size examined ($n =7$), there is a low intensity feature at 1643 cm^{-1}. At $n = 8$ there are two spectral features in this region one at 1665 and another at 1583 cm^{-1}. For clusters larger than $n = 9$, there is only one low intensity spectral feature in this region, its position varying from 1592–1598 cm^{-1} as cluster size increases.
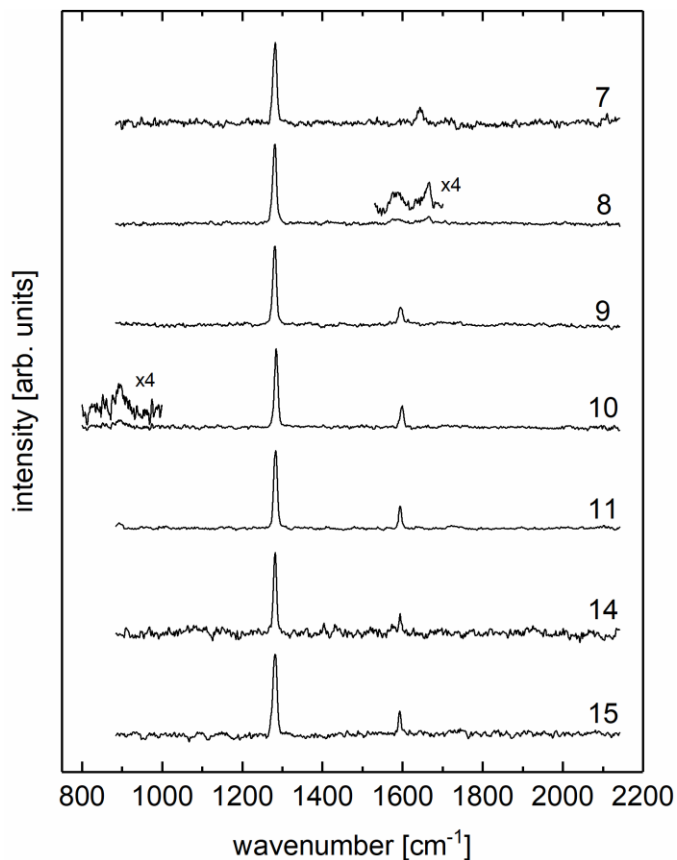
Figure 7.8. Photodissociation spectra of $(N_2O)_n^-$ cluster ions (n = 7-11,14,15).

The presence of only one unknown vibrational signature in the region from 1400–2000 cm^{-1} suggests that the core ion is a single N_2O^- species. If the excess electron were to be shared between multiple N_2O species, one would expect to see many different signatures in this region, corresponding to local N–N or N–O oscillations of the core ion. The signature at 1595 cm^{-1} can be assigned to the N–N stretching mode of an N_2O^- core ion. This assignment is confirmed by both density functional theory and *ab initio* calculations (see Table 7.1). Anharmonic correction scaling factors for N_2O^- were calculated by comparing calculated vibrational frequencies to experimentally measured frequencies. Using an anharmonic correction scaling factor of 0.949, our

calculated vibrational frequency for the N–N stretching mode in N_2O^- is exactly 1595 cm^{-1}. This confirms the assignment of this mode to the N–N stretch, although the exact agreement is likely fortuitous.

TABLE 7.1. Experimental transitions and calculated (harmonic approximation) (in cm^{-1}) for neutral and anionic N_2O. Experimental data for neutral N_2O have been taken from Ref. [27] Experimental data for N_2O^- are from the present work.

mode	method	N_2O	N_2O^-
bend	experimental	589	N/A
	calc. (this work, DFT)	619	654
	calc. (Ref. [142])	549	560
	calc. (Ref. [143]).	N/A	657
N-O stretch	experimental	1285	894
	calc. (this work, DFT)	1329	993
	calc. (Ref. [142])	959	863
	calc. (Ref. [143])	N/A	998
N-N stretch	experimental	2224	1595
	calc. (this work, DFT)	2343	1681
	calc. (Ref. [142])	2434	1610
	calc. (Ref. [143])	N/A	1684

As mentioned above, the exact position of the N–N stretching mode depends on the size of the cluster, with two different signatures separated by around 80 cm^{-1}. It is not unreasonable to

suggest that this could be due to the N_2O^- experiencing two different solvation environments. In the limit of a small cluster, solvation will occur preferentially at the portion of the core ion containing more charge. Preferential solvation around the oxygen side of the anion will result in charge polarization of the excess electron toward that side of the molecule. This will result in a stronger attraction of additional solvent species to this side of the anion. As the cluster grows, eventually there will be no more solvation sites on this side of the anion and solvation will occur on the other side. As the solvation shell around the anion begins to grow, the charge will redistribute more evenly.

When N_2O accepts an excess electron, it is accommodated in an antibonding orbital. This weakens the N-N and N-O bonds and results in a red shift of both stretching frequencies. When the charge distribution shifts toward the N–N bond this will weaken it resulting in a red shift of the signature. This is similar to the behavior observed in the transition from cluster size n = 7–9. At these cluster sizes the N–N stretching signature red shifts over 80 cm^{-1} from 1665 cm^{-1} for small clusters to 1595 cm^{-1} for larger clusters. One hypothesis consistent with this shift is that a half shell is formed around the oxygen atom of the N_2O^-, which is completed at $n = 8$. The solvation shell then continues to grow to a more symmetric structure around the core ion at larger cluster sizes. The behavior is similar to $IBr^- \cdot (CO_2)_n$ clusters, where solvation preferentially occurs at the bromine atom of the core ion until a half shell is formed at $n \approx 8$.[144] Electronic structure calculations of clusters at this size are difficult, and due to the large number of possible structures, we were unable to confirm half shell formation at large cluster sizes by computational chemistry. We were able to calculate the energy difference between an O solvated cluster and a more symmetric solvation environment for cluster sizes $n = 3$ and 4. At these cluster sizes, asymmetric solvation structures around the O atom of the core ion are 50-60 meV lower in energy than structures

symmetrically solvating the core ion. This result is consistent with our present hypothesis. However, there was only a negligible difference in the calculated vibrational frequency of the N–N stretching mode (less than 10 cm^{-1}). While the predicted red shift of the experimentally observed signature is consistent with our calculations, the magnitude of the shift is not recovered. Nevertheless, the overall theory that the experimentally observed red shift is due to the formation of a half shell around the core ion is still a plausible explanation.

In principle, the N–O stretching motion of N_2O^-, predicted to be between 863–998 cm^{-1} depending on the level of theory, is within the wavenumber range of our experiment. To attempt to observe this signature, we extended our scanning range to 800 cm^{-1} for $(N_2O)_{10}^-$ clusters, which was the most abundant cluster size, and detected a low intensity feature at 894 cm^{-1}. Transitions below around 1000 cm^{-1} are suppressed due to the binding energy of N_2O solvent molecules, leading to kinetic shift effects, as described in the previous chapters of this thesis. Calculations performed for the current experiment using an anharmonic correction factor of 0.967 predict the N–O stretching mode to be at 960 cm^{-1}. This does not agree well with the experimental observation, and likely is due to an underestimation of the anharmonicity of this vibrational mode.

7.4 Conclusions

We report the photodissociation spectra of $(N_2O)_nO^-$ and $(N_2O)_n^-$ generated by electron injection into a supersonic expansion of N_2O. In $(N_2O)_nO^-$, we identify the core ion for smaller cluster sizes as NNO_2^-. There is a core ion change that occurs around $n = 3$ to predominantly an O^- core ion, although the molecular core ion persists in small abundances.

For $(N_2O)_n^-$, the core ion is N_2O^-. IR measurement of the vibrational frequencies of this ion show the N–N stretching vibrational frequency to be 1595 cm^{-1} and the N–O vibrational

frequency to be 894 cm^{-1}. The observation of an abrupt red shift of the N–N stretching mode is attributed to the formation of a half solvation shell around the oxygen side of the core ion at cluster size $n = 8$.

Chapter 8

Bibliography

1.   *Climate Change 2013 - The Physical Science Basis*; Cambridge University Press, 2014.

2.   Barton Cole, E.; Bocarsly, A. B. In *Carbon Dioxide as Chemical Feedstock*; Wiley-VCH Verlag GmbH & Co. KGaA: 2010, p 291-316.

3.   Pan, W.; Song, C. In *Carbon Dioxide as Chemical Feedstock*; Wiley-VCH Verlag GmbH & Co. KGaA: 2010, p 249-266.

4.   Hori, Y. In *Modern Aspects of Electrochemistry*; Vayenas, C. G., White, R. E., Gamboa-Aldeco, M. E., Eds.; Springer New York: New York, NY, 2008, p 89-189.

5.   Rosen, B. A.; Salehi-Khojin, A.; Thorson, M. R.; Zhu, W.; Whipple, D. T.; Kenis, P. J. A.; Masel, R. I. Ionic liquid-mediated selective conversion of CO_2 to CO at low overpotentials. *Science* **2011**, *334*, 643-644.

6.   Lim, C.-H.; Holder, A. M.; Hynes, J. T.; Musgrave, C. B. Catalytic reduction of CO_2 by renewable organohydrides. *Phys. Chem. Lett.* **2015**, *6*, 5078-5092.

7.   Herzberg, G. *Molecular spectra and molecular structure*; Krieger Publishing Co.: Malabar, Florida, 1991; Vol. III.

8.   Sommerfeld, T.; Meyer, H.-D.; Cederbaum, L. S. Potential energy surface of the CO_2^- anion. *Phys. Chem. Chem. Phys.* **2004**, *6*, 42-45.

9.   Gutsev, G. L.; Bartlett, R. J.; Compton, R. N. Electron affinities of CO_2, OCS, and CS_2. *J. Chem. Phys.* **1998**, *108*, 6756-6762.

10.   Ovenall, D. W.; Whiffen, D. H. Electron spin resonance and structure of the CO_2^- radical ion. *Mol. Phys.* **1961**, *4*, 135-144.

11.   Walsh, A. D. 467. The electronic orbitals, shapes, and spectra of polyatomic molecules. Part II. Non-hydride AB_2 and BAC molecules. *J. Chem. Soc.* **1953**, 2266-2288.

12.   Weber, J. M. The interaction of negative charge with carbon dioxide – Insight into solvation, speciation and reductive activation from cluster studies. *Int. Rev. Phys. Chem.* **2014**, *33*, 489-519.

13.   Compton, R. N.; Reinhardt, P. W.; Cooper, C. D. Collisional ionization of Na, K, and Cs by CO_2, COS, and CS_2 - Molecular electron affinities. *J. Chem. Phys.* **1975**, *63*, 3821-3827.

14.   Knapp, M.; Echt, O.; Kreisle, D.; Märk, T. D.; Recknagel, E. Formation of long-lived CO_2^- ,N_2O^-, and their dimer anions, by electron-attachment to van-der-waals clusters. *Chem. Phys. Lett.* **1986**, *126*, 225-231.

15.   Raarup, M. K.; Andersen, H. H.; Andersen, T. Metastable state of CO_2^- with millisecond lifetime. *J. Phys. B.* **1999**, *32*, L659-L664.

16.   Schröder, D.; Schalley, C. A.; Harvey, J. N.; Schwarz, H. On the formation of the carbon dioxide anion radical CO_2^-. in the gas phase. *Int. J. Mass Spectrom.* **1999**, *187*, 25-35.

17.   Arnold, S. T.; Coe, J. V.; Eaton, J. G.; Freidhoff, C. B.; Kidder, L. H.; Lee, G. H.; Manaa, M. R.; McHugh, K. M.; Patel-Misra, D.; Sarkas, H. W.; Snodgrass, J. T.; Bowen, K. H. In *The Chemical Physics of Atomic and Molecular Clusters : Varenna on Lake Como, Villa Monastero, 28 June-7 July 1988*; Scoles, G., Ed.; Elsevier Science Publishing Company: New York, N.Y., U.S.A., 1990, p 467–490.

18.   Thompson, W. E.; Jacox, M. E. The vibrational spectra of CO_2^+, $(CO_2)_2^+$, CO_2^-, and $(CO_2)_2^-$ trapped in solid neon. *J. Chem. Phys.* **1999**, *111*, 4487-4496.

19.   Jacox, M. E.; Milligan, D. E. Vibrational spectrum of CO_2^- in an argon matrix. *Chem. Phys. Lett.* **1974**, *28*, 163-168.

20.   Zhou, M.; Andrews, L. Infrared spectra of the CO_2^- and $C_2O_4^-$ anions isolated in solid argon. *J. Chem. Phys.* **1999**, *110*, 2414-2422.

21.   Takahashi, K.; Sawamura, S.; Dimitrijevic, N. M.; Bartels, D. M.; Jonah, C. D. Transient negative species in supercritical carbon dioxide: Electronic spectra and reactions of CO_2 anion clusters. *J. Phys. Chem. A* **2002**, *106*, 108-114.

22.   Janik, I.; Tripathi, G. N. R. The nature of the CO_2^- radical anion in water. *J. Chem. Phys.* **2016**, *144*, 154307.

23.   Shin, J. W.; Hammer, N. I.; Johnson, M. A.; Schneider, H.; Glöss, A.; Weber, J. M. An infrared investigation of the $(CO_2)_n^-$ clusters: Core ion switching from both the ion and solvent perspectives. *J. Phys. Chem. A* **2005**, *109*, 3146-3152.

24.   Deluca, M. J.; Niu, B.; Johnson, M. A. Photoelectron-spectroscopy of $(CO_2)_n^-$ Clusters with 2≤n≤13: Cluster size dependence of the core molecular ion. *J. Chem. Phys.* **1988**, *88*, 5857-5863.

25.   Tsukuda, T.; Johnson, M. A.; Nagata, T. Photoelectron spectroscopy of $(CO_2)_n^-$ revisited: Core switching in the 2 £ n £ 16 range. *Chem. Phys. Lett.* **1997**, *268*, 429-433.

26.   Dodson, L. G.; Thompson, M. C.; Weber, J. M. Characterization of intermediate oxidation states in CO_2 activation. *Annu. Rev. Phys. Chem.* **2018**, *69*.

27.   Shimanouchi, T. *Tables of molecular vibrational frequencies consolidated volume I*; National Bureau of Standards, 1972.

28.   Weber, J. M.; Schneider, H. Infrared spectra of $X^-\cdot CO_2\cdot Ar$ cluster anions (X = Cl,Br,I). *J. Chem. Phys.* **2004**, *120*, 10056-10061.

29.   Knurr, B. J.; Weber, J. M. Solvent-driven reductive activation of carbon dioxide by gold anions. *J. Am. Chem. Soc.* **2012**, *134*, 18804-18808.

30.   Knurr, B. J.; Weber, J. M. Solvent-mediated reduction of carbon dioxide in anionic complexes with silver atoms. *J. Phys. Chem. A* **2013**, *117*, 10764-10771.

31.   Knurr, B. J.; Weber, J. M. Structural diversity of copper–CO_2 complexes: infrared spectra and structures of $[Cu(CO_2)_n]^-$ clusters. *J. Phys. Chem. A* **2014**, *118*, 10246-10251.

32.   Chen, Y.; Li, C. W.; Kanan, M. W. Aqueous CO_2 reduction at very low overpotential on oxide-derived Au nanoparticles. *J. Am. Chem. Soc.* **2012**, *134*, 19969-19972.

33.   Li, C. W.; Kanan, M. W. CO_2 reduction at low overpotential on Cu electrodes resulting from the reduction of thick Cu_2O films. *J. Am. Chem. Soc.* **2012**, *134*, 7231-7234.

34.   Costentin, C.; Robert, M.; Saveant, J.-M. Catalysis of the electrochemical reduction of carbon dioxide. *Chem. Rev. Soc.* **2013**, *42*, 2423-2436.

35.   Berardi, S.; Drouet, S.; Francas, L.; Gimbert-Surinach, C.; Guttentag, M.; Richmond, C.; Stoll, T.; Llobet, A. Molecular artificial photosynthesis. *Chem. Rev. Soc.* **2014**, *43*, 7501-7519.

36.   Schneider, J.; Jia, H.; Muckerman, J. T.; Fujita, E. Thermodynamics and kinetics of CO_2, CO, and H^+ binding to the metal centre of CO_2 reduction catalysts. *Chem. Rev. Soc.* **2012**, *41*, 2036-2051.

37.   Kumar, B.; Llorente, M.; Froehlich, J.; Dang, T.; Sathrum, A.; Kubiak, C. P. Photochemical and photoelectrochemical reduction of CO_2. *Annu. Rev. Phys. Chem.* **2012**, *63*, 541-569.

38.   Kang, P.; Chen, Z. F.; Brookhart, M.; Meyer, T. J. Electrocatalytic reduction of carbon dioxide: Let the molecules do the work. *Top. Catal.* **2015**, *58*, 30-45.

39.   Bockris, J. O. M.; Wass, J. C. The photoelectrocatalytic reduction of carbon dioxide. *J. Electrochem. Soc.* **1989**, *136*, 2521-2528.

40.   Appel, A. M.; Bercaw, J. E.; Bocarsly, A. B.; Dobbek, H.; DuBois, D. L.; Dupuis, M.; Ferry, J. G.; Fujita, E.; Hille, R.; Kenis, P. J. A.; Kerfeld, C. A.; Morris, R. H.; Peden, C. H. F.; Portis, A. R.; Ragsdale, S. W.; Rauchfuss, T. B.; Reek, J. N. H.; Seefeldt, L. C.; Thauer, R. K.; Waldrop, G. L. Frontiers, opportunities, and challenges in biochemical and chemical catalysis of CO_2 fixation. *Chemical Reviews* **2013**, *113*, 6621-6658.

41.   Weber, J. M. A pulsed ion source for the preparation of metal containing cluster ions using supersonic entrainment of laser vaporized metal. *Rev. Sci. Instrum.* **2005**, *76*, 043301.

42.   Robertson, W. H.; Kelley, J. A.; Johnson, M. A. A pulsed supersonic entrainment reactor for the rational preparation of cold ionic complexes. *Rev. Sci. Instrum.* **2000**, *71*, 4431-4434.

43.   Stoermer, C. W.; Gilb, S.; Friedrich, J.; Schooss, D.; Kappes, M. M. A high resolution dual mass gate for ion separation in laser desorption/ionization time of flight mass spectrometry. *Rev. Sci. Instrum.* **1998**, *69*, 1661-1664.

44.   Fenn, J. B.; Mann, M.; Meng, C. K.; Wong, S. F.; Whitehouse, C. M. Electrospray ionization for mass spectrometry of large biomolecules. *Science* **1989**, *246*, 64-71.

45.   Lu, I.-C.; Lee, C.; Lee, Y.-T.; Ni, C.-K. Ionization mechanism of matrix-assisted laser desorption/ionization. *Annu. Rev. Anal. Chem.* **2015**, *8*, 21-39.

46.   Johnson, M. A.; Lineberger, W. C. In *Techniques for the Study of Ion Molecule Reactions*; Farrar, J. M., Saunders, W., Eds.; Wiley: New York, 1988, p 591.

47.   Campargue, R. Aerodynamic separation effect on gas and isotope mixtures induced by invasion of the free jet shock wave structure. *J. Chem. Phys.* **1970**, *52*, 1795-1802.

48.   Klots, C. E. Evaporative cooling. *J. Chem. Phys.* **1985**, *83*, 5854-5860.

49.   Dietz, T. G.; Duncan, M. A.; Powers, D. E.; Smalley, R. E. Laser production of supersonic metal cluster beams. *J. Chem. Phys.* **1981**, *74*, 6511-6512.

50.   Bondybey, V. E.; English, J. H. Laser induced fluorescence of metal clusters produced by laser vaporization: Gas phase spectrum of Pb_2. *J. Chem. Phys.* **1981**, *74*, 6978-6979.

51.   Weber, J. M.; Robertson, W. H.; Johnson, M. A. Argon predissociation and electron autodetachment spectroscopy of size-selected $CH_3NO_2^-\cdot Ar_n$ clusters. *J. Chem. Phys.* **2001**, *115*, 10718-10723.

52.   Wiley, W. C.; McLaren, I. H. Time-of-flight mass spectrometer with improved resolution. *Rev. Sci. Instrum.* **1955**, *26*, 1150-1157.

53.   Misaizu, F.; Mitsuke, K.; Kondow, T.; Kuchitsu, K. Formation of negative cluster ions from $(CO_2)_m$ in collision with high-Rydberg atoms. *J. Chem. Phys.* **1991**, *94*, 243-249.

54.   Alexander, M. L.; Johnson, M. A.; Levinger, N. E.; Lineberger, W. C. Photodissociation of mass-selected $(CO_2)_n^-$ clusters: evaporation leading to magic numbers in fragment-ion distributions. *Phys. Rev, Lett.* **1986**, *57*, 976-979.

55.   Ahlrichs, R.; Bär, M.; Häser, M.; Horn, H.; Kölmel, C. Electronic-Structure Calculations on Workstation Computers - the Program System Turbomole. *Chem. Phys. Lett.* **1989**, *162*, 165-169.

56.   Becke, A. D. Density-functional exchange-energy approximation with correct asymptotic-behavior. *Phys. Rev. A* **1988**, *38*, 3098-3100.

57.   Grimme, S. Accurate description of van der Waals complexes by density functional theory including empirical corrections. *J. Comput. Chem.* **2004**, *25*, 1463-1473.

58.   Weigend, F.; Ahlrichs, R. Balanced basis sets of split valence, triple zeta valence and quadruple zeta valence quality for H to Rn: Design and assessment of accuracy. *Phys. Chem. Chem. Phys.* **2005**, *7*, 3297-3305.

59.   Deglmann, P.; Furche, F.; Ahlrichs, R. An efficient implementation of second analytical derivatives for density functional methods. *Chem. Phys. Lett.* **2002**, *362*, 511-518.

60.   Reed, A. E.; Weinstock, R. B.; Weinhold, F. Natural population analysis. *J. Chem. Phys.* **1985**, *83*, 735-746.

61.   Hori, Y.; Wakebe, H.; Tsukamoto, T.; Koga, O. Electrocatalytic process of CO selectivity in electrochemical reduction of CO_2 at metal electrodes in aqueous media. *Electrochim. Acta* **1994**, *39*, 1833-1839.

62.   Hori, Y.; Koga, O.; Yamazaki, H.; Matsuo, T. Infrared spectroscopy of adsorbed CO and intermediate species in electrochemical reduction of CO_2 to hydrocarbons on a Cu electrode. *Electrochim. Acta* **1995**, *40*, 2617-2622.

63.   Yoshio, H.; Katsuhei, K.; Shin, S. Production of CO and CH_4 in electrochemical reduction of CO_2 at metal electrodes in aqueous hydrogencarbonate solution. *Chem. Lett.* **1985**, *14*, 1695-1698.

64.   DiMeglio, J. L.; Rosenthal, J. Selective conversion of CO_2 to CO with high efficiency using an inexpensive bismuth-based electrocatalyst. *J. Am. Chem. Soc.* **2013**, *135*, 8798-8801.

65.   Medina-Ramos, J.; DiMeglio, J. L.; Rosenthal, J. Efficient reduction of CO_2 to CO with high current density using in situ or ex situ prepared Bi-based materials. *J. Am. Chem. Soc.* **2014**, *136*, 8361-8367.

66.   Sampson, M. D.; Nguyen, A. D.; Grice, K. A.; Moore, C. E.; Rheingold, A. L.; Kubiak, C. P. Manganese catalysts with bulky bipyridine ligands for the electrocatalytic reduction of carbon dioxide: eliminating dimerization and altering catalysis. *J. Am. Chem. Soc.* **2014**, *136*, 5460-5471.

67.   Song, J.; Klein, E. L.; Neese, F.; Ye, S. The mechanism of homogeneous CO_2 reduction by Ni(cyclam): Product selectivity, concerted proton–electron transfer and C–O bond cleavage. *Inorganic Chemistry* **2014**, *53*, 7500-7507.

68.   Chandrasekaran, K.; Bockris, L. O. M. In-situ spectroscopic investigation of adsorbed intermediate radicals in electrochemical reactions: CO_2^- on platinum. *Surface Science* **1987**, *185*, 495-514.

69.   Thompson, M. C.; Ramsay, J.; Weber, J. M. Interaction of CO_2 with atomic manganese in the presence of an excess negative charge probed by infrared spectroscopy of $[Mn(CO_2)_n]^-$ clusters. *J. Phys. Chem. A* **2017**, *121*, 7534–7542.

70.   Thompson, M. C.; Dodson, L. G.; Weber, J. M. Structural motifs of $[Fe(CO_2)_n]^-$ clusters ($n = 3$–7). *J. Phys. Chem. A* **2017**, *121*, 4132-4138.

71.   Pichugin, K.; Grumbling, E.; Velarde, L.; Sanov, A. Solvation-induced cluster anion core switching from $NNO_2^-(N_2O)_{n-1}$ to $O^-(N_2O)_n$. *J. Chem. Phys.* **2008**, *129*.

72.   Boese, A. D.; Schneider, H.; Gloess, A. N.; Weber, J. M. The infrared spectrum of $Au^-\cdot CO_2$. *J. Chem. Phys.* **2005**, *122*, 154301.

73.   Hartman, K. O.; Hisatsune, I. C. Infrared spectrum of carbon dioxide anion radical. *J. Chem. Phys.* **1966**, *44*, 1913-1918.

74.   Del Castillo, A.; Alvarez-Guerra, M.; Irabien, A. Continuous electroreduction of CO_2 to formate using Sn gas diffusion electrodes. *AIChE J.* **2014**, *60*, 3557-3564.

75.   Baruch, M. F.; Pander, J. E.; White, J. L.; Bocarsly, A. B. Mechanistic insights into the reduction of CO_2 on tin electrodes using in situ ATR-IR spectroscopy. *ACS Catal.* **2015**, *5*, 3148-3156.

76.   Chen, Y.; Kanan, M. W. Tin oxide dependence of the CO_2 reduction efficiency on tin electrodes and enhanced activity for tin/tin oxide thin-film catalysts. *J. Am. Chem. Soc.* **2012**, *134*, 1986-1989.

77.   Medina-Ramos, J.; Pupillo, R. C.; Keane, T. P.; DiMeglio, J. L.; Rosenthal, J. Efficient conversion of CO_2 to CO using tin and other inexpensive and easily prepared post-transition metal catalysts. *J. Am. Chem. Soc.* **2015**, *137*, 5021-5027.

78.   Li, C. W.; Ciston, J.; Kanan, M. W. Electroreduction of carbon monoxide to liquid fuel on oxide-derived nanocrystalline copper. *Nature* **2014**, *508*, 504-507.

79.   Knurr, B. J.; Weber, J. M. Infrared spectra and structures of anionic complexes of cobalt with carbon dioxide ligands. *J. Phys. Chem. A* **2014**, *118*, 4056-4062.

80.   Knurr, B. J.; Weber, J. M. Interaction of nickel with carbon dioxide in $[Ni(CO_2)_n]^-$ clusters studied by infrared spectroscopy. *J. Phys. Chem. A* **2014**, *118*, 8753-8757.

81.   Thompson, M. C.; Ramsay, J.; Weber, J. M. Solvent-driven reductive activation of CO_2 by bismuth: Switching from metalloformate complexes to oxalate products. *Angew. Chem. Int. Ed.* **2016**, *55*, 15171-15174.

82.   Dodson, L. G.; Thompson, M. C.; Weber, J. M. Titanium insertion into CO bonds in anionic Ti–CO_2 complexes. *J. Phys. Chem. A* **2018**.

83.   Miller, T. M.; Miller, A. E. S.; Lineberger, W. C. Electron affinities of Ge and Sn. *Phys. Rev. A* **1986**, *33*, 3558-3559.

84.   Ho, J.; Polak, M. L.; Lineberger, W. C. Photoelectron spectroscopy of group IV heavy metal dimers: Sn_2^-, Pb_2^-, and $SnPb^-$. *J. Chem. Phys.* **1992**, *96*, 144-154.

85.   Moravec, V. D.; Klopcic, S. A.; Jarrold, C. C. Anion photoelectron spectroscopy of small tin clusters. *J. Chem. Phys.* **1999**, *110*, 5079-5088.

86.   Schneider, H.; Boese, A. D.; Weber, J. M. Unusual hydrogen bonding behavior in binary complexes of coinage metal anions with water. *J. Chem. Phys.* **2005**, *123*, 084307.

87.   Zhang, X.; Lim, E.; Kim, S. K.; Bowen, K. H. Photoelectron spectroscopic and computational study of (M–CO_2)$^-$ anions, M = Cu, Ag, Au. *J. Chem. Phys.* **2015**, *143*, 174305.

88.   Miller, G. B. S.; Esser, T. K.; Knorke, H.; Gewinner, S.; Schoellkopf, W.; Heine, N.; Asmis, K. R.; Uggerud, E. Spectroscopic identification of a bidentate binding motif in the anionic magnesium-CO_2 complex (ClMgCO$_2$)$^-$. *Angew. Chem.-Int. Edit.* **2014**, *53*, 14407-14410.

89.   Schwarz, H. Metal-mediated activation of carbon dioxide in the gas phase: Mechanistic insight derived from a combined experimental/computational approach. *Coord. Chem. Rev.* **2017**, *334*, 112-123.

90.   Gibson, D. H. The organometallic chemistry of carbon dioxide. *Chemical Reviews* **1996**, *96*, 2063-2095.

91.   Yang, H. Q.; Xu, Z. H.; Fan, M. H.; Gupta, R.; Slimane, R. B.; Bland, A. E.; Wright, I. Progress in carbon dioxide separation and capture: A review. *J. Environ. Sci.* **2008**, *20*, 14-27.

92.   Qiao, J.; Liu, Y.; Hong, F.; Zhang, J. A review of catalysts for the electroreduction of carbon dioxide to produce low-carbon fuels. *Chem. Rev. Soc.* **2014**, *43*, 631-675.

93.   Scurlock, C. T.; Pullins, S. H.; Duncan, M. A. Photodissociation spectroscopy of Ca^+-CO_2. *J. Chem. Phys.* **1996**, *105*, 3579-3585.

94.   Gregoire, G.; Velasquez, J.; Duncan, M. A. Infrared photodissociation spectroscopy of small $Fe^+(CO_2)_n$ and $Fe^+(CO_2)_n$ Ar clusters. *Chem. Phys. Lett.* **2001**, *349*, 451-457.

95.	Walker, N. R.; Grieves, G. A.; Walters, R. S.; Duncan, M. A. The metal coordination in $Ni^+(CO2)_n$ and $NiO_2^+(CO_2)_m$ complexes. *Chem. Phys. Lett.* **2003**, *380*, 230-236.

96.	Gregoire, G.; Brinkmann, N. R.; van Heijnsbergen, D.; Schaefer, H. F.; Duncan, M. A. Infrared photodissociation spectroscopy of $Mg^+(CO_2)_n$ and $Mg^+(CO_2)_nAr$ clusters. *J. Phys. Chem. A* **2003**, *107*, 218-227.

97.	Walters, R. S.; Brinkmann, N. R.; Schaefer, H. F.; Duncan, M. A. Infrared photodissociation spectroscopy of mass-selected $Al^+(CO_2)_n$ and $Al^+(CO_2)_nAr$ clusters. *J. Phys. Chem. A* **2003**, *107*, 7396-7405.

98.	Walker, N. R.; Walters, R. S.; Duncan, M. A. Infrared photodissociation spectroscopy of $V^+(CO_2)_n$ and $V^+(CO_2)_n$ Ar complexes. *J. Chem. Phys.* **2004**, *120*, 10037-10045.

99.	Ricks, A. M.; Brathwaite, A. D.; Duncan, M. A. IR spectroscopy of gas phase $V(CO_2)_n^+$ clusters: Solvation-induced electron transfer and activation of CO_2. *J. Phys. Chem. A* **2013**, *117*, 11490-11498.

100.	Iskra, A.; Gentleman, A. S.; Kartouzian, A.; Kent, M. J.; Sharp, A. P.; Mackenzie, S. R. Infrared spectroscopy of gas-phase $M^+(CO_2)_n$ (M = Co, Rh, Ir) ion–molecule complexes. *J. Phys. Chem. A* **2017**, *121*, 133-140.

101.	Fatur, S. M.; Shepard, S. G.; Higgins, R. F.; Shores, M. P.; Damrauer, N. H. A synthetically tunable system to control MLCT excited-state lifetimes and spin states in iron(II) polypyridines. *J. Am. Chem. Soc.* **2017**, *139*, 4493-4505.

102.	Engelking, P. C.; Lineberger, W. C. Laser photoelectron spectrometry of Fe^-: The electron affinity of iron and the "nonstatistical" fine-structure detachment intensities at 488 nm. *Phys. Rev. A* **1979**, *19*, 149-155.

103.	Darwent, B. d. Bond dissociation energies in simple molecules. *Nat. Stand. Ref. Data Ser.* **1970**.

104.	Bratsch, S. G.; Lagowski, J. J. Predicted stabilities of monatomic anions in water and liquid ammonia at 298.15 K. *Polyhedron* **1986**, *5*, 1763-1770.

105.	Walker, N. R.; Walters, R. S.; Grieves, G. A.; Duncan, M. A. Growth dynamics and intracluster reactions in $Ni^+(CO_2)_n$ complexes via infrared spectroscopy. *J. Chem. Phys.* **2004**, *121*, 10498-10507.

106.	Myshakin, E. M.; Jordan, K. D.; Sibert, E. L.; Johnson, M. A. Large anharmonic effects in the infrared spectra of the symmetrical $CH_3NO_2^-\cdot(H_2O)$ and $CH_3CO_2^-\cdot(H_2O)$ complexes. *J. Chem. Phys.* **2003**, *119*, 10138-10145.

107.	Armentrout, P. B.; Koizumi, H.; MacKenna, M. Sequential bond energies of $Fe^+(CO_2)_n$, n = 1−5, determined by threshold collision-induced dissociation and ab initio theory. *J. Phys. Chem. A* **2005**, *109*, 11365-11375.

108.	Whitney, E. S.; Dong, F.; Nesbitt, D. J. Jet-cooled infrared spectroscopy in slit supersonic discharges: Symmetric and antisymmetric CH_2 stretching modes of fluoromethyl (CH_2F) radical. *J. Chem. Phys.* **2006**, *125*, 054304.

109.	Whitney, E. S.; Haeber, T.; Schuder, M. D.; Blair, A. C.; Nesbitt, D. J. High-resolution infrared studies in slit supersonic discharges: CH_2 stretch excitation of jet-cooled CH_2Cl radical. *J. Chem. Phys.* **2006**, *125*, 054303.

110.	Carnegie, P. D.; McCoy, A. B.; Duncan, M. A. IR spectroscopy and theory of $Cu^+(H_2O)Ar_2$ and $Cu^+(D_2O)Ar_2$ in the O−H (O−D) stretching region: Fundamentals and combination bands. *J. Phys. Chem. A* **2009**, *113*, 4849-4854.

111.	McCoy, A. B.; Guasco, T. L.; Leavitt, C. M.; Olesen, S. G.; Johnson, M. A. Vibrational manifestations of strong non-Condon effects in the $H_3O^+\bullet X_3$ (X = Ar, N_2, CH_4, H_2O) complexes: A possible explanation for the intensity in the "association band" in the vibrational spectrum of water. *Phys. Chem. Chem. Phys.* **2012**, *14*, 7205-7214.

112.	Roscioli, J. R.; Diken, E. G.; Johnson, M. A.; Horvath, S.; McCoy, A. B. Prying apart a water molecule with anionic H-bonding: A comparative spectroscopic study of the $X^-\cdot H_2O$ (X = OH, O, F, Cl, and Br) binary complexes in the 600-3800 cm^{-1} region. *J. Phys. Chem. A* **2006**, *110*, 4943-4952.

113.	Armbruster, M. K.; Weigend, F.; van Wullen, C.; Klopper, W. Self-consistent treatment of spin-orbit interactions with efficient Hartree-Fock and density functional methods. *Phys. Chem. Chem. Phys.* **2008**, *10*, 1748-1756.

114.	Ehrhardt, C.; Ahlrichs, R. Population analysis based on occupation numbers .2. Relationship between shared electron numbers and bond-energies and characterization of hypervalent contributions. *Theor. Chem. Acc* **1985**, *68*, 231-245.

115.	Gerardi, H. K.; DeBlase, A. F.; Su, X.; Jordan, K. D.; McCoy, A. B.; Johnson, M. A. Unraveling the anomalous solvatochromic response of the formate ion vibrational spectrum: An infrared, Ar-tagging study of the HCO_2^-, DCO_2^-, and $HCO_2^-\cdot H_2O$ ions. *Phys. Chem. Lett.* **2011**, *2*, 2437-2441.

116.	Garrett, B. C.; Dixon, D. A.; Camaioni, D. M.; Chipman, D. M.; Johnson, M. A.; Jonah, C. D.; Kimmel, G. A.; Miller, J. H.; Rescigno, T. N.; Rossky, P. J.; Xantheas, S. S.; Colson, S. D.; Laufer, A. H.; Ray, D.; Barbara, P. F.; Bartels, D. M.; Becker, K. H.; Bowen, H.; Bradforth, S. E.; Carmichael, I.; Coe, J. V.; Corrales, L. R.; Cowin, J. P.; Dupuis, M.; Eisenthal, K. B.; Franz, J. A.; Gutowski, M. S.; Jordan, K. D.; Kay, B. D.; LaVerne, J. A.; Lymar, S. V.; Madey, T. E.; McCurdy, C. W.; Meisel, D.; Mukamel, S.; Nilsson, A. R.; Orlando, T. M.; Petrik, N. G.; Pimblott, S. M.; Rustad, J. R.; Schenter, G. K.; Singer, S. J.; Tokmakoff, A.; Wang, L. S.; Wittig, C.; Zwier, T. S.

Role of water in electron-initiated processes and radical chemistry: Issues and scientific advances. *Chemical Reviews* **2005**, *105*, 355-389.

117.   Paulson, J. F. Negative-ion-neutral reactions in N_2O. *J. Chem. Phys.* **1970**, *52*, 959-962.

118.   Ferguson, E. E.; Fehsenfeld, F. C.; Schmeltekopf, A. L. Geometrical considerations for negative ion processes. *J. Chem. Phys.* **1967**, *47*, 3085-3086.

119.   Marx, R.; Mauclair, G.; Fehsenfeld, F. C.; Dunkin, D. B.; Ferguson, E. E. Negative-ion reactions in N_2O at low energies. *J. Chem. Phys.* **1973**, *58*, 3267-3273.

120.   Chantry, P. J. Temperature dependence of dissociative attachment in N_2O. *J. Chem. Phys.* **1969**, *51*, 3369-3379.

121.   Chantry, P. J. Formation of N_2O- via ion-molecule reactions in N_2O. *J. Chem. Phys.* **1969**, *51*, 3380-3384.

122.   Hopper, D. G.; Wahl, A. C.; Wu, R. L. C.; Tiernan, T. O. Theoretical and experimental studies of N_2O^- and N_2O ground-state potential-energy surfaces - implications for O^-+N_2 - N_2O+e and other processes. *J. Chem. Phys.* **1976**, *65*, 5474-5494.

123.   Nalley, S. J.; Compton, R. N.; Schweinler, H. C.; Anderson, V. E. Molecular electron affinities from collisional ionization of cesium .1. NO, NO_2, AND N_2O. *J. Chem. Phys.* **1973**, *59*, 4125-4139.

124.   Kryachko, E. S.; Vinckier, C.; Nguyen, M. T. Another look at the electron attachment to nitrous oxide. *J. Chem. Phys.* **2001**, *114*, 7911-7917.

125.   Suter, H. U.; Greber, T. On the dissociation of N_2O after electron attaclnnent. *J. Phys. Chem. B* **2004**, *108*, 14511-14517.

126.   Weigend, F.; Häser, M. RI-MP2: first derivatives and global consistency. *Theor. Chem. Acc.* **1997**, *97*, 331-340.

127.   Weigend, F.; Häser, M.; Patzelt, H.; Ahlrichs, R. RI-MP2: optimized auxiliary basis sets and demonstration of efficiency. *Chem. Phys. Lett.* **1998**, *294*, 143-152.

128.   Schulz, G. J. Study of N_2O molecule using electron beams. *J. Chem. Phys.* **1961**, *34*, 1778-&.

129.   Kaufman, F. N_2O bond dissociation energy. *J. Chem. Phys.* **1967**, *46*, 2449-&.

130.   Bruning, F.; Matejcik, S.; Illenberger, E.; Chu, Y. N.; Senn, G.; Muigg, D.; Denifl, G.; Märk, T. D. Effects of temperature on the dissociative electron attachment to N_2O. *Chem. Phys. Lett.* **1998**, *292*, 177-182.

131. Takahashi, K. J.; Ohgami, S.; Koyama, Y.; Sawamura, S.; Marin, T. W.; Bartels, D. M.; Jonah, C. D. Reaction rates of the hydrated electron with N_2O in high temperature water and potential surface of the N_2O^- anion. *Chem. Phys. Lett.* **2004**, *383*, 445-450.

132. Weber, J. M.; Leber, E.; Ruf, M. W.; Hotop, H. Nuclear-excited Feshbach resonances in electron attachment to molecular clusters. *Phys. Rev. Lett.* **1999**, *82*, 516-519.

133. Leber, E.; Barsotti, S.; Bömmels, J.; Weber, J. M.; Fabrikant, I. I.; Ruf, M. W.; Hotop, H. Vibrational Feshbach resonances in electron attachment to nitrous oxide clusters: decay into heterogeneous and homogeneous cluster anions. *Chem. Phys. Lett.* **2000**, *325*, 345-353.

134. Hotop, H.; Ruf, M. W.; Fabrikant, I. I. Resonance and threshold phenomena in low-energy electron collisions with molecules and clusters. *Phys. Scr.* **2004**, *T110*, 22-31.

135. Kraft, T.; Ruf, M. W.; Hotop, H. Electron-transfer from state-selected rydberg atoms to $(N_2O)_m$ AND $(CF_3Cl)_m$ clusters. *Z. Phys. D - At. Mol. Clust.* **1991**, *20*, 13-15.

136. Kraft, T.; Ruf, M. W.; Hotop, H. Strong dependence of negative cluster ion spectra on principal quantum number n in collisions of state-selected $Ar^{**}(nd)$ rydberg atoms with N_2O clusters. *Z. Phys. D - At. Mol. Clust.* **1990**, *17*, 37-43.

137. Hanel, G.; Fiegele, T.; Stamatovic, A.; Märk, T. D. Dissociative electron attachment to N_2O clusters: attachment spectra for $(N_2O)_nO^-$ anions (n=0-7) from about 0 up to 25 eV. *Int. J. Mass Spectrom.* **2001**, *205*, 65-75.

138. Vizcaino, V.; Denifl, S.; Märk, T. D.; Illenberger, E.; Scheier, P. Low energy (0-4 eV) electron impact to N_2O clusters: Dissociative electron attachment, ion-molecule reactions, and vibrational Feshbach resonances. *J. Chem. Phys.* **2010**, *133*.

139. Posey, L. A.; Johnson, M. A. Pulsed photoelectron-spectroscopy of negative cluster ions - Isolation of 3 distinguishable forms of N_2O_2. *J. Chem. Phys.* **1988**, *88*, 5383-5395.

140. Velarde, L.; Habteyes, T.; Grumbling, E. R.; Pichugin, K.; Sanov, A. Solvent resonance effect on the anisotropy of $NO^-(N_2O)_n$ cluster anion photodetachment. *J. Chem. Phys.* **2007**, *127*.

141. Grumbling, E. R.; Pichugin, K.; Velarde, L.; Sanov, A. Further evidence for resonant photoelectron-solvent scattering in nitrous oxide cluster anions. *J. Phys. Chem. A* **2010**, *114*, 1367-1373.

142. Yarkony, D. R. On the reaction $Mg+N_2O- MgO+N_2$. *J. Chem. Phys.* **1983**, *78*, 6763-6772.

143. Huang, D.-H.; Wang, F.-H.; Zhu, Z.-H. Study of potential energy function for ground state N_2O. *Acta Chim. Sinica* **2007**, *65*, 994-997.

144.   Sanford, T.; Andrews, D.; Rathbone, J.; Taylor, M.; Muntean, F.; Thompson, M.; McCoy, A. B.; Parson, R.; Lineberger, W. C. Time resolved solvent rearrangement dynamics. *Faraday Disc.* **2004**, *127*, 383-394.